Fabrication of Ferromagnetic Nanostructures via Analysis and Control of Electrochemical Nucleation Process

電析初期過程の解析および微細構造制御による強磁性ナノ構造体の形成

February, 2017

Siggi WODARZ

ヴォダルツ　ジギー

Fabrication of Ferromagnetic Nanostructures via Analysis and Control of Electrochemical Nucleation Process

電析初期過程の解析および微細構造制御による強磁性ナノ構造体の形成

February 2017

Waseda University

Graduate School of Advanced Science and Engineering

Department of Applied Chemistry, Research on Interface Electrochemistry

Siggi WODARZ

ヴォダルツ　ジギー

Contents

Chapter 1

General Introduction

1.1 Introduction

Along with the explosive progress in the modern information industry, world's total data is expected to exceed 40 zettabytes in 2020 [1]. Due to this exponential increase in data volumes, hard disk drive (HDD), which plays a major role in the magnetic recording media, currently required an areal recording density of more than 1.0 Tbit/in^2; the Advanced Storage Technology Consortium (ASTC) released the technology roadmap for the research and development of HDD towards ultra-high density magnetic recording (Fig. 1.1.1) [2]. Conventional HDD employs continuous granular film media, in which the magnetic particles are separated by the non-magnetic grain boundaries [3,4]. In this film media data is stored in ensembles of several magnetic grains, thus to achieve higher areal density the grain size has to be reduced in several nanometer size. Because the smaller volume of magnetic particle would result in loss of thermal stability due to the superparamagnetic characteristics of the particle, use of ferromagnetic materials with high uniaxial magnetocrystalline anisotropy, K_u, is required. However, high K_u materials require high switching magnetic field, which makes difficult to write a data. To overcome these trilemma among high areal density, thermal stability, and writeability, several technologies were proposed as promising candidates for the ultra-high density magnetic recording media as described in Fig. 1.1.2 [5].

Bit patterned magnetic recording (BPMR) [6] is expected to achieve areal densities more than 1.0 Tbit/in^2 by physically separating the magnetic grains to form isloated nanodot arrays, which is explained in detail in next section. Shingled write recording (SWR) combining two demensional mangetic recording (TDMR) [7] utilizes wide write-pole to write a series of overlapping tracks, enabling to achieve high track density. In energy assisted magnetic recording, such as heat assisted magnetic recording (HAMR) [8, 9] and microwave-assisted magnetic recording (MAMR) [10, 11], high areal density can be achied by temporary reducing the coercivity with heating or microwave filed at nanometer sized region, allowing the use of high K_u materials to maintain high thermal stability at ultra-high areal densities. In future technologies, employment of HAMR in BPM would allow further increase in areal density, which is expected to exceeds 10 Tbit/in^2 as described in Fig. 1.1.1.

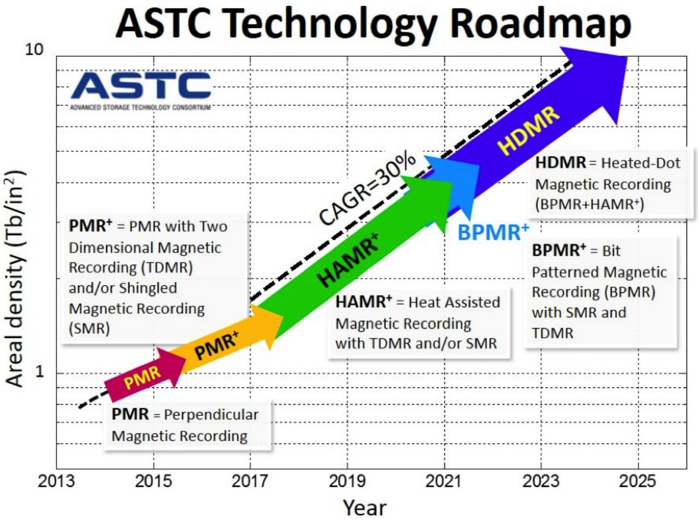

Fig. 1.1.1 Technology roadmap of magnetic recording in hard disl drive [2]

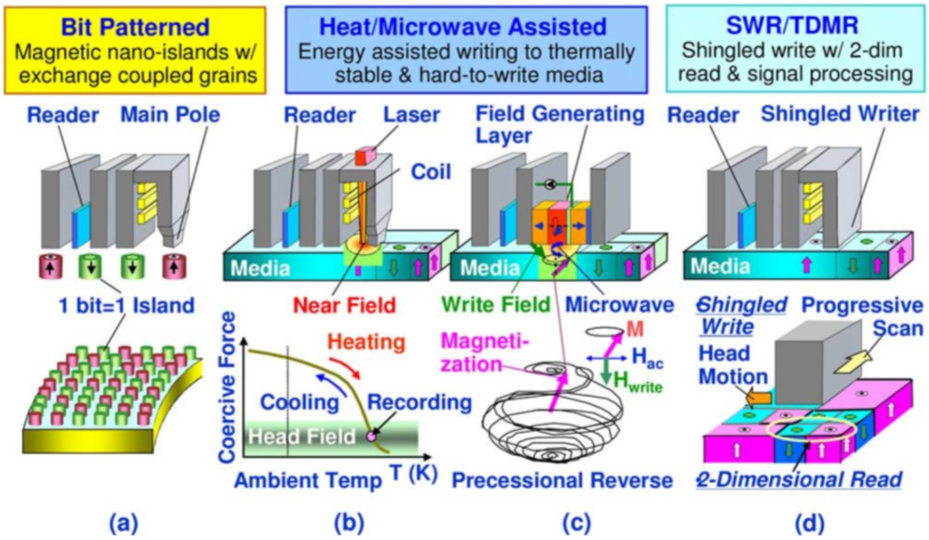

Fig. 1.1.2 Future technology options for HDD storage. (a) Bit patterned magneticc recording (BPMR), (b) heat-assisted mangetic recording (HAMR), (c) microwave-asisted magnetic recording (HAMR), and (d) shingled write recording with two dimensional magnetic recording (SMR/TDMR) [5]

1.2 Ferromagnetic Materials with High K_u

In order to achieve Tbit-level recording density in BPM, energy barrier of ferromagnetic nanodots is required as following Eq. (1.3.1) to stabilize stored data without an effect of superparamagnetic limit; where K_u is uniaxial magnetocrystalline anisotropy constant, V is volume of ferromagnetic, k_B is Boltzmann constant and T is temperature.

$$K_u V > 60\ k_B T \qquad (1.3.1)$$

Superparamagnetic limit is caused when magnetic anisotropy energy $K_u V$ is below the right hand side, where $k_B T$ is a thermal energy, thus in order to achieve both small volume and thermal stability high K_u materials are required in ultra-high density magnetic recording. Table 1.3.1 summarized the high K_u materials, which was referred to Ref. [9]. CoPt is one of the high K_u materials that their magnetic properties change with alloy composition, for example, hcp-CoPt, Co_3Pt [9, 12] which are consist of cobalt rich composition and $L1_0$ ordered structure CoPt [9, 13] at equiatomic composition. Although, this ordered alloy has been studied to apply in magnetic recording media due to its high magnetic anisotropy, post annealing at high temperature is required for the phase transformation. Hcp-CoPt shows relatively high magnetic anisotropy without any annealing treatment at the as-deposited state, which simplifies the fabrication process of magnetic recording media. On the other hand, among high K_u materials, $L1_0$-FePt [13, 14] is expected as a leading candidate since it shows 10 times higher K_u than CoPtCr alloys [9, 15], as used in conventional HDD. The ordered $Fe_{14}Nd_2B$ [16, 17] and $SmCo_5$ [18, 19] also exhibit high K_u values, although these materials are considered to be difficult for the BPM application due to the corrosion issue.The minimal stable grain size, D_p, in table 1.3.1 was calculated from Eq. (1.3.1), assuming that the magnetic grain is 10 nm-thick columnar shape. The calculated values showed that the FePt can be minimized to the diameter of 2.3 nm, which enables to achieve thermal stability at areal density of more than 50 Tbit/in^2.

As described above, the use of high K_u materials in BPM system is significant to achieve high thermal stability at Tbit/in^2 areal density. In this thesis, hcp-CoPt alloy (chapter 2, 3) and $L1_0$-FePt (chapter 4, 5) alloy were applied for the fabrication process of nanodot arrays due to their excellent features described above.

Table 1.3.1 Magnetic properties of high K_u materials

Materials	K_u / 10^7erg cm^{-3}	M_s / emu cm^{-3}	H_k / kOe	D_p / nm
$CoCr_8Pt_{22}$	0.7	500	28.0	7.3
Co_3Pt	2.0	1100	36.4	4.3
CoPt	4.9	800	122.5	2.7
FePt	7.0	1140	122.8	2.3
$Fe_{14}NdB$	4.6	1270	72.4	2.8
$SmCo_5$	20	910	439.6	1.4

1.3 Bit Patterned Recording Media

Bit patterned recording media (BPMR) [6, 20-23] consists of physically isolated arrays of ordered ferromagnetic nanodot with diameter of about 10 nm, and each dot is magnetized to store a data, that is, one dot functions as one bit. For the conventional granular film media, because bit is recorded in assembled magnetic grains, high signal to noise ratio (SNR) caused by the demagnetization between each magnetic grain and thermal instability are considered as significant issues for achieving high areal density. Figure 1.4.1 shows the comparison between continuous granular film media and bit patterned media (BPM) [23]; 1 and 0 are attributed to the magnetization directions in up and down directions. In BPM, unfavorable magnetic coupling of each dot is eliminated due to the structural feature of physically isolated nanodots, thus low SNR can be achieved. In addition, since the grain size is allowed to be as large as the bit size in BPM, high value of K_u is not necessary to maintain high thermal stability, which avoids the insufficient writeability. Due to these features, areal density beyond 1.0 Tb/in^2 is expected to achieve in BPM.

For the practical use of BPM, several studies on the development of writing and reading of nanodot arrays were reported [24, 25]. In order to achieve high writeability in BPM, low switching field distribution for nanodots is significant. Grobis et al. demonstrated the recording performance of BPM by employing exchange coupled composited (ECC) structure to reduce the switching filed distribution [25]. ECC structure consisted of Co/Pd and Co/Ni multilayer structure, in which Co/Pd was hard layer and Co/Ni was soft layer. By optimizing the aspect ratio of magnetic island and write synchronization between the magnetic islands and the switching of the write head field, single track recording was successfully performed in 60 Gbit/in^2 BPM with commercially available recording head (Fig. 1.4.2) [25].

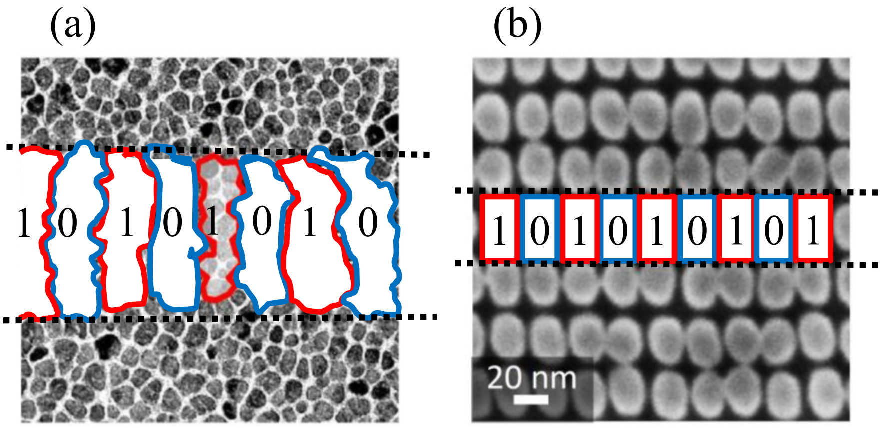

Fig. 1.3.1 Schematic illustrations of (a) conventional granular film media and (b) bit patterned media. The magnetizations in upper and downward directions are described as 1 and 0 in the images [23].

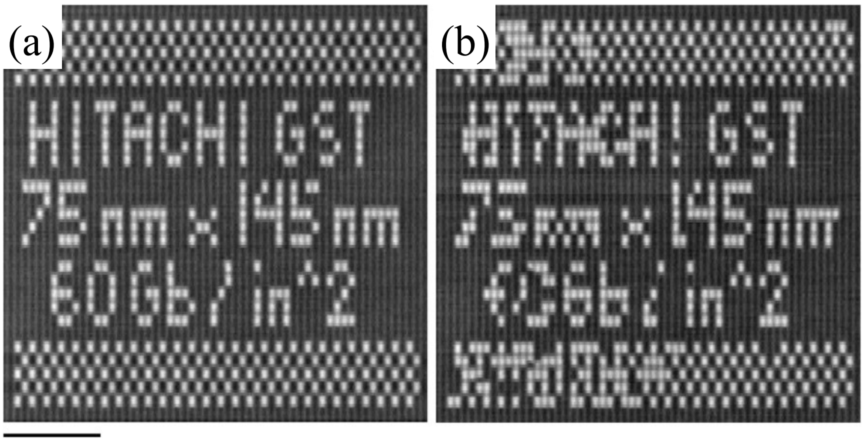

Fig. 1.3.2 Demonstration of recording performance of 60 Gbit/in^2 BPM with (a) good and (b) poor write synchronization. The scale bar is 1 μm [25].

1.4 Fabrication Process of Bit Patterned Media

Since the concept of BPM was proposed, several approaches on the fabrication of ordered ferromagnetic nanodo arrays for the use in BPM were proposed. In many case, the fabrication of nanodot arrays were performed by top-down approach, such as patterning the physically deposited ferromagnetic continuous films by lithography techniques. By contrast, electrochemical processes, so-called bottom-up approach, were also proposed as an alternative approach due to its excellent features of high areal selectivity and high deposition uniformity for fabricating micro/nano structure. In these methods, ferromagnetic materials are deposited inside the patterned substrate to fabricate nanodot arrays. Here, several examples for fabrication of nanodot arrays were introduced.

1.4.1 Physical Fabrication Process

Initially, the fabrication of BPM was attempted by depositing magnetic layer with perpendicular anisotropy onto pre-patterned pillar substrate [25-27]. In this method, Si substrate was etched by combining lithography technique and reactive ion etching (RIE). Because the deposition of magnetic layer is independent from the patterning process, magnetic properties is not affected by the etching process. Co/Pd and Co/Pt multilayer structure were suitable for this fabrication approach, since perpendicular anisotropy was originated from the interface of each layer these systems do not need to apply seed layer to induce magnetic anisotropy. Yang et al. reported fabrication process of Co/Pd multilayer magnetic nanodots with 3.3 Tbit/in^2 (15 nm in pitch) by fabricating pillar substrate via electron beam lithography (EBL) with hydrogen silsesquioxane (HSQ) resist as shown in Fig. 1.4.1 [27]. However, as the areal density increases, the side magnetic materials deposited at trench or wall of the pillar causes undesired magnetic decoupling, which is considered as critical issues for achieving Tbit/in^2 density. In addition, this system is suitable for the multilayer structure, but other materials with high perpendicular magnetic anisotropy, such as FePt and CoPtCr, were difficult to apply.

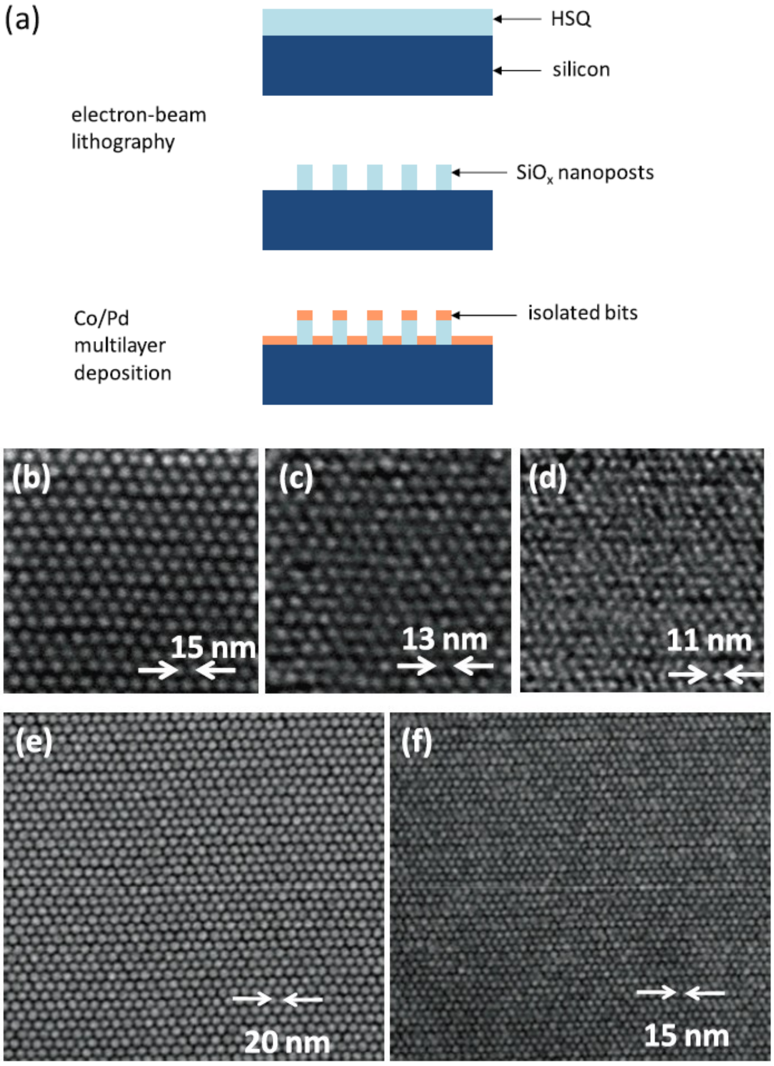

Fig. 1.4.1 Schematic of fabrication process of nanodot arrays. (b)-(d) SEM images of patterned HSQ resist fabricated by EBL. (e), (f) SEM images of Co/Pd nanodots with 1.9 Tbit/in^2 (e) and 3.3 Tbit/in^2 (f) [27]. Copyright 2011 by Nanotechnology. Reproduced with permission of Nanotechnology via Copyright Clearance Center.

Along with the development of patterning process or lithography technique, ferromagnetic nanodots were fabricated by patterning a continuous magnetic layer as alternative approach to depositing magnetic layer on pre-patterned substrate. In this method, magnetic layer with high perpendicular magnetic layer was etched by focused ion beam [28, 29] or RIE [30, 31]. Figure 1.4.2 illustrates the fabrication process of magnetic nano dot arrays fabricated by using electron beam lithography and RIE demonstrated by Albrecht et al [31].

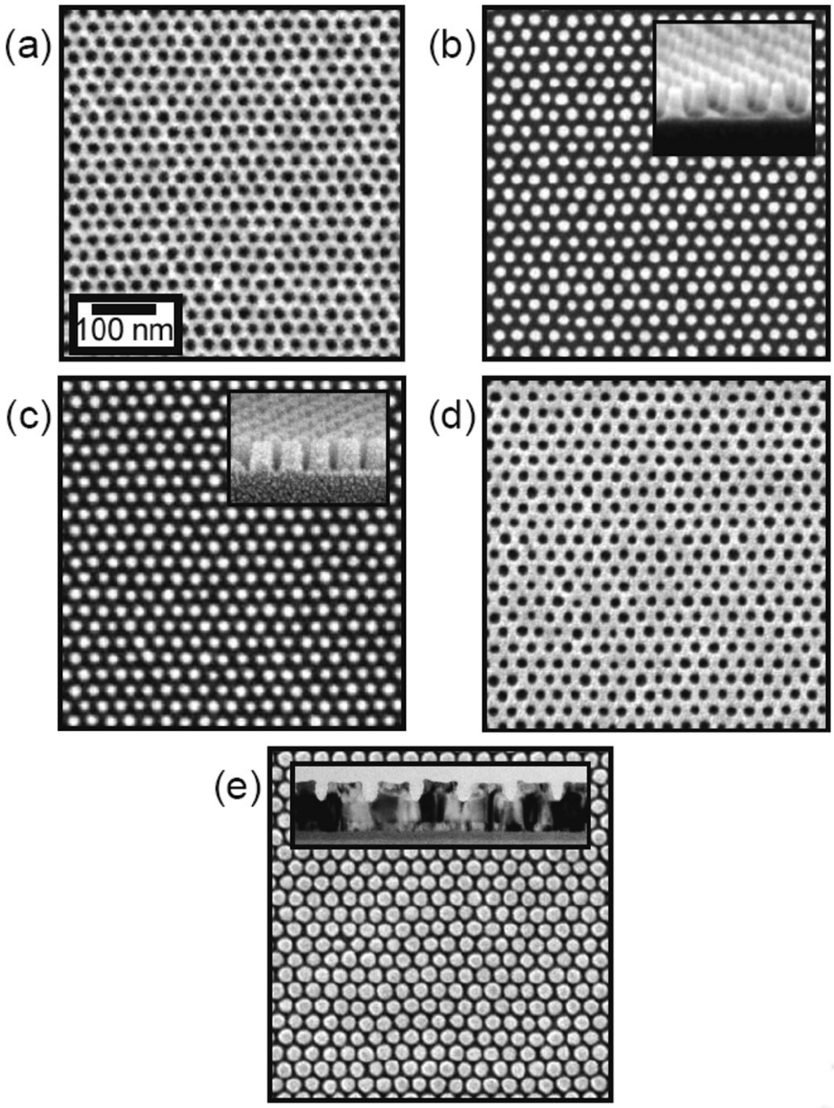

Fig. 1.4.2 SEM images of (a) developed block copolymer pattern on Si master template, (b) Si master template, (c) quartz replica working template, (d) imprinted resist on disk, and (e) finished magnetic nanodots (inset: cross-section TEM image) [31].

In order to further achieve higher areal density, fabrication process of nanopore patterned substrate was studied by the application of UV-cure nanoimprint lithography (UV-NIL) [32-34] and electron beam lithography (EBL) [34-37], which are powerful technique for the fabrication of nanopore patterned substrate with Tbit/in^2. In UV-NIL process, UV-transparent mold is pressed into UV-curable resist coated on the substrate and yields a negative copy of the mold by UV exposure. Since this process utilize mold, it has advantages of high resolution and high throughput. On the other hand, EBL is a maskless lithography technique, which electron beam directly draws desired patterns in several nanometers with high resolution. Although it shows low throughput, these features of EBL make it suitable for fundamental study of fabricating nanodot arrays with ultra-high recording density. In addition, nanopore patterns fabricated by EBL can be used to prepare the imprint template for application to UV-NIL. Based on the detail optimization of development process, Yang et al. demonstrated the high-resolution patterning of 2.0 Tbit/in^2 (18 nm in pitch) and 4.5 Tb/in^2 (12 nm in pitch) by using negative-type resist (Fig. 1.4.3) [36]. Utilizing the patterned substrate, fabrication of an imprint template has been also successfully demonstrated by the formation of Cr dot with 1.5 Tbit/in^2 (21 nm in pitch) [37]. In this thesis, nanopore patterned substrate was fabricated by EBL, and to achieve high areal density fabrication process of nanopore patterned substrate was investigated in detail in chapter 2.

Another approach to fabricate nanopore patterned substrate is the directed polymer self-assembly, which combines top-down advanced lithography with bottom-up self-assembling block copolymer (BCP) materials [38-40]. BCP materials can form periodic patterns with desirable shape in a self-assembled manner, which overcomes the low throughput of EBL process. For the patterning, low density patter is fabricated by EBL to guide the BCP into self-assembled domains. Yang et al. have successfully demonstrated the fabrication of nanopore patterns with 1.0 Tbit/in^2 on 6 inch fused silica template by using cylinder-forming poly (styrene-b-methyl methacrylate) (PS-b-PMMA) with chemical pre-pattern performed via EBL (Fig.1.4.4) [40]. Furthermore, they succeeded to fabricate imprint template for the UV-NIL process on 2.5 inch disk size media by using the patterned substrate, and succeeded to transfer into CoCrPt magnetic layer with 1.5 Tbit/in^2 by ion beam etching.

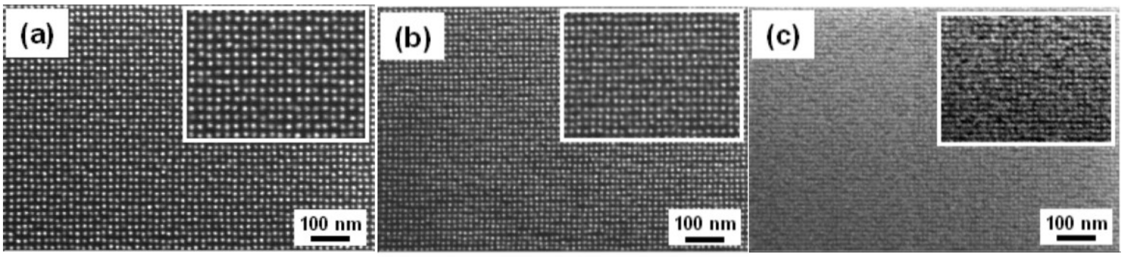

Fig. 1.4.3 SEM images of dot patterning with HSQ resist fabricated by EBL.
(a) 2.0 Tbit/in^2, (b) 2.9 Tbit/in^2, and (c) 4.5 Tbit/in^2 [36].

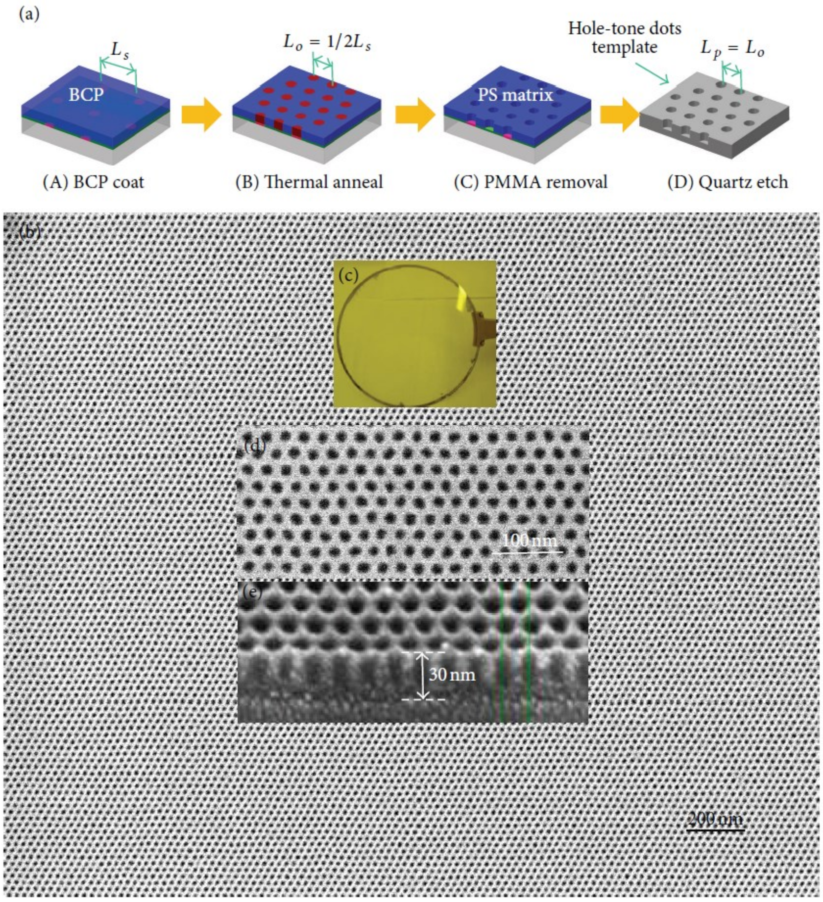

Fig. 1.4.4 (a) Schematic illustration of nanopore fabrication on fused silica substrate using PS-b-PMMA. (b) Large-scale SEM image of a 1.0 Tbit/in2 nanopore patterned substrate with 27.0 nm in pitch. (c) A fabricated 6 inch fused silica template. (d) Magnified SEM image of nanopore patterned substrate and (e) cross-sectional SEM image of the substrate [40].

As described above, the physical fabrication process demonstrated the fabrication process of nanodot arrays with Tbit/in^2 areal density. However, because magnetic layer is patterned by etching process, the magnetic properties of etched area is deteriorated by the damage during the process, also nanodots should contain random grain boundaries originated from the initial magnetic layer. In order to achieve high SNR and magnetic properties in BPM system, fabrication of highly uniform nanodot arrays is essential, because defects [41], grain boundaries [42], cause the variation in the switching field of each dot, resulting in the noise to degrade the recording performance.

1.4.2 Self-Assembly of Nanoparticles

Self-assembly of nanoparticles with high magnetic anisotropy was expected as an alternative approach to potential use in BPM system [43-45]. Sun et al. first demonstrated the formation of assembled arrays of FePt nanoparticles having diameter of 4.0 nm with narrow size distribution of 5.0 % [44]. As mentioned in section 1.3, FePt exhibit high K_u value, thus it can maintain magnetic anisotropy with small volume, which makes it suitable for the application in nanoparticles with a size of few nano-meters. FePt nanoparticles were prepared by using combination of oleic acied and oleyl amine to stabilize the monodisperse FePt nanoparticles. Synthesis of nanoparticles was carried out by reduction of $Pt(acac)_2$ and by decomposition of $Fe(CO)_5$ in high temperature solutions. The spacing of nanoparticles can be controlled by changing the ligand of FePt colloids; 6.0 nm FePt nanoparticles with a spacing of 4.0 nm and 1.0 nm with different ligands were fabricated. In addition, arrays of 4.0 nm FePt nanoparticles without agglomeration were observed upon annealing at 560 ^{o}C for 30 min; the particles were single crystal with $L1_0$-ordered structure. In addition, Hachisu et al. successfully demonstrated the uniform arrangement of 5.6 nm FePt nanoparticles by using (3-mercaptopropyl) trimethoxysilane, MPTMS as an interlayer between nanoparticles and substrate with a geometrical structure prepared by UV-NIL as shown in Fig. 1.4.5 [45].

Although, high areal density was achieved in the arrays of self-assembled nanoparticles, orienting the magnetic easy axis of particles in the perpendicular direction is considered as critical issue for the application in BPM system. Using magnetic field during the post annealing process was attempted to guide the magnetic easy axis of nanoparticles [43], however, there were no successful reports.

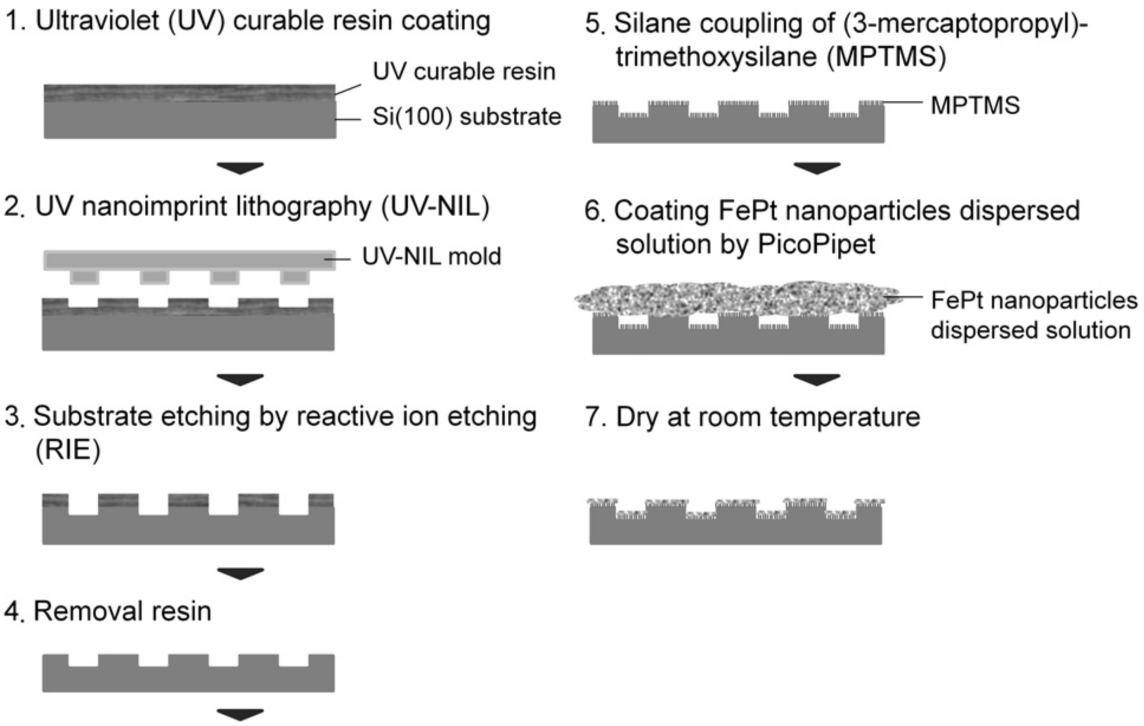

Fig. 1.4.5 Scheme of uniform arrangement of FePt nanoparticle by hole-patterns and chemical bonding. Process 1–4: the preparation of hole-patterns on Si (100) substrate, and process 5–7: the immobilization and arrangement of FePt nanoparticles on the hole-patterns with modified MPTMS [45]. Copyright 2012 by J. Magn. Magn. Mater. Reproduced with permission of J. Magn. Magn. Mater. via Copyright Clearance Center.

1.4.3 Electrocheimcal Fabrication Process

Electrochemical fabrication processes have been widely used as a fabrication method of metal films to functionalize material surface, such as corrosion resistance and abrasion resistance. Due to its precise deposition control at nanoscale as well as highly uniform formation on complex structure, it has been applied in, for example, fabrication process of high density mounting board and ultra-fine wiring in ultra large scale integration (ULSI) [46], and thin film magnetic head for hard disk drive (HDD) [47]. In this process it is possible to deposit metal at electrochemically active site, in principal it can be assumed as feasible fabrication process of nanostructured devices.

In this section, the outlines and features on electrodeposition process, which is used in this thesis for the fabrication of nanodot arrays, are overviewed.

Electrodeposition process of ferromagnetic nanostructures has attracted attention for the applications in fields of magnetics [48, 49] and biomedical device [50]. Especially, fabrication of ferromagnetic nanowires was extensively studied, where ordered anodic alumina oxide (AAO) templates with high aspect ratio were commonly used. Several groups reported the fabrication of ferromagnetic nanowires such as Ni, Co, and Fe with AAO templates, in which coercivity was tuned by changing the pore diameter and aspect ratio [51-53]. Fabrication of nanowires with high K_u value, such as CoPt and FePt, was also attempted by utilizing AAO template [54-56]. Haung et al. have first demonstrated the fabrication of CoPt and FePt nanowires with a near stoichiometric composition by using a simple solution of cobalt/iron chloride and platinum chloride. And nanowires with 100 nm diameter showed coercivity of 3.0 to 6.0 kOe after annealing at 700 ^{o}C [54]. Dahmane et al. also reported the fabrication of equiatomic CoPt and FePt nanowires embedded into AAO template with diameter of 60 nm and interpore distance of 100 nm and thickness of 40 μm [56]. Upon annealing at 700 ^{o}C, coercivity up to 11 kOe was obtained in both CoPt and FePt with $L1_0$ structure. Yasui et al. successfully demonstrated the improvement of coercivity of $L1_0$-CoPt nanowires with diameter of 100 nm and interpore distance of 100 nm and thickness of 500 nm by controlling the crystal orientation of CoPt with different types of underlayers [57]. In the case of W underlayer, CoPt showed random c-axis crystal orientation, whereas (001) orientation of $L1_0$-CoPt was obtained when (001) oriented Pt underlayer was applied. This improvement in the c-axis crystal orientation induced perpendicular mangetic anisotropy to increase coercivity up to 7.4 kOe with squareness of 0.96 after annealing at 700 °C.

For the practical use of electrochemical fabrication process in BPM system, several reports utilized lithography technique in fabrication of nanodot arrays [58-62]. Figure 1.4.6 shows the typical flowchart of the fabrication processes of nanodot arrays utilizing nanoimprint lithographic technique [62]. Oshima et al. demonstrated the fabrication of Co nanodot arrays with 30 nm diameter, 100 nm pitch, and 350 nm height with coercivity of 1.9 kOe, and dynamic write/read measurement of the nanodot arrays was successfully demonstrated that the nanodots showed single-domain behavior in a perpendicular direction [63]. Sohn et al. fabricated hcp-CoPt nanodot arrays with 25 nm in diameter and 50 nm in pitch by combining UV-NIL and electrodeposition [64]. In this work, Ru underlayer, which has small lattice mismatch between CoPt, was applied to induce the perpendicular magnetic anisotropy of deposited CoPt, and coercivity of 2.5 kOe was achieved.

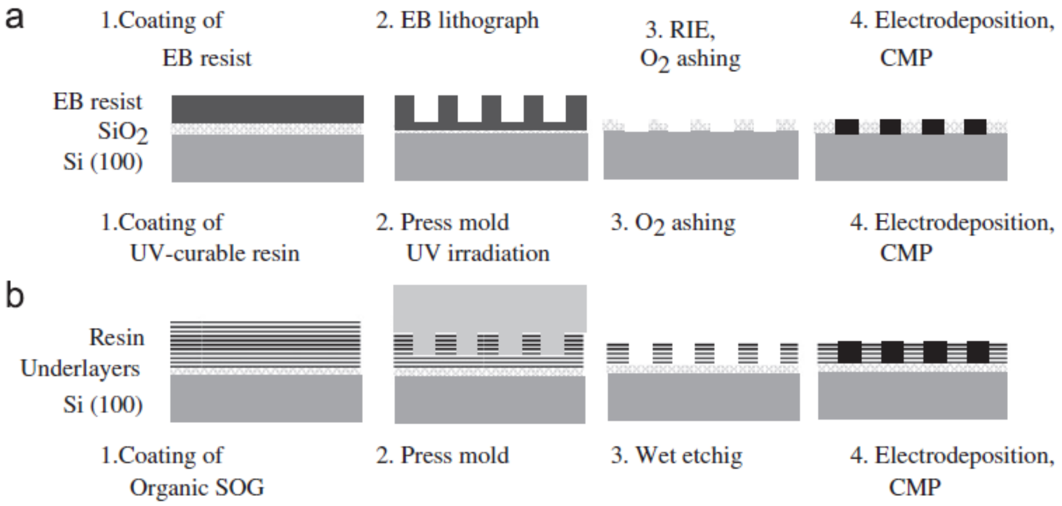

Fig. 1.4.6 Schematic illustration of fabrication process of nanodot arrays with (a) EBL and (b) UV-NIL [62].

Ouchi et al. also utilized UV-NIL for the fabrication of hcp-CoPt nanodot arrays [62, 65, 66]. The fabrication of CoPt nanodot arrays were performed on glass disk substrate with a practical construction in perpendicular magnetic recording media consist of softmagnetic underlayer (SUL) and intermediate layer; 100 nm-thick CoZrNb layer was used as SUL and 1.0-2.0 nm-thick (111) oriented Cu layer was used as an intermediate layer, which have close lattice constant with hcp-CoPt. CoPt nanodot arrays were uniformly fabricated with clear stacking of hcp lattice in perpendicular direction (Fig. 1.4.7) [66]. This uniform crystal orientation induced by Cu intermediate layer increased cercivity and M/M_s of nanodot arrays up to 5.4 kOe and 0.84. In addition, Ouchi et al. have demonstrated fabrication of CoPt nanodot arrays by combining EBL and electrodeposition to fabricate nanodot arrays with Tbit/in^2 areal density. Based on the detail optimization of EBL conditions, such as conditions and process of development, nanopore patterned substrate with 10 nm diameter and 25 nm pitch, which corresponds to 1.0 Tbit/in^2 areal density was successfully fabricated on Si substrate with (111) oriented Cu intermediate layer. The nanopore patterned substrate was further utilized for the electrodeposition of CoPt, and CoPt nanodot arrays with 1.0 Tbit/in^2 was successfully demonstrated. This was the first and the only study that achieved the fabrication of nanodot arrays with Tbit-level areal recording density by electrochemical fabrication process.

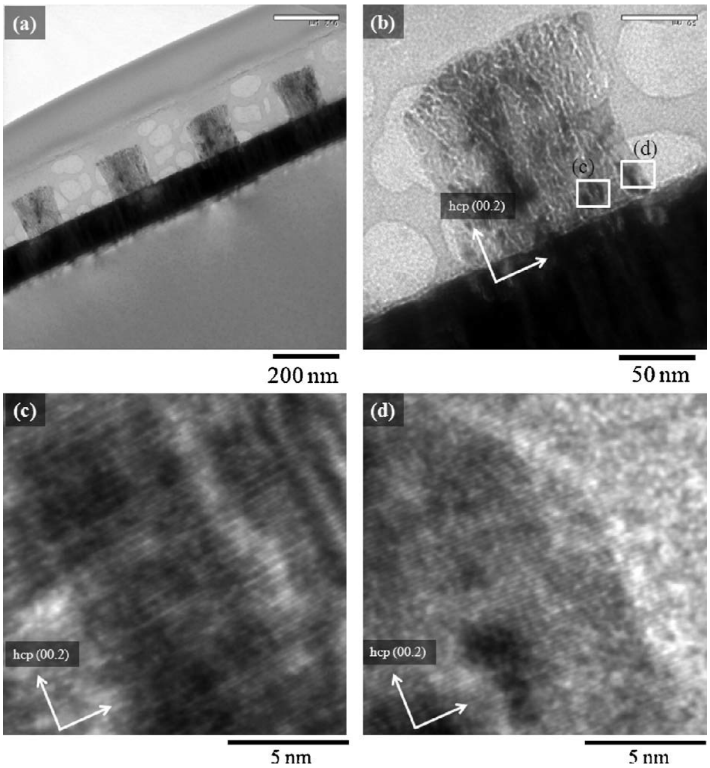

Fig. 1.4.7 Cross-sectional TEM images of CoPt nanodot arrays with 120 nm height, 150 nm diameter ans 300 nm pitches: (a, b) low magnification image and (c, d) high magnification image at the 20 nm height from the substrate [66].

1.5 Strategy of This Study

As described, bit patterned media (BPM) is a promising candidate for the application in ultra-high density magnetic recording media. For the fabrication of BPM, physical fabrication process and self-assembly of magnetic nanoparticles have been extensively studied. However, the above mentioned approaches face difficulties in controlling the grain boundaries, the damage due to etching of the magnetic layer, or the crystal orientation of the nanoparticles, which cause media noise to degrade the recording performance. On the other hand, electrochemical fabrication process of ferromagnetic nanodot arrays has been proposed as an alternative approach due to its high areal selectivity and deposition uniformity at the nanoscale. Despite many studies on the electrodeposition of ferromagnetic nanostructures, such as nanowires, have been reported, there is no report of fabrication of nanodot arrays with Tbit-level areal density that exhibit sufficient coercivity for the application in BPM. Along with the increase in areal density, nanodots are miniaturized to 10 nm in diameter, therefore, to control the magnetic properties and deposition uniformity, it is significant to understand the mechanism of initial deposition stages of ferromagnetic metals inside the nanopore. However, little attention has been paid to the formation mechanisms inside the nanopore.

Against these backgrounds, this study aims to fabricate Tbit/in^2 nanodot arrays with high coercivity by electrochemical process based on the detailed analyses of initial deposition stage and crystal structure of ferromagnetic nanodots. Especially, nucleation and growth process was analyzed to achieve nanodot arrays consist of single crystal structure, which is highly desirable for the application in BPM owing to its high coercivity and high crystallinity. Because hcp-CoPt exhibit high coercivity without annealing process, hcp-CoPt was utilized in fundamental studies of analyses of initial deposition stage and fabrication of nanodot arrays. In addition, to further demonstrate the applicability of electrochemical fabrication process, $L1_0$-FePt was focused on as a promising candidate for high K_u materials.

References

[1] EMC Digital Universe with Research & Analysis by IDC, April 2014, "The Digital Universe of Opportunities: Rich Data and the Increasing Value of the Internet of Things", available: http://www.emc.com/leadership/digital-universe/2014iview/executive-summary.htm, [Accessed 13 November 2016]

[2] T. Coughlin, 22 November 2014, "100 TB HDD and A New Spin on Storage", Forbes, available: http://www.forbes.com/sites/tomcoughlin/2014/11/22-100-tb-hdds-and-a-new-spin-on-storage/#17bed32c279f, [Accessed 13 November 2016]

[3] D. Weller and A. Moser, *IEEE Trans. Magn.*, 35 (1999) 4423.

[4] Li Zhang, Y.K.Takahashi, A.Perumal, and K.Hono, *J. Magn. Magn. Mater.*, 322 (2010) 2658.

[5] Y. Shiroishi, K. Fukud, I. Tagawa, H. Iwasaki, S. Takenoiri, H. Tanaka, H. Mutoh, and N. Yoshikawa, *IEEE Trans. Magn.*, 45 (2009) 3816.

[6] H. J. Richter, A. Y. Dobin, O. Heinonen, K. Z. Gao, R. J. M. v. d. Veerdonk, R. T. Lynch, J. Xue, D. Weller, P. Asselin, M. F. Erden, and R. M. Brockie, *IEEE Trans. Magn.*, 42 (2006) 2255.

[7] R. Wood, M. Williams, A. Kavcic, and J. Miles, *IEEE Trans. Magn.*, 45 (2009) 917.

[8] M. H. Kryder, E. C. Gage, T. W. McDaniel, W. A. Challener, R. E. Rottmayer, G. Ju, Y. T. Hsia, M. F. Erden, *Proc. IEEE*, 96 (2008) 1810.

[9] D. Weller, O. Mosendz, G. Parker, S. Pisana, and T. S. Santos, *Phys. Status Solidi A*, 210 (2013) 1245.

[10] J-G. Zhu, X. Zhu, and Y. Tang, *IEEE Trans. Magn.*, 44 (2008) 125.

[11] Y. Nozaki, M. Ohta, S. Taharazako, K. Tateishi, S. Yoshimura, and K. Matsuyama, *Appl. Phys. Lett.*, 91 (2007) 082510.

[12] Y. Yamada, T. Suzuki, H. Kanazawa, and J.C. Ostermann, *J. Appl. Phys.*, 85 (1999) 5094.

[13] R.A. Ristau, K. Barmak, L.H. Lewis, K.R. Coffey, J.K. Howard, *J. Appl. Phys.*, 86 (1999) 4527.

[14] D. Waller, A. Monser, L. Folks, M. E. Best, W. Lee, M. F. Toney, M. Schwickert, J. U. Thiele, and M. F. Doerner, *IEEE Trans. Magn.*, 36 (2000) 10.

[15] Y. Kubota, L. Folks, and E.E. Marinero, *J. Appl. Phys.*, 84 (1998) 6202.

[16] J. F. Herbst, J. J. Croat, and F. E. Pinkerton, *Phys. Rev. B*, 29 (1984) 4176.

[17] T. Sato, H.Kato, T.Shima, Y.K.Takahashi, and K.Hono, *J. Magn. Magn. Mater.*, 323 (2011) 163.

[18] E.E. Fullerton, J. S. Jiang, Christine Rehm, C. H. Sowers, S. D. Bader, J. B. Patel, and X. Z. Wu, *Apply. Phys. Lett.*, 71 (1997) 1579.

[19] E.E. Fullerton, C.H. Sowers, J.P. Pearson, S.D. Bader, X.Z. Wu, and D. Lederman, *Apply. Phys. Lett.*, 69 (1996) 2438.

[20] E.A. Dobisz, Z.Z. Bandic, T-W. Wu, and T. Albrecht, *Proc. IEEE*, 96 (2008) 1836.

[21] J.C. Lodder, *J. Magn. Magn. Mater.*, 272-276 (2004) 1692.

[22] B. D. Terris and T. Thomas, *J. Phys. D: Appl. Phys.*, 38 (2005) R199.

[23] T. R. Albercht, H. Arora, V. A.-Vitikkate, J.-M. Beaujour, D. Bedau, D. Berman, A. L. Bogdanov, Y.-A. Chapuis, J. Cushen, E. E. Dobisz, G. Doerk, H. Gao, M. Grobis, B. Gurney, W. Hanson, O. Hellwig, T. Hirano, P.-O. Jubert, D. Kercher, J. Lille, Z. Liu, C. M. Mate, Y. Obukhov, K. C. Patel, K. Rubin, R. Ruiz, M. Schabes, L. Wan, D. Weller, T.-W. Wu, and E. Yang, *IEEE Trans. Magn.*, 51 (2015) 1.

[24] M. Albrecht, C.T. Rettner, A. Moser, M.E. Best, and B.D. Terris, *Apply. Phys. Lett.*, 81 (2002) 2875.

[25] M.K. Grobis, O. Hellwig, T. Hauet, E. Dobisz, and T.R. Albrecht, *IEEE Trans. Magn.*, 47 (2011) 6.

[26] J. Moritz, S. Landis, J.C. Toussaint, P.B-Guillemaud, B. Rodmacq, G. Casali, A. Lebib, Y. Chen, J. P. Nozieres, and B. Dieny, *IEEE Trans. Magn.*, 38 (2002) 1731.

[27] J.K.W. Yang, Y. Chen, T. Huang, H. Duan, N. Thiyagarajah, H.K. Hui, S.H. Leong, and V. Ng, *Nanotechnology*, 22 (2011) 385301.

[28] C.T. Rettner, S. Andres, T. Thomson, M. Albrecht, Y. Ikeda, M.E. Best, and B.D. Terris, *IEEE Trans. Magn.*, 38 (2002) 1725.

[29] C.T. Rettner, M.E. Best, and B.D. Terris, *IEEE Trans. Magn.*, 37 (2001) 1649.

[30] T. Aoyama, S. Okawa, K. Hattori, H. Hatate, Y. Wada, K. Uchiyama,T. Kagotani, H. Nishio, and I. Sato, *J. Magn. Magn. Mater.*, 235 (2001) 174.

[31] T.R. Albrecht, D. Bedau, E. Dobisz, H. Gao, M. Grobis, O. Hellwig, D. Kercher, J. Lille, E. Marinero, K. Patel, R. Ruiz, M.E. Schabes, L. Wan, D. Weller, and T-W. Wu, *IEEE Trans.*

Magn., 49 (2013) 773.

[32] S. Y. Chou, P. R. Krauss, and P. J. Renstrom, *Apply. Phys. Lett.*, 81(1995) 3114.

[33] J.I. Martın, J. Nogues, K. Liu, J.L. Vicente, and I.K. Schuller, *J. Magn. Magn. Mater.*, 256 (2003) 449.

[34] L.J. Guo, *Adv. Mater.*, 19 (2007) 495.

[35] S. Hosaka, H. Sano, M. Shirai, and H. Sone, *Apply. Phys. Lett.*, 89 (2006) 223131.

[36] X.M. Yang, Y. Xu, K. Lee S. Xiao, D. Kuo, and D. Weller, *IEEE Trans. Magn.*, 45 (2009) 833.

[37] X.M. Yang, S. Xiao, W. Wu, Y. Xu, K. Mountfield, R. Rottmayer, K. Lee, D. Kuo, D. Weller, *J. Vac. Sci. Technol. B*, 25 (2007) 2202.

[38] C.A. Ross and J.Y. Cheng, *MRS Bulletin*, 33 (2008) 838.

[39] S.O. Kim, H. H. Solak, M.P. Stoykovich, N.J. Ferrier, J.J. de Pablo, and P.F. Nealey, *Nature*, 24 (2003) 411.

[40] X.M. Yang, S. Xiao, Y. Hsu,M. Feldbaum, K. Lee, and D. Kuo, *J. Nanomater.*, 2013 (2013) 1.

[41] J.M. Shaw, S.E. Russek, T. Thomson, M.J. Donahue, B.D. Terris, O. Hellwig, E. Dobisz, and M.L.Schneider, *Phys. Rev. B*, 78 (2008) 024414.

[42] Y. Kamata, A. Kikitsu, H. Hieda, M. Sakurai, K. Naito, J. Bai, and S. Ishio, *Jpn. J. Appl. Phys.*, 46 (2007) 999.

[43] J-P. Wang, *Proc. IEEE*, 96 (2008) 1847.

[44] S. Sun, C. B. Murray, D. Weller, L. Folks, A. Moser, *Science*, 287 (2000) 1989.

[45] T. Hachisu, W. Sato, S. Ishizuka, A. Sugiyama, J. Mizuno, T. Osaka, *J. Magn. Magn. Mater.*, 324 (2012) 303.

[46] P.C. Andricacos, C. Uzoh, J.O. Dukovic, J. Horkans, H. Deligianni, *IBM J. Res. Develop.*, 42 (1989) 567.

[47] T. Osaka, *Electrochim. Acta*, 45 (2000) 3311.

[48] S-F. Chen, H.H.Wei, C-P. Liu, C.Y. Hsu, and J.C.A Huang, *Nanotechnology*, 21 (2010) 425602.

[49] K. Nielsch, R.B. Wehrspohn, J. Barthel, J. Kirschner, S.F. Fischer, H. Kronmuller, T. Schweinbock, D. Weiss, and U. Gosele, *J. Magn. Magn. Mater.*, 249 (2002) 234.

[50] F. Byrne, A.P-Mello, A. Whelan, B.M. Mohamed, A. Davies, Y. K. Gunko, J.M.D. Coey, and Y. Volkov, *J. Magn. Magn. Mater.*, 321 (2009) 1341.

[51] H. Zeng, R. Skomski, L. Menon, Y. Liu, S. Bandyopadhyay, and D.J. Sellmyr, *Phys. Rev. B*, 65 (2002) 134426.

[52] H. Wu, R. Zhang, X. Liu, D. Lin, and W. Pan, *Chem. Mater.*, 19 (2007) 3506.

[53] M. Vazquez and L. G. Vivas, *Phys. Status Solidi B*, 248, (2011) 2368.

[54] Y. H. Huang, H. Okumura, G. C. Hadjipanayis, and D. Weller, *J. Appl. Phys.*, 91 (2002) 6869.

[55] S.Z. Chu, S. Inoue, K. Wada, K. Kurashima, *Electrochim. Acta*, 51 (2005) 820.

[56] Y Dahmane, L Cagnon, J. Voiron, S. Pairis, M. Bacia, L. Ortega, N. Benbrahim, and A. Kadri, *J. Phys. D: Appl. Phys.*, 39 (2006) 4523.

[57] N. Yasui, A. Imada, and T. Den, *Appl. Phys.Lett.*, 83 (2003) 3347.

[58] C.A. Ross, H.I. Smith, T. Savas, M. Schattenburg, M. Farhoud, M. Hwang, M. Walsh, M.C. Abraham, and R.J. Ram, *J. Vac. Sci. Technol. B*, 17 (1999) 3168.

[59] C. A. Ross, M. Hwang, M. Shima, J.Y. Cheng, M. Farhoud, T.A. Savas, H. I. Smith, W. Schwarzacher, F.M. Ross, M. Redjdal, and F.B. Humphrey, *Phys. Rev. B*, 65 (2002) 144417.

[60] W. Wu, B. Cui, X-Y. Sun, W. Zhang, L. Zhuang, L. Kong, and S.Y. Chou, *J. Vac. Sci. Technol. B*, 16 (1998) 3825.

[61] L.J. Heyderman, H.H. Solak, C. David, D. Atkinson, R.P. Cowburn, and F. Nolting, *Appl. Phys.Lett.*, 85 (2004) 4989.

[62] T. Ouchi, Y. Arikawa, T. Homma, *J. Magn. Magn. Mater.*, 320 (2008) 3104.

[63] H. Oshima, H. Kikuchi, H. Nakao, K. Itoh, T. Kamimura, T. Morikawa, K. Matsumoto, T. Umada, H. Tamura, K. Nishio, and H. Masuda, *Appl. Phys. Lett.*, 91 (2007) 022508.

[64] J-S. Sohn, D. Lee, E. Cho, H-S. Kim,B-K. Lee, M-B. Lee, and S-J Suh, *Nanotechnology,* 20 (2009) 025302.

[65] T. Ouchi, Y. Arikawa, T. Kuno, J. Mizuno, S. Shoji, T. Homma, *IEEE Trans. Magn.*, 46 (2010) 2224.

[66] T. Ouchi, Y. Arikawa, Y. Konishi, T. Homma, *Electrochim. Acta*, 55 (2010) 8081.

Chapter 2

Fine Structural Control of Electrodeposited CoPt Nanodot Arrays with Tbit/in^2 Areal Density

2.1 Introduction

In BPM with Tbit-level areal recording density, high and uniform coercivity for each ferromagnetic nanodot is of extreme importance to achieve thermal stability and low media noise. When the morphology or crystal orientation is different for each nanodot, coercivity becomes non-uniform, thus resulting in the degradation of the magnetic properties of entire nanodot arrays. Thus, it is significant to fabricate nanodot arrays with highly uniform crystal orientations from the initial deposition stages. In the previous study, Ouchi et al. demonstrated the fabrication of CoPt nanodot arrays with 25 nm in pitch, which corresponds to 1.0 Tbit/in^2 areal density by electrodeposition combining electron beam lithography. However, there has been no report of fabrication of nanodot arrays with Tbit-level recording density with sufficient coercivity and deposition uniformity, which is applicable to BPM.

In electrodeposition, diffusion of metal ions is strongly influencing the surface morphology and the thickness of the deposited film, especially when the deposition reaction proceeds under diffusion limited conditions, films having rough surface with a dendritic texture are formed. Also, in the case of alloy electrodeposition, such as CoPt electrodeposition, the difference of diffusion in each metal ion causes the variation in composition of the deposited films. Thus, to deposit films with uniform surface morphology and composition it is extremely important to control the diffusion of reactive metal ions to the electrode surface. Pulse electrodeposition and electrodeposition under forced convection conditions are known as a means of fabricating uniform deposits by controlling the diffusion layer of deposited metal ions.

In this chapter, in order to achieve high coercivity of CoPt nanodot arrays with Tbit-level recording density, crystal structure was controlled by controlling the diffusion of metal ions with the application of rotating electrode. In addition, the crystal growth of ultra-fine nanodot arrays with 35 nm in pitch was analyzed in detail to achieve high crystallinity of nanodot arrays with high coercivity.

2.2 Experimental

2.2.1 Fabrication Process of Nanopore Patterned Substrate by Electron Beam Lithography

A 60 nm-thick and (002) oriented Ru layer was sputter-deposited onto a Ti adhesion layer on top of an n-type Si (100) wafer, which was provided from the laboratory of Prof. Zngari in University of Virginia. Since the a-axis lattice spacing of (002) oriented Ru (0.269 nm) is close to that of hcp-CoPt (0.257 nm), Ru is the most commonly used element as an underlayer to induce the perpendicular magnetic anisotropy of the CoPt alloy [1-3]. Prior to the deposition of the nanodot arrays, nanopore patterns were fabricated onto the Ru substrate using an electron beam apparatus (ELS-7500, ELIONIX). First, the surface of the Ru layer was rinsed with acetone, ethanol, and ultra-pure water (UPW) for 5 min, respectively, using an ultrasonic bath (sonicator). An electron beam resist was then spin-coated onto the substrate at 5000 rpm to set the thickness of the resist to 30 nm. A mixture of the positive-type electron beam resist (ZEP520A-7, Nippon Zeon) and diluent (ZEP-A, Nippon Zeon) with a ratio of 1 to 2, and negative-type electron beam resist (TEBN-1, Tokuyama), which has a higher resolution than positive type resist, were utilized. The nanopore patterns with 15 and 35 nm in diameter and pitch were fabricated over patterned area of 105 μm^2 by exposing to electron beam. After the exposure, development was performed using isopropanol as a developer, and the surface of the substrate was rinsed with UPW. To remove the residue inside the nanopore remaining after the development, the patterned substrate was exposed to excimer UV irradiation for 30 s prior to electrodeposition. The process conditions of EBL are summarized in Table 2.1.

Table 2.2.1 Operating conditions of electron beam lithography

Resist	ZEP520A-7 : ZEP-A = 1:2 (positive-type EB resist)	TEBN-1 (negative-type EB resist)
Spin coat rate	5000 rpm, 60 s	5000 rpm, 60 s
Prebake	180 °C, 3 min	110 °C, 3 min
Thickness of resist	30 nm	25 nm
Accelerating voltage	50 kV	50 kV
Beam current	20 pA	20 pA
Dose value	3.0-10 fC / dot	0.022-0.040 fC / dot
Developer	IPA	IPA
Developing time	5 s	30 s
Developing temperature	5 °C	RT
Rinse	UPW	UPW

2.2.2 Fabrication Process of CoPt Nanodot Arrays

In order to deposit hcp-CoPt, CoPt alloy continuous films and nanodot arrays were electrodeposited at constant potential. The reduction of Co and Pt metal ions take place at negative potential where hydrogen evolution reaction occurs, thus alloy composition was tuned by selectively adjusting the potential to minimize the effect of hydrogen evolution. Also, the overpotential is a strong function of nucleation and growth of deposited metals, which allows to control the grain size or crystal structure of the deposited films. Thus, in order to control the alloy composition and crystal structure of the deposited films, we employed potentiostatic method. The electrolyte shown in Table 2.2 was used for the CoPt electrodeposition. The bath temperature was 303 K, and the pH was adjusted to 5.2 by adding diluted NaOH. All electrochemical measurements were performed in a three-electrode cell using a potentiostat (HZ-5000, Hokuto Denko); consisting of a Co wire, an Ag/AgCl electrode, and a sputter deposited Ru substrate as the counter electrode, reference electrode, and working electrode, respectively. To deposit uniform alloy films and nanodot arrays, CoPt was electrodeposited using a rotating electrode (HR-300, Hokuto Denko); the surface area was 0.503 cm^2 (ϕ 8.0 mm) and the rotating speed was optimized to minimize the deterioration of the nanopore patterned substrate while also controlling the mass transfer of the metal ions to the electrode surface. Ga-In paste was applied between the backside of the substrate and the rotating electrode to obtain sufficient conductivity.

The crystal structure of the deposited films was investigated by an X-ray diffractometer (XRD, Rint-UltimaIII, Rigaku) with Cu Kα radiation, and the structure of the deposited nanodot arrays was observed by a transmission electron microscope (TEM, JEM-2010, JEOL). The morphology of the deposited CoPt films and nanodot arrays was observed by a high-resolution scanning electron microscope (HRSEM, S5500, Hitachi High-Tech.); all the nanodot arrays were observed after removing all the resists by exposing the samples to excimer UV irradiation for 2.0 min and rinsing with ethanol and UPW to avoid sample charge up. The alloy composition was determined by inductively-coupled plasma mass spectrometry (ICP-MS, 7700x, Agilent). The thickness of the deposited films was measured using surface profiler (P-15, KLA-Tencor). The coercivity of the deposited films and nanodot arrays was measured using polar magneto-optical Kerr effect equipment (BH-810CPC-WU, NEOARK and BH-618PL-AU, NEOARK); the diameter of the laser spot area was 1.0 mm and 100 μm for BH-810CPC-WU and BH-618PL-AU, respectively. Schematic image of fabrication process of nanodot arrays was shown in Fig. 2.1.

Table 2.2.2 Bath compositions and electrodeposition conditions of Co-Pt

Chemicals	Concentration / mM
$Pt(NO_2)_2(NH_3)_2$	1.2-3.0
$CoSO_4 \cdot 7H_2O$	100
$(NH_4)_2C_6H_6O_7$	100
NH_2CH_2COOH	100
Bath temperature	30 °C
pH	5.2 (adjusted by NaOH)
Reference electrode	Ag / AgCl
Counter electrode	Co

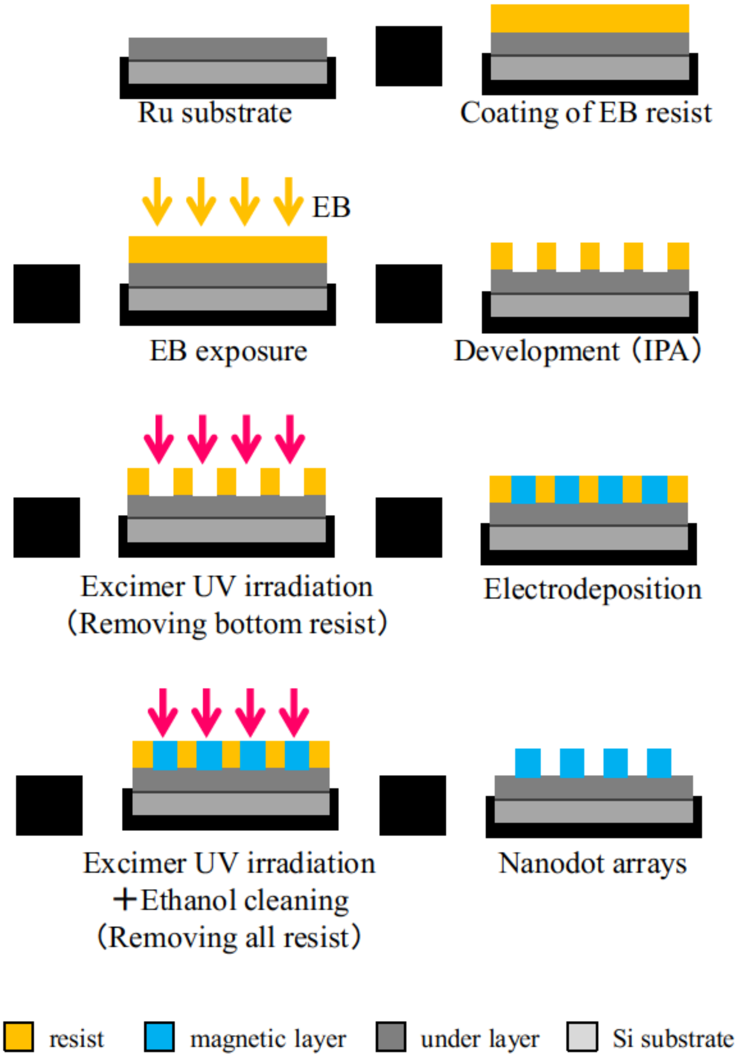

Fig. 2.2.1 Schematic image of fabrication process of nanodot arrays

2.3 Fabrication of Nanopore Patterned Substrate with Tbit/in^2 Areal Density

2.3.1 Formation of Nanopore patterned substrate on Ru underlayer

In the previous study, Ouchi et al. developed the fabrication process of nanopore patterned substrate with electron beam lithography on the Cu underlayer by the detailed analyses of effects of the dose values and developing processes on the formation of nanopore patterns. In this study, Ru was applied as an underlayer of CoPt to induce the perpendicular magnetic anisotropy [1-3]. Therefore, fabrication process, such as prebake temperature, was optimized for the fabrication of nanopores on Ru substrate. Prebake process is an important process to evaporate the excess solvent and to harden the resist, which affects the resolution of exposure. When the solvent remains in the coated resist, sensitizer will be prevented from the light, which significantly decreases the photosensitivity of the resist. Thus, it is significant to bake the resist in adequate temperature to prevent under-bake the resist; the optimum prebake temperature of ZEP520A-7 is reported as 170~200 ^{o}C for 2.0~5.0 min [4]. Considering this point, coated resist was prebaked at 180 ^{o}C for 3.0 min.

Figure 2.3.1 compares the SEM images of nanopores with 25 nm in pitch fabricated with prebake temperature of 90 ^{o}C for 3 min and 180 ^{o}C for 3.0 min, respectively. The dose values were set to 5.0 fC/dot, 4.0 fC/dot, and 3.0 fC/dot, which were optimized in previous studies. The diameters of the nanopores were 10 nm, 8.0 nm, and 7.0 nm, respectively. The nanopores were partially overlapped to the neighbor nanopores with the lower prebake temperature, whereas the nanopore patterns were uniformly fabricated over the patterned area in all dose values with higher prebake temperature, indicating the improvement in the photosensitivity of the resist. Thus, in this study, prebake was conducted with 180 ^{o}C for 3.0 min in the case of positive-type resist.

Figure 2.3.2 shows the SEM images of nanopores with 100 nm and 35 nm in pitch fabricated with various dose values. From Figs. 2.3.1 and 2.3.2, the diameter of the nanopore was increased with narrower pitch due to the increase in backscattering of the electron beam; the diameters of the nanopore were 8.0 nm and 10 nm, for the nanopores with 100 nm and 35 nm in pitch, respectively at dose values of 5.0 fC/dot. By controlling the dose values the diameter of the nanopores was controlled in each nanopores with different pitches.

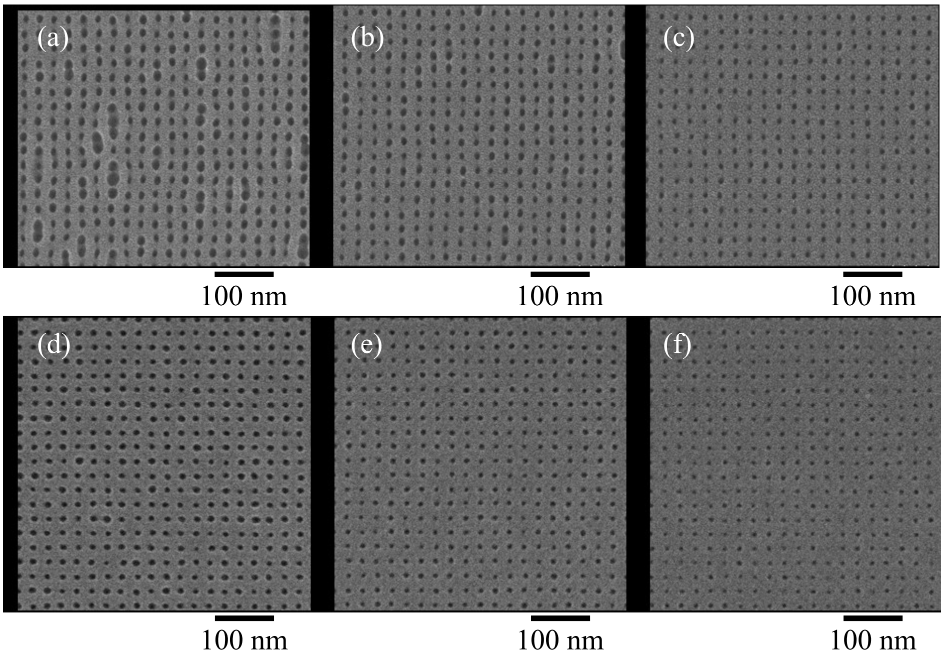

Fig. 2.3.1 SEM images of nanopores with 25 nm in pitch fabricated with prebake temperature of (a-c) 90 ^{o}C and (d-f) 180 ^{o}C for 3 min. The dose values were (a, d) 5.0 fC/dot, (b, e) 4.0 fC/dot, and (c, f) 3.0 fC/dot.

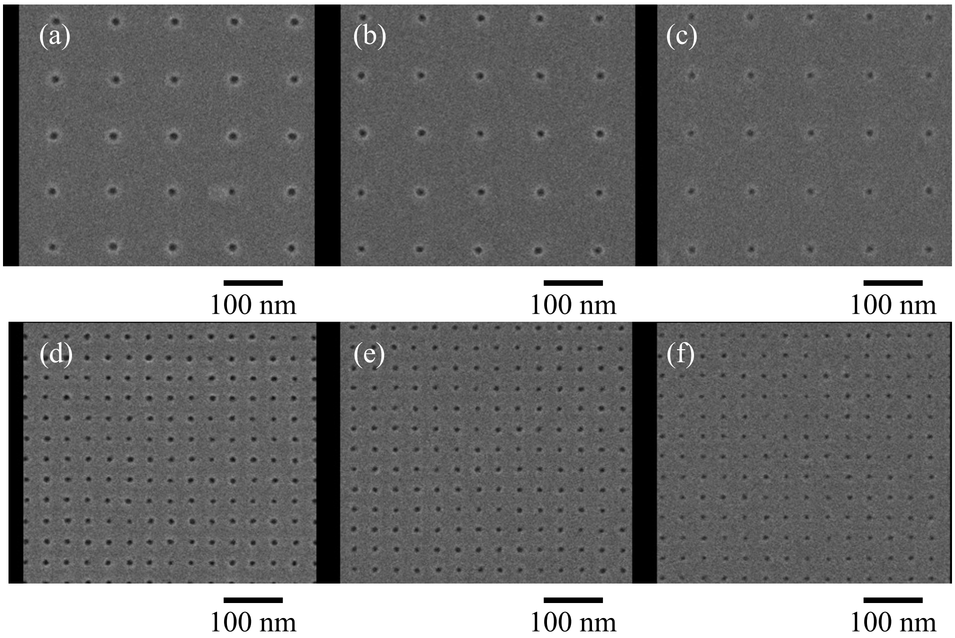

Fig. 2.3.2 SEM images of nanopores with (a-c) 100 nm and (d-f) 35 nm in pitch. The dose values were (a) 10 fC/dot, (b) 7.0 fC/dot, and (c) 5.0 fC/dot for 100 nm in pitch, and (d) 5.0 fC/dot, (e) 4.0 fC/dot , and (f) 3.0 fC/dot for 35 nm in pitch.

Based on the above results, CoPt was deposited with -0.9 V (vs. Ag/AgCl) for 10 s inside the nanopores fabricated with various dose values to fabricate nanodot arrays with 35 nm and 25 nm in pitch; corresponding SEM images are shown in Fig 2.3.3. Prior to the electrodeposition, the nanopore patterned substrate was exposed to excimer UV irradiation for 30 s. At smaller dose amount CoPt was partially deposited to form nano-uniform nandots in both pitches, suggesting that the dose values were insufficient to fabricate nanopores. At higher dose values, CoPt was uniformly deposited inside the nanopore with 35 nm in pitch, whereas the diameter of each nanodot was non-uniform in the case of 25 nm in pitch due to the overlap of the neighboring nanopores caused by the backscattering of the electron beam. From these results, it was suggested that the fabrication of nanopore with Tbit/in^2 is difficult to achieve by the application of positive-type resist (ZEP520A-7) owing to the difficulties in controlling the backscattering of the electron beam.

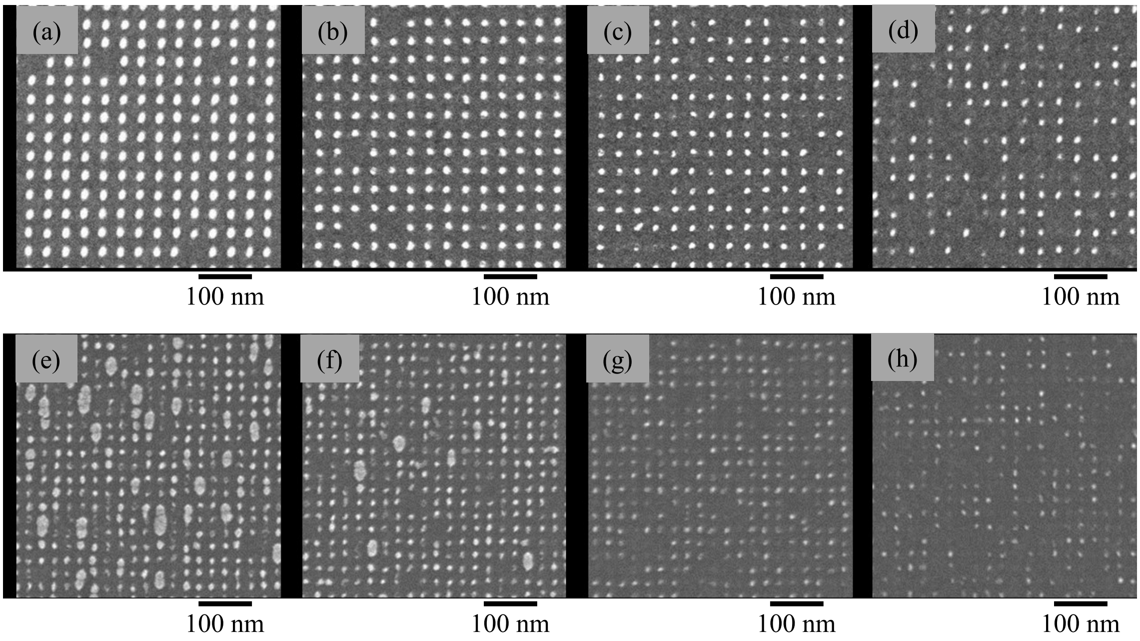

Fig. 2.3.3 SEM images of CoPt nanodot arrays with (a-d) 35 nm and (e-h) 25 nm in pitch. The dose values were (a) 10 fC/dot, (b) 7.0 fC/dot, (c) 5.0 fC/dot, and (d) 4.0 fC/dot for 35 nm in pitch, and (e) 6.0 fC/dot, (f) 5.0 fC/dot, (g) 4.0 fC/dot, and (h) 3.5 fC/dot for 25 nm in pitch.

In order to fabricate nanodot arrays with Tbit/in^2 areal density, negative-type resist (TEBN-1) was applied. Bilenberg et al. reported that the TEBN-1 exhibits high resolution in fabricating nanopattern with linewidth of 10 nm [5]. In addition, in the case of patterning with negative-type resist, nanopore patterns are formed by drawing the resist in line shape compared to the dot shape in positive-type resist, which enables to reduce the backscattering of the electron beam by applying smaller dose values. Figure 2.3.4 shows the SEM images of nanopore patterned substrate with 25 nm in pitch fabricated with the condition summarized in table 2.2.1: the dose value was set to 0.040 fC. The nanopores with 25 nm in pitch and 15 nm in diameter were fabricated over the patterned area. However, the bonding between neighboring nanopore was observed especially at the center of the patterned area [Fig. 2.3.4 (c)], which could be due to the larger scattering of the electron beam at the center part compared to the edge part of the patterns.

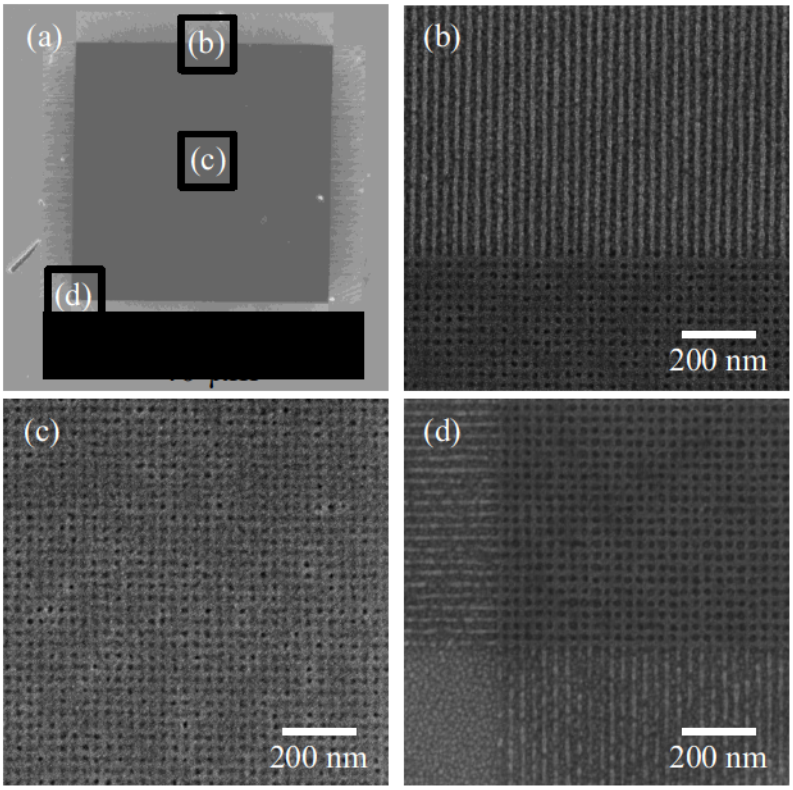

[redacted]

Fig. 2.3.4 SEM images of nanopore patterned substrate with 25 nm in pitch and 15 nm in diameter fabricated by applying negative-type resist (TEBN-1). The dose value was 0.040 fC.

In order to suppress the scattering of the electron beam at the center of the patterned area, dose values were optimized to gradually reduce the dose values towards the center part; the schematic image of this method and a typical SEM image of patterned substrate fabricated by this method are shown in Fig. 2.3.5. In this method, the dose values were reduced towards the center part at 8.0 μm intervals as described as (i-iii) in the schematic image of Fig. 2.3.5. Table 2.3.1 shows the lithography conditions with various dose values at (i-iii) position. The nanopore patterned substrates with 25 nm in pitch were fabricated with conditions summarized in table 2.3.1.

In order to investigate the uniformity of nanopores, patterned areas of (a), (b), and (c) described in the SEM image of Fig. 2.3.5 were observed by SEM; corresponding SEM images were shown in Fig. 2.3.6. In the case of condition A, the linewidth was broaden to reduce the diameter of the nanopore compared to the other lithography conditions, indicating the large scattering of the electron beam due to the higher dose values. By contrast, in condition C, linewidth was narrowed to form a bonding of neighbor nanopores due to the lower dose values. In the case of condition B and D, nanopores were uniformly fabricated with only a small part of the bonded nanopores. From these collective data, by optimizing the lithography processes, such as prebake conditions and dose values, fabrication of nanopore patterned substrate with Tbit/in2 areal density was successfully demonstrated.

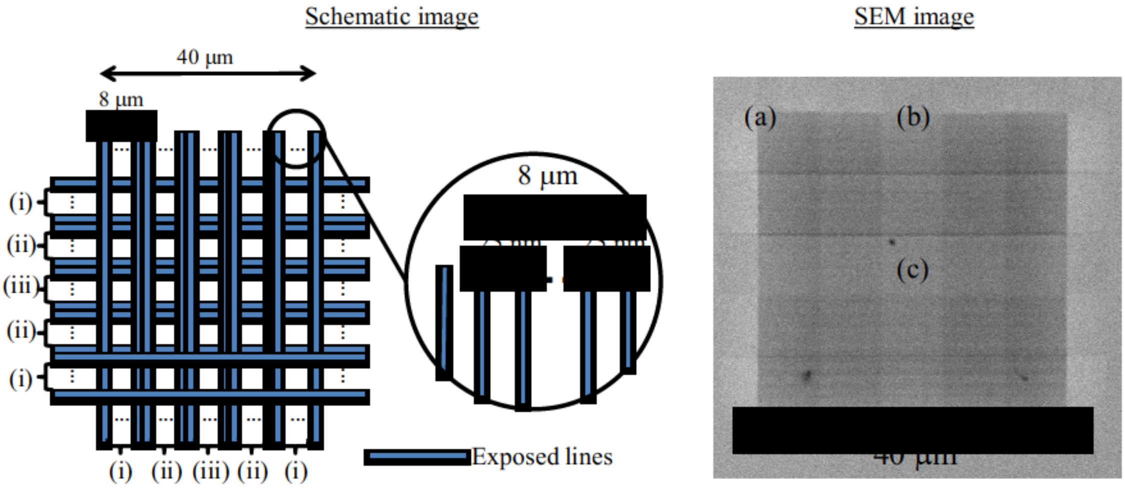

Fig. 2.3.5 Schematic image of nanopore fabrication and a typical SEM image of total patterned area.

Table 2.3.1 Dose values in each lithography condition

Condition	Dose value at each position / fC		
	(i)	(ii)	(iii)
A	0.032	0.028	0.024
B	0.030	0.028	0.026
C	0.030	0.026	0.022
D	0.028	0.026	0.024

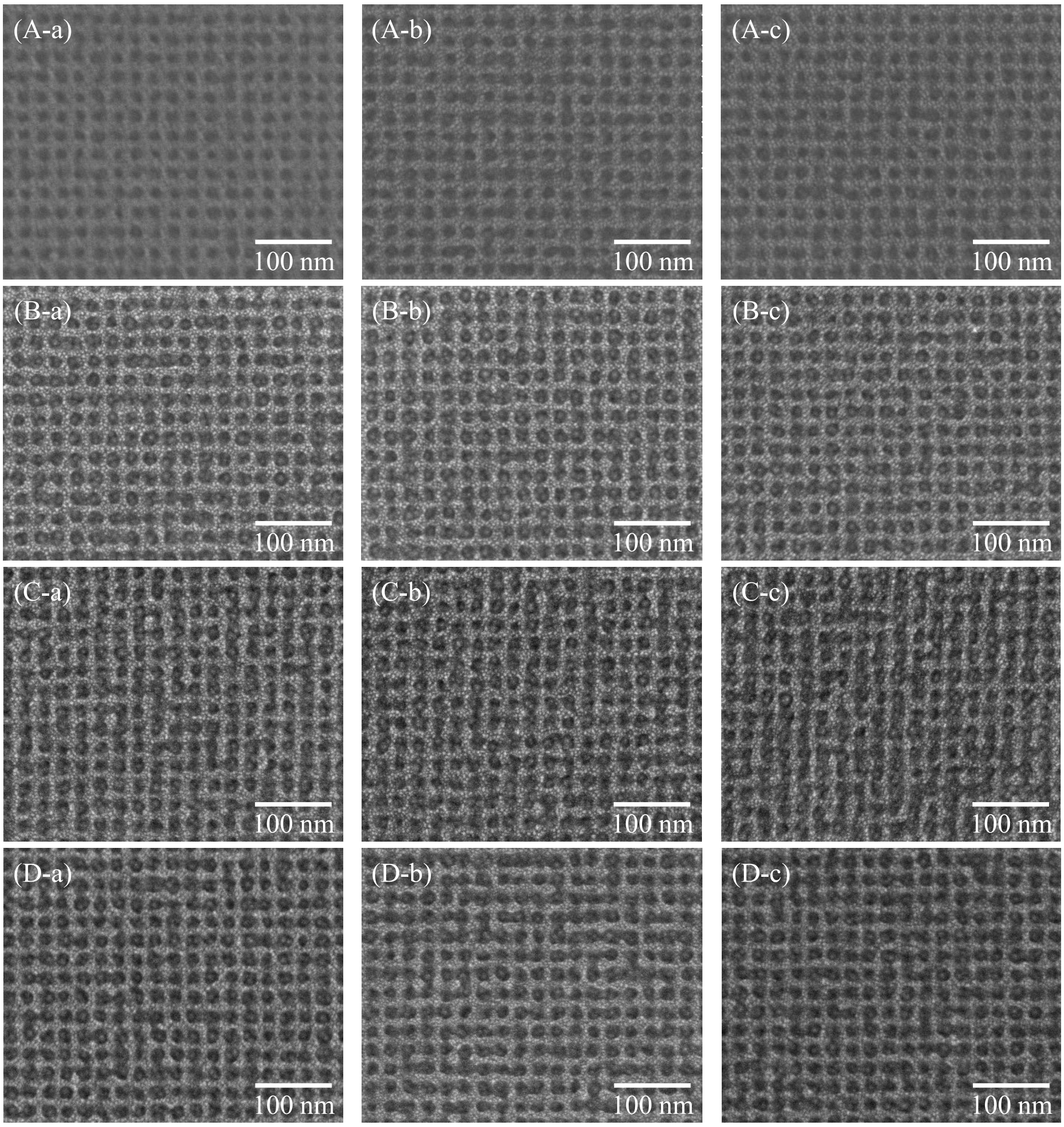

Fig. 2.3.6 SEM images of nanopore patterned substrate with 25 nm in pitch. Capital letters and small letters correspond to the lithography condition summarized in table 2.3.1 and patterned area described in Fig. 2.3.5, respectively.

2.4 Structural Control of Electrodeposited CoPt Nanodot Arrays with Tbit/in^2 Areal Density

2.4.1 Electrodeposition of CoPt Continuous Films with High Coercivity

Prior to the deposition of nanodot arrays, the surface morphology, crystal structure, and magnetic properties of the CoPt continuous films deposited with and without bath agitation were analyzed to optimize the deposition conditions of the nanodot arrays. Figure 2.4.1 shows the linear sweep voltammograms of CoPt electrolyte under different rotating speeds of 0, 50, and 200 rpm. In order to eliminate the effect of electrolyte composition, the concentration of the Pt electrolyte was fixed to 2.4 mM. From the voltammogram, the deposition of Pt and Co starts at a potential of about -0.45 V and -0.70 V (vs. Ag/AgCl), respectively, whereas hydrogen evolution reaction starts below -1.0 V vs. Ag/AgCl. As the rotating speed increased the current density increased for Pt and Co deposition, which is attributed to the enhancement of mass transfer of Pt and Co to the electrode surface to increase the current density. Based on this voltammogram, CoPt alloy was deposited at applied potential of -0.9 V (vs. Ag/AgCl), in which the composition of the CoPt alloy was easily controlled by varying the Pt electrolyte concentration.

Figure 2.4.2 shows the current-time transients during the CoPt electrodeposition with and without bath agitation under the same bath composition as Fig.2.4.1. After the current drop associated with the nucleation of the CoPt, the current density continuously decreased with deposition duration due to the slow diffusion of the metal ions to the electrode surface without agitation, indicating the diffusion limited growth of CoPt. On the other hand, the current density increased and plateaued in the case of bath agitation due to the enhancement of mass transport of the metal ions under forced convection caused by the rotating electrode, leading to the mitigation of diffusion limited growth of CoPt. These are typical effects of bath agitation during the deposition process, leading to an increase in the current density, which was also observed in Fig.2.4.1.

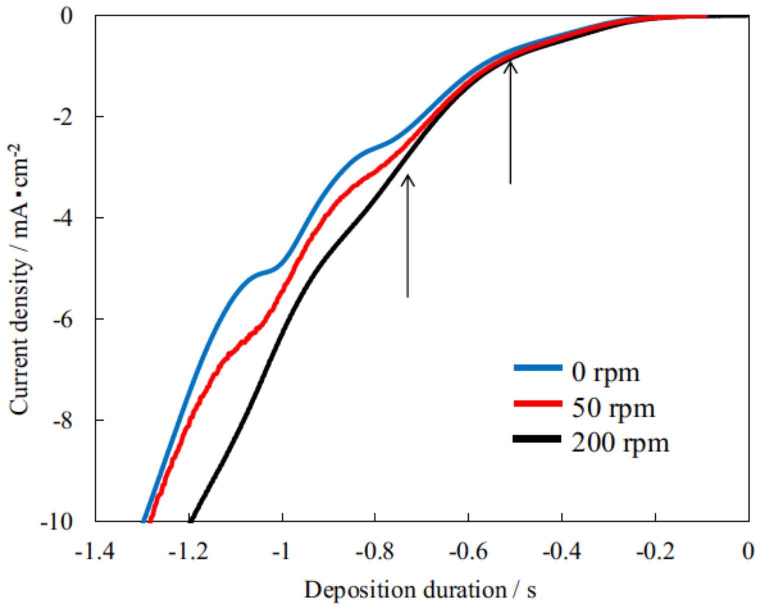

Fig. 2.4.1 Linear sweep voltammogram of CoPt electrolyte

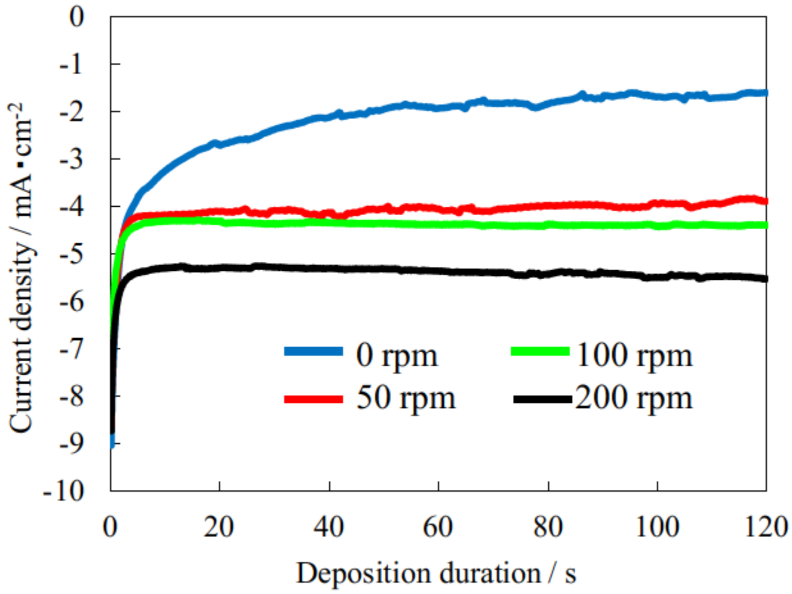

Fig. 2.4.2 Current-time transient during CoPt electrodeposition under agitation with different rotating speeds.

Figures 2.4.3 compares the surface morphology, observed by SEM, of the CoPt continuous films grown with a Pt electrolyte concentration of 2.4 mM, without and with bath agitation; the thicknesses of the films were ca. 30 nm for all deposition conditions. The surface morphology of the CoPt film without agitation showed that at the initial deposition stage, CoPt grew along with Ru to form a grain structure, followed by the growth of a net-like structure, which could be caused by the diffusion-limited condition at this potential similar to dendritic growth. On the other hand, net-like structure was vanished to form uniform and smooth grain structure under bath agitation, and the apparent grain size became much smaller and surface morphology became uniform, thus resulting in an isolated grain structure. As described in current-time transient, current density increased under bath agitation, indicating a higher number of CoPt nuclei, and therefore a smaller grain size and uniform surface morphology was achieved. It should be noted that the higher rotating speed could deteriorate the nanopore patterned substrate during the electrodeposition; indeed, a major deterioration of the substrate was confirmed by SEM observation over 100 rpm. Thus, the following analyses of the CoPt continuous films and the nanodot arrays were conducted under the rotating speed of 50 rpm, which was confirmed to be effective in controlling the diffusion of metal ions for the deposition of uniform films (Figs. 2.4.2 and 2.4.3).

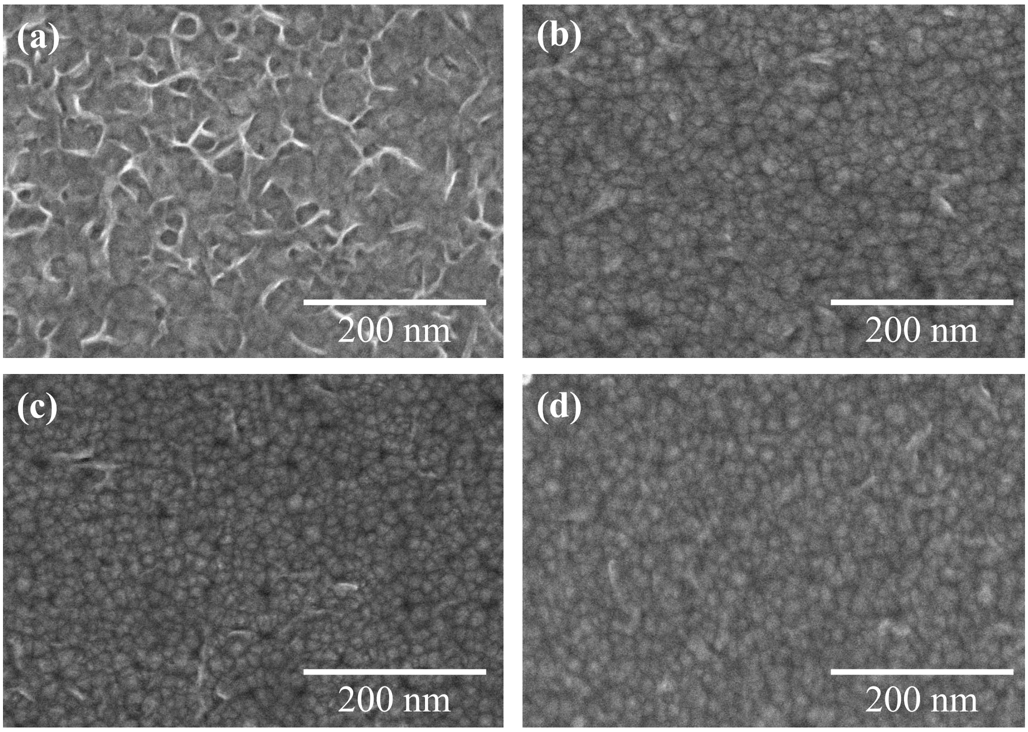

Fig. 2.4.3 SEM images of surface morphology of ca. 30 nm thick CoPt continuous films deposited without (a) and with bath agitation at (b) 50 rpm, (c) 100 rpm, and (d) 200 rpm. Pt electrolyte concentration was 2.4 mM.

To deposit CoPt continuous films with a composition of CoPt = 80:20, which should show high perpendicular coercivity, composition of CoPt was controlled with Pt electrolyte by changing the concentration from 1.2 mM to 3.0 mM. The composition of the as-deposited films were determined by ICP-MS analysis; the thickness of the films was ca. 40 nm. The alloy compositions of the deposited CoPt films with different Pt concentrations are plotted in Fig. 2.4.4. Because the concentration of the Pt electrolyte is two orders of magnitude lower than that of the Co electrolyte as shown in Table 2.2.2, the electrolyte agitation should strongly enhance the mass transport of the Pt ions to suppress the diffusion-limited condition, whereas diffusion of the Co ions is less influenced under agitation due to its high concentration. Therefore, the composition of Pt in the deposited film with agitation increased under the same concentration of Pt electrolyte. Nevertheless, 40 nm-thick CoPt films with a near-ideal composition of CoPt = 83:17 were achieved with Pt electrolyte concentrations of 1.6 and 3.0 mM for with and without bath agitation, respectively.

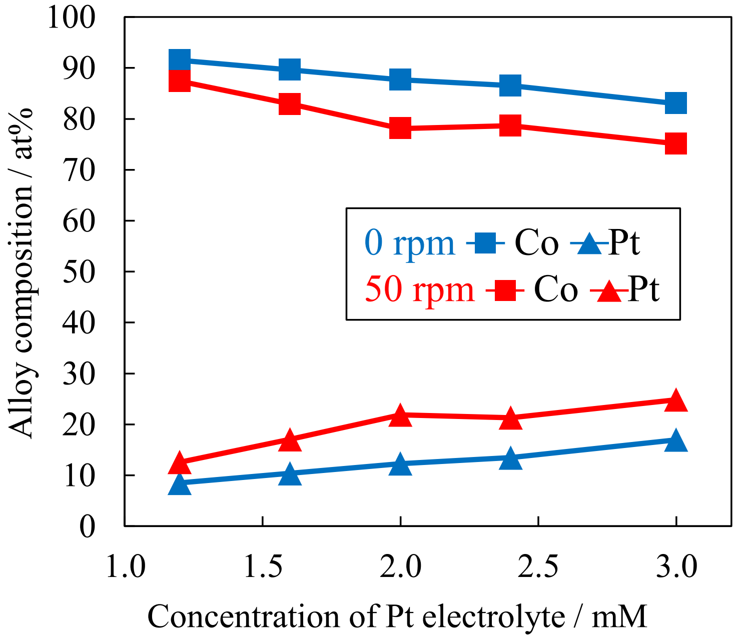

Fig. 2.4.4 Alloy composition of CoPt continuous films deposited with different concentration of Pt electrolyte

Table 2.4.1 shows the thickness-dependence of the alloy composition of CoPt films with different thicknesses measured by ICP-MS. Considering that Co and Pt are deposited from around -0.7 and -0.3 V (vs. Ag/AgCl), respectively, in the electrolyte used in this work, the diffusion layer is not stably formed at the initial deposition stage; thus the noble metal, Pt, is preferentially deposited compared to Co resulting in a slight increase in the Pt composition in both deposition conditions. In addition, when the electrolyte was not agitated, the Pt composition was higher than that of the film deposited with electrolyte agitation at its initial deposition stage (thickness of 1 and 2 nm, respectively), thus confirming the large composition gradient with thickness. When the composition gradient of the film is large, the film should contain several crystal structures, especially the near-equiatomic composition of CoPt as observed at the initial deposition stage should exhibit fcc structure phase. On the other hand, the composition rarely differed from each deposition stage and the alloy composition was closer to the ideal composition of Co:Pt = 80:20 from its initial deposition stage under agitation, indicating that CoPt is likely to grow as an hcp structure from its initial deposition stage. This uniform composition is attributed to the formation of the diffusion layer with constant thickness under forced convection.

Table 2.4.1 Thickness-dependence of alloy composition of CoPt continuous films

Rotating speed / rpm	Pt electrolyte / mM	Thickness / nm	Alloy composition Co/ at%	Pt/ at%
0	3.0	1	59	41
0	3.0	8	75	25
0	3.0	21	78	22
50	1.6	2	64	36
50	1.6	8	71	29
50	1.6	20	72	28

To investigate the crystal structure of the deposited CoPt films, XRD patterns of the Ru substrate and ca. 40 nm-thick CoPt films deposited with and without bath agitation were measured; corresponding data are shown in Fig. 2.6. The Ru substrate showed two peaks corresponding to hcp (002) and hcp (101) at 42.3° and 44.2°, respectively, which were also observed in the diffraction patterns of the deposited CoPt films. All of the deposited films showed a diffraction peak of hcp (002) at 43-44°, indicating that CoPt grew in a perpendicular direction from the Ru substrate due to the small lattice mismatch between hcp Ru and hcp CoPt, which induces epitaxial-like growth. In addition, peak of hcp (002) shifted to negative value as the composition of Pt increased, which has large atomic radius compared to Co, increased, leading to the broadening of the lattice spacing of CoPt.

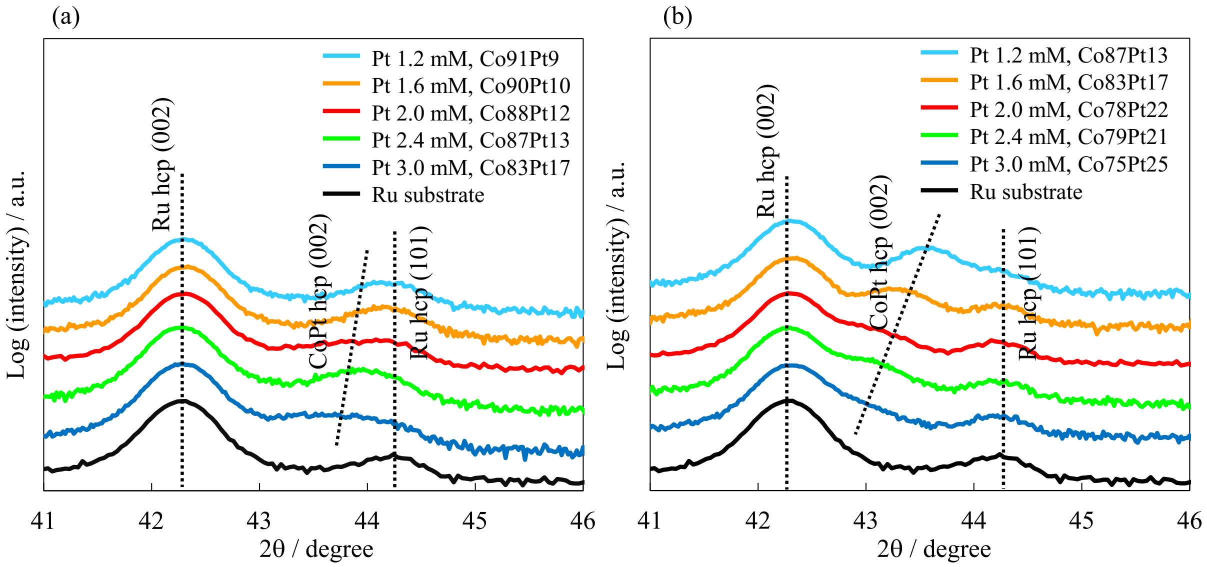

Fig. 2.4.5 XRD patterns of CoPt continuous films deposited
(a) without and (b) with bath agitation

Figure 2.4.6 compares the XRD patterns of CoPt films with a near-ideal composition of CoPt = 83:17 deposited with and without agitation. From the XRD patterns, the shape of the (002) peaks were different with and without bath agitation; the deposited film without agitation showed a broad (002) peak at 43.8°, whereas sharp (002) peak was observed at 43.2° with agitation. Table 2.5 summarizes the 2θ and logarithmic intensity of the hcp (002) diffraction peak of CoPt. When the electrolyte was agitated, the logarithmic intensity increased from 2.9 to 4.0, indicating that a highly oriented CoPt in the (002) direction was formed with electrolyte agitation. This increase in the crystallinity is due to the formation of a film with a uniform composition as observed in the composition analysis (Table 2.4) to have hcp structure from the initial deposition stages, whereas large composition gradient leads to the formation of partial fcc phases in the deposited films that decrease the crystallinity of hcp (002) structure without bath agitation.

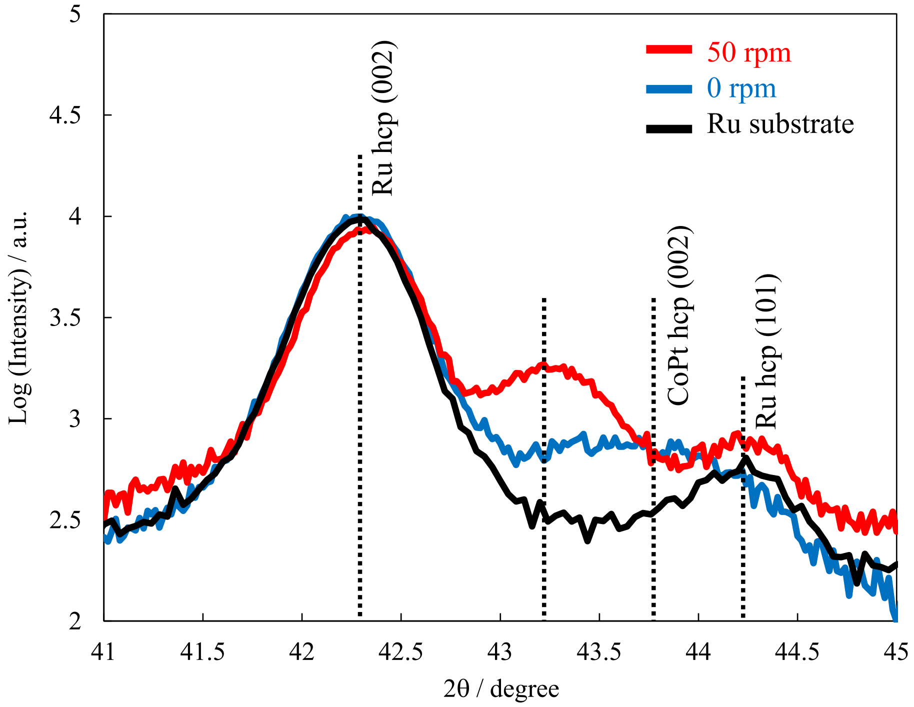

Fig. 2.4.6 XRD patterns of Ru substrate and CoPt contrinuous films deposited with and without agitation.

Table 2.4.2 2θ and peak intensity of hcp (002) of CoPt continuous films

Rotating speed	Alloy composition		CoPt-hcp(002)	
/ rpm	Co/ at%	Pt/ at%	2θ / °	log(intensity) / -
0	83	17	43.8	2.9
50	83	17	43.2	4.0

In addition, lattice mismatch between Ru underlayer and CoPt was investigated by calculating the a-axis of deposited CoPt films from hcp (002) peak. The lattice spacing d, which corresponds to the c-axis lattice parameter for (002) peak, was calculated from Bragg equation, where n is an integer and λ is the wavelength of the incident wave (1.5418 Å for CuKα). By using the calculated values of c-axis parameter, a-axis parameter was calculated based on the ratio of a- and c-axis of CoPt ($c = 1.63a$).

$$d = \frac{n\lambda}{2\sin\theta} \tag{2.3.1}$$

The calculated values of c- and a-axis lattice parameters of the deposited films and theoretical values of these parameters of Ru and $Co_{80}Pt_{20}$ are summarized in Table 2.5. The calculated c- and a-axis parameters of the film deposited with bath agitation were in good agreement with the theoretical values of $Co_{80}Pt_{20}$, whereas the calculated values of the film deposited without agitation were not. This equivalence in the calculated values and theoretical values also provide evidence for the improvement of the crystallinity of the hcp structure under agitation compared to without agitation. In addition, lattice mismatch of a-axis parameter between Ru and deposited CoPt films were calculated to be 5.73 and 4.48 % for without and with agitation, which indicates that CoPt is more likely to grow along with Ru crystal under agitation.

Table 2.4.3 Lattice parameters of electrodeposited film

Material		lattice parameters / nm	
		c-axis	a-axis
Theoretical values	Ru	0.427	0.269
	$Co_{80}Pt_{20}$	0.419	0.257
Electrodeposited films	0 rpm	0.413	0.254
	50 rpm	0.419	0.257

These features of high crystallinity of hcp structure and epitaxial-like growth observed in the structure analyses of the CoPt film deposited under agitation should improve the perpendicular magnetic anisotropy of CoPt. Figure 2.7 shows the out-of-plane magnetic hysteresis loops for the same samples as shown in Fig. 2.6, which were measured by polar magneto-optical Kerr effect equipment. The measured coercivity and squareness are summarized in Table 2.6. The film deposited without agitation exhibited a perpendicular coercivity of 1.0 kOe and squareness of 0.35. By contrast, the film deposited with agitation increased its coercivity and squareness up to 4.3 kOe and 0.65, respectively. This increase in coercivity and squareness is attributed to the increase in crystallinity of the hcp (002) plane as observed in the XRD pattern (Fig. 2.5), which induces the perpendicular magnetic anisotropy of

CoPt from the initial deposition stage. Furthermore, the isolated grain structure [Fig. 2.3 (c)] could cause the decoupling of the magnetic grains at grain boundaries to increase the coercivity.

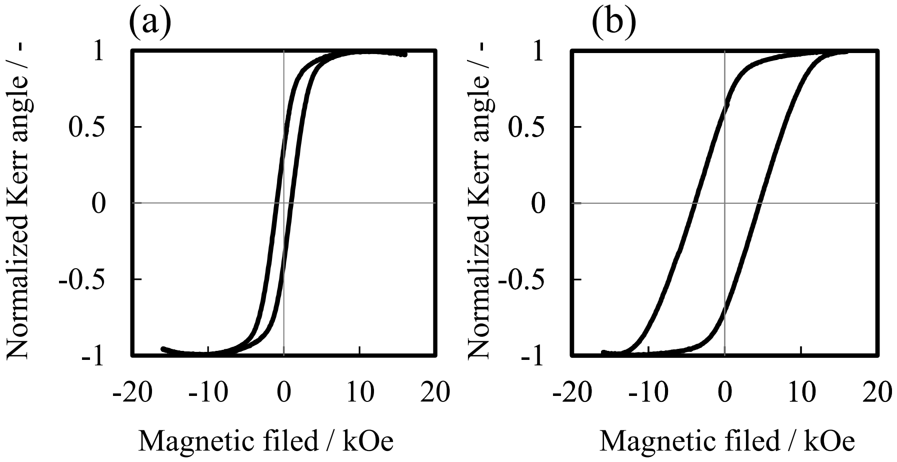

Fig. 2.4.7 Out-of-plane hysteresis loops of CoPt continuous films deposited without (a) and with (b) agitation.

Table 2.4.4 Coercivity and squareness of CoPt continuous films

Rotating speed / rpm	Alloy composition		Coercivity / kOe	Squareness
	Co/ at%	Pt/ at%		
0	83	17	1.0	0.35
50	83	17	4.3	0.65

These results successfully demonstrated the improvement of coercivity of CoPt by controlling the diffusion state of metal ions from the initial deposition stage with bath agitation, which should reflect in the formation of CoPt nanodot arrays with Tbit/in^2 areal density.

2.4.2 Characterization of CoPt Nanodot Arrays with Tbit/in^2 Areal Density

From the characterization of the CoPt continuous films, significant improvement in the crystallinity of CoPt was found by controlling the diffusion state of metal ions from the initial deposition stage. Thus in order to achieve high coercivity of CoPt nanodot arrays with Tbit/in^2 areal density, fabrication of nanodot arrays was attempted under forced convection conditions based on the results of chapter 2.4.1.

Figure 2.4.8 shows representative SEM images of CoPt nanodot arrays deposited inside the nanopore patterned substrate with 100 nm in pitch and 10 nm in diameter with and without the treatment by excimert-UV irradiation. As these images were taken after removal of the entire EB resist, the Ru surface appeared as dark contrast and the CoPt nuclei appeared as bright contrast. As seen in Fig. 2.4.8, the effects of excimer-UV irradiation were clear; without excimer-UV treatment, CoPt nucleated at only a fraction of patterned area, resulting in the formation of nanodot arrays with insufficient uniformity over the patterned area. In contrast, when the nanopore patterned substrates were treated with excimer-UV before the electrodeposition, CoPt nucleated uniformly on the entire patterned area. It was hypothesized that, after the development process, small amount of residue remained inside the nanopore, hindering the nucleation of CoPt to form non-uniform nanodot arrays. This residue is a critical problem, especially for the smaller nanopore of less than 10 nm diameter, thus, excimer-UV treatment should be considered as an essential process for the fabrication of ultra-high density nanodot arrays.

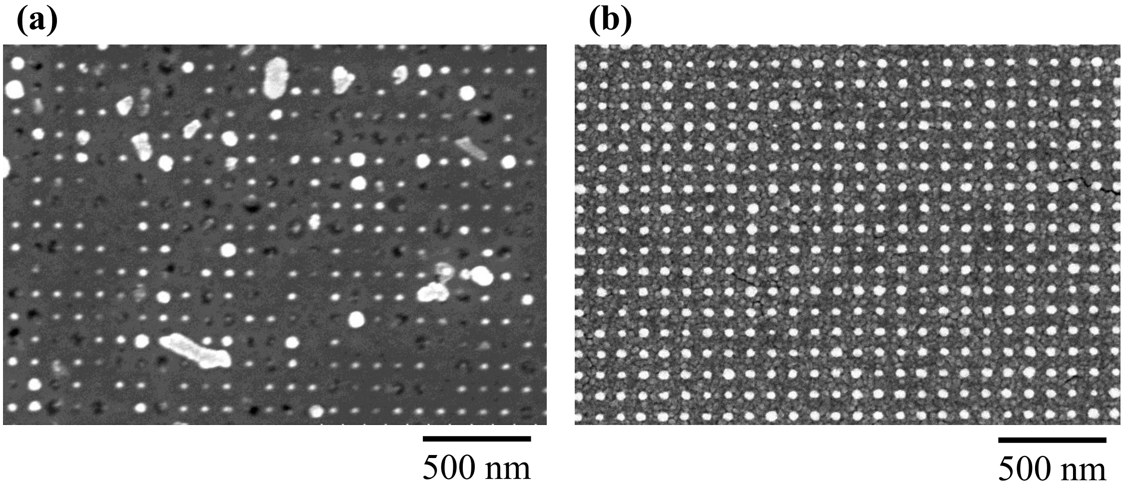

Fig. 2.4.8 SEM images of CoPt nanodot arrays treated (a) without and (b) with excimer-UV irradiation before the electrodeposition.

Figures 2.4.9 (a) and (b) show SEM images of CoPt nanodot arrays with 35 nm in pitch deposited with and without bath agitation, respectively; both nanodot arrays showed near-ideal composition of Co :Pt = 80 :20, which were measured by ICP-MS. From the top images, although the diameter of CoPt around 15–20 nm was larger than the nanopore diameter due to the overfilling of CoPt from the nanopore patterns, nanodot arrays were uniformly fabricated over the patterned area in both deposition conditions. Fabrication of the CoPt nanodot arrays with 25 nm in pitch, which corresponds to a recording density of 1 Tbit/in^2, was also successfully demonstrated under agitation as shown in Fig. 2.4.9 (c). However, in such ultra-high recording density, it is difficult to obtain uniform nanopores over the patterned area owing to the difficulties in controlling the electron beam dispersion. Therefore, in this chapter, analyses were conducted for nanodot arrays having 35 nm in pitch. The characterization of continuous films showed that the crystallinity of CoPt was improved from the initial deposition stage when agitation was applied, thus to investigate the difference in crystal growth behavior of CoPt inside nanopore patterns, the lattice structure of the CoPt nanodot arrays with 35 nm in pitch were observed using TEM.

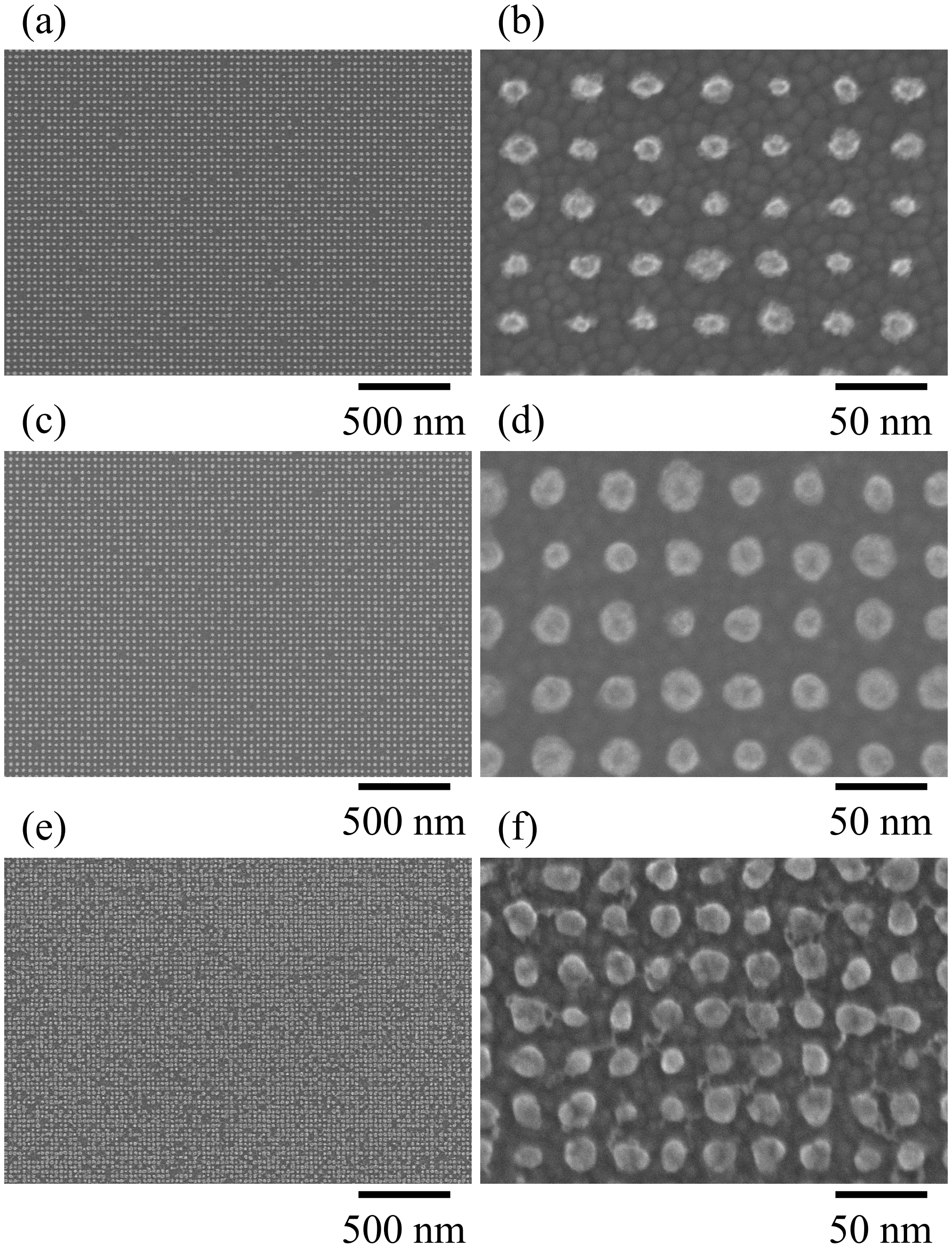

Fig. 2.4.9 High and low magnification SEM images of CoPt nanoto arrays with 35 nm in pitch deposited (a, b) without and (c, d) with agitation, and (e, f) nanodot arrays with 25 nm in pitch deposited with agitation.

Figure 2.4.10 shows the cross-sectional TEM images of the CoPt nanodot arrays deposited with and without bath agitation, which are the same samples as shown in the Fig.

2.4.9 SEM images. Figures 2.4.10 (a) and (b) show the cross-sectional images of a single nanodot, and insets show the selected area electron diffraction (SAED) patterns of each nanodot. Lower magnification TEM images confirmed the formation of a uniform columnar nanodot without any voids. In addition, the overfilling of CoPt from the nanopore was observed as described above. In both deposition conditions, the SAED showed ring-like patterns indicating that the deposited nanodots are polycrystalline owing to the multi-nucleation inside the nanopore at this applied potential. Figures 2.4.10 (c) and (e) show higher magnification TEM images of the interface between CoPt and the Ru underlayer. The lattice spacing measured in the TEM image was 0.2 nm, which agrees with the d_{002} plane spacing of the hcp CoPt (0.209 nm) [26]. At the initial deposition stage, the lattice fringes of CoPt were aligned along with the Ru crystal in a direction perpendicular to the interface in both deposition conditions, indicating the epitaxy relationship between CoPt and Ru, which is significant to induce the perpendicular magnetic anisotropy of the nanodot arrays. Figures 2.4.10 (d) and (f) show high magnification TEM images of the upper part of the nanodot. As the growth of CoPt proceeds, the crystal lattice of CoPt is oriented in several directions when agitation was not applied, whereas the crystal lattice of hcp (002) remained in a perpendicular direction and was uniformly oriented from the initial deposition stage under bath agitation. This uniform orientation could be due to the homogenization of the CoPt alloy composition from the initial deposition stage, which corresponds to the results analyzed in the continuous CoPt films. In addition, diffusion-limited growth of CoPt was considered to be mitigated based on the analyses of continuous films under electrolyte agitation, which could reduce the formation of randomly oriented nuclei to improve the crystal orientation of the nanodots.

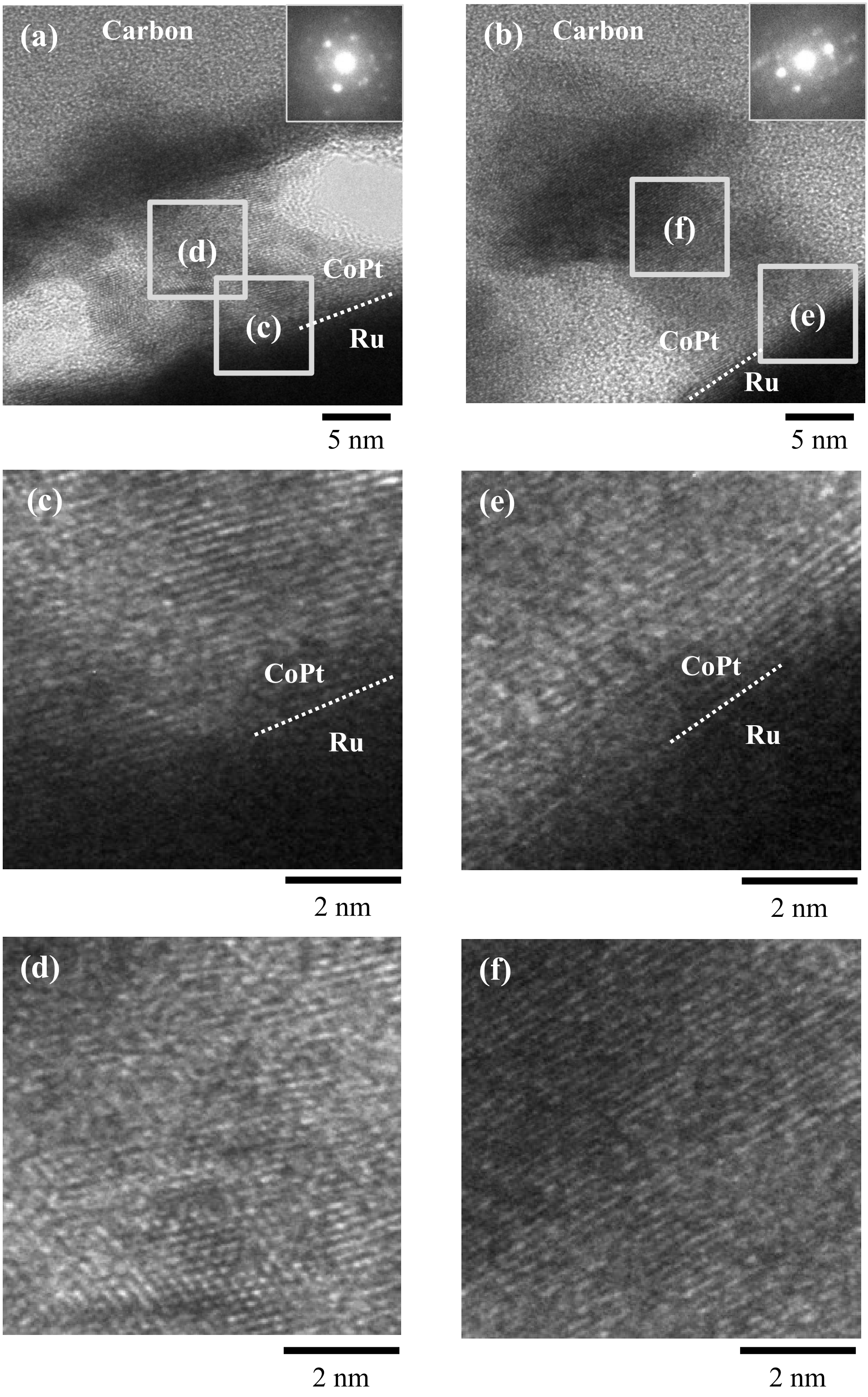

Fig. 2.4.10 Cross-sectional TEM images of CoPt nanodot arrays with 35 nm in pitch deposited (a) without and (b) with agitation. High magnification images (c, e) at interface of CoPt and Ru substrate and (d, f) upper part of CoPt nanodot arrays. The insets show the SAED images.

Based on these observations of the TEM images, it was found that nanodot arrays with uniform crystal orientations in the perpendicular direction formed under electrolyte agitation, which should improve the perpendicular magnetic anisotropy of CoPt. Hence, magnetic characterization of the nanodot arrays with 35 and 25 nm in pitch was attempted using polar magneto-optical Kerr effect equipment; corresponding hysteresis loops, measured coercivity, and squareness are shown in Fig. 2.4.11 and Table 2.4.5, respectively. The coercivity and squareness of the nanodot arrays deposited without electrolyte agitation were 2.0 kOe and 0.64, whereas the nanodot arrays deposited with agitation exhibit higher coercivity and squareness values of 4.0 kOe and 0.87. This increase in coercivity and squareness corresponds with the improvement in the crystal orientation as confirmed by the TEM analysis, which induces the perpendicular magnetic anisotropy of CoPt. In addition, the columnar shape of the nanodot arrays induces shape magnetic anisotropy along the growth direction to enhance the perpendicular coercivity and squareness, also physical isolation of nanodots enhances the exchange decoupling of each nanodot, thus resulting in higher magnetic properties compared to continuous films. In the case of nanodot arrays with 25 nm in pitch, the low coercivity is due to the small patterned area of 40 μm^2, because the laser spot of magneto-optical Kerr effect device is 100 μm in diameter, it was difficult to detect the magnetic properties of nanodot arrays. Although the coercivity of nanodot arrays with 25 nm in pitch was lowered we have succeeded to fabricate CoPt nanodot arrays with 1 $Tbit/in^2$, exhibiting ferromagnetic properties. For the BPM application, it is significant to estimate not only the coercivity but also the magnetic anisotropy, K_u, of nanodot arrays. Since the diameter of the CoPt nanodot arrays is less than 20 nm, they should exhibit single magnetic domain structure [6]. Thus, the coercivity, H_c, can be calculated from the equation of $H_c=H_A=2K_u/M_s$, where H_A and M_s are anisotropy field and saturation magnetization, respectively, based on the Stoner-Wohlfarth model. In this model, the maximum value of coercivity is equal to H_A of CoPt (28 kOe) [7], however, measured coerivity showed smaller coercivity (4.0 kOe). The decrease in the coercivity is attributed to the small size of CoPt nanodot arrays, because the critical single domain size of CoPt is 0.89 μm, coercivity decreases below this critical size. In addition, in the case of CoPt nanodot arrays, magnetostatic interaction between adjasent nanodots decreases the coercivity. Sun et al. reported that the magnetostatic interaction affects the coercivity and remanence of Fe_3Pt nanowire arrays with diameter of 10 nm and interwire distance of 40 nm [8]. Upon decreasing the interwire distance, coercivity and remanence were decreased, indicating the magnetostatic interaction between each nanowire. Considering this point, in the case of CoPt nanodot arrays, magnetostatic interaction should occur since the pitch between each nanodot is 35 nm. In order to further investigate the magnetic anisotropy of nanodot arrays, M_s should be precisely measured with superconducting quantum interference devices or vibrating sample magnetometer by expanding the fabricated area of CoPt nanodot arrays with the application of patterned substrate fabricated by such as nanoimprint lithography technique in the next step.

From the above collective results, by controlling the composition and crystal orientation of CoPt with bath agitation, deposition uniformity and magnetic properties, such as coercivity and squareness, of the ultra-fine CoPt nanodot arrays with Tbit-level areal density was successfully controlled. Considering the formation of the overfilling parts of the nanodot arrays, which have polycrystalline structures with random crystal orientations owing to the rapid nucleation that may be due to the formation of hemispherical diffusion of metal ions to expand the nucleation sites, future study may achieve higher coercivity and squareness by suppressing the overfilling of CoPt.

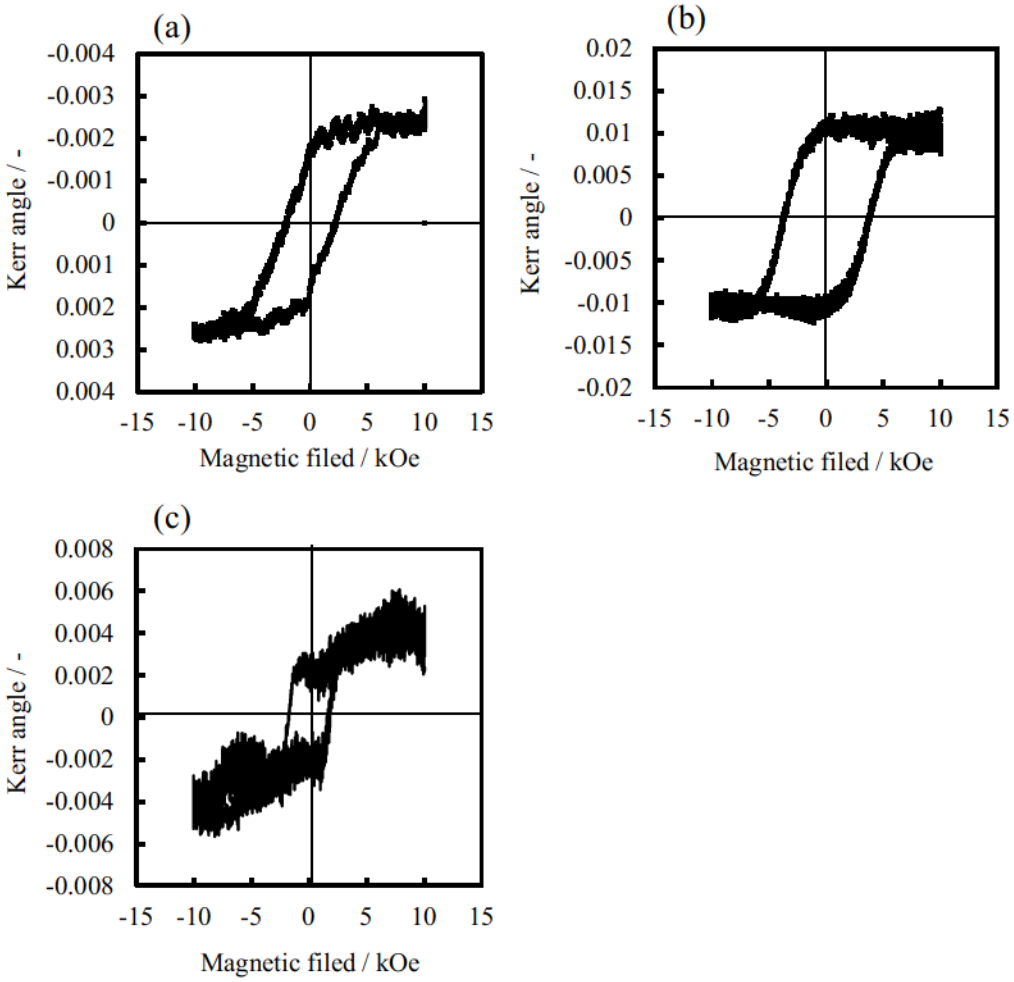

Fig. 2.4.11 Out-of-plane hysteresis loops of CoPt nanodot arrays with 35 nm in pitch deposited without (a) and with (b) agitation. (c) CoPt nanodot arrays with 25 nm in pitch deposited with agitation

Table 2.4.5 Coercivity and squareness of CoPt nanodot arrays

Pitch / nm	Rotating speed / rpm	Coercivity / kOe	Squareness
35	0	2.0	0.64
35	50	4.0	0.87
25	50	1.8	-

Conclusion

In chapter 2, the composition and crystal orientation of CoPt was controlled by controlling the diffusion of metal ions under bath agitation to achieve precise fabrication of CoPt nanodot arrays with high and uniform coercivity. Prior to the fabrication of nanodot arrays, uniform nanopore patterned substrate with 25 nm in pitch were successfully demonstrated by detailed optimization of electron beam lithography conditions, such as prebake temperature and dose values. For the fabrication of nanodot arrays, composition of CoPt was controlled from its initial deposition stage to improve the crystallinity of the hcp (002) structure of CoPt by applying bath agitation with rotating electrode. Cross-sectional TEM images of the CoPt nanodot arrays deposited with bath agitation confirmed that stacking of the hcp (002) lattice was uniformly oriented in a perpendicular direction from the Ru interface to the upper part of the nanodot, thus enhancing the coercivity and squareness from 2.0 kOe and 0.64 to 4.0 kOe and 0.87, respectively. The collective results have successfully demonstrated the facrication of Tbit-level ferromagnetic nanodot arrays with high coercivity by controlling the crystal structure at nanoscale. To the best of my knowledge, this is the first research that demonstrate the fabrication of nanodot arrays that exhibit sufficient high coercivity by electrochemical process, which is applicable to BPM.

References

[1] S. N. Piramanyagam, and K. Srinivasan, *J. Magn. Magn. Mater.*, 321 (2009) 485.

[2] G. Pattanaik, J. Weston, G. Zangari, *J. Appl. Phys.*, 99 (2006) 08E901.

[3] X. Xu, M. Ghidini, and G. Zangari, *J. Electrochem. Soc.*, 159 (2012) D240.

[4] ZEON corporation Electronics Materials Division, October 2010, "ZEP520A Techinical Report", available: https://www.zeonchemicals.com/pdfs/ZEP520A.pdf, [Accessed 13 November 2016].

[5] B. Bilenberg, M. Schøler, P. Shi, M. S. Schmidt, P. Bøggild, M. Fink, C. Schuster, F. Reuther, C. Gruetzner, and A. Kristensen, *J. Vac. Sci. Technol. B*, 24 (2006) 1776.

[6] K. Mitsuzuka, N. Kikuchi, T. Shimatsu, O. Kitamoto, H. Aoi, H. Muraoka, and J. C. Lodder, *IEEE Trans. Magn.*, 43 (2007) 2160.

[7] D. Weller, A. Moser, L. Folks, M. E. Best, W. Lee, M. F. Toney, M. Schwickert, J-U. Thiele, and M. F. Doerner, *IEEE Trans. Magn.*, 36 (2000) 10.

[8] D-L. Sun, J-H. Gao, X-Q. Zhang, Q-F. Zhan, W. He, Y. Sun, and Z-H. Cheng, *J. Magn. Magn. Mater.*, 321 (2009) 2732.

Chapter 3

Analysis of Nucleation Process of CoPt inside Ultrafine Nanopore

3.1 Introduction

In order to achieve high SNR and high coercivity of BPM with Tbit-level recording density, fabrication of highly uniform nanodot arrays is essential, because defects, grain boundaries, and random crystal orientation cause the non-uniformity in coercivity in each nanodot, leading to the media noise to degrade the recording performance [1, 2]. Therefore, a single magnetic domain structure is highly desirable for BPM application owing to its low media noise and high coercivity, and thus it is essential to miniaturize the size of nanodot arrays while avoiding the superparamagnetic limit. When each nanodot consists of single crystal structure, it can be considered as an ideal structure to exhibit high and uniform coercivity because it has high crystal orientation without the formation of grain boundaries, which is highly desirable for the application in BPM. In chapter 2, although the crystal structure was successfully controlled by controlling the diffusion of metal ions, fabricated nanodot arrays showed polysrystalline structure with random grain bounraeis.

At ultra-high recording densities, the nanodots are miniaturized to 10 nm in diameter. Therefore, to control the magnetic properties and deposition uniformity, especially to achieve fabrication of nanodot arrays consists of single crystal structure, it is essential to understand the mechanism of the initial deposition stages of ferromagnetic metal inside the nanopore. Electrochemical nucleation and growth process have been studied for several decades by theoretical and experimental methods, and several theoretical models of formation mechanisms have been proposed [3-6]. Recently, with the development of technologies for in situ characterization, such as transmission electron microscope (TEM) [7-9] and atomic force microscope (AFM) [10-12], reports on the quantitative analyses of nucleation mechanisms based on the in situ imaging have been increasing. In addition, in the fields of electrochemical microfabrication, such as through-silicon via process, formation mechanisms of metals inside the micro-ordered pattern have been extensively studied [13-15]. However, above mentioned reports analyzed the nucleation mechanisms on the planer substrate or inside the micro-ordered patterns, there has been no reports of analyses on the nucleation and growth process inside the ultra-fine nanopores with 10 nm diameter, which is required in BPM application.

Thus, in this chapter, the initial nucleation and growth processes of CoPt inside the nanopores were analyzed under various conditions, such as different applied potentials and sizes of nanopores, to achieve precise control of the deposition for the fabrication of nanodot arrays consists of single crystal structure.

3.2 Experimental

3.2.1 Characterization of Initial Deposition Stages of CoPt

(002) oriented Ru (60 nm) and Ti (5 nm) as an adhesion layer were sputter deposited onto an n-type Si (100) substrate. Electron beam lithography was carried out to fabricate nanopore patterned substrate by using an EBL apparatus (ELS-7500, ELIONIX). The EBL conditions are summarized in Table 3.2.1. Prior to the CoPt electrodeposition, the substrate was exposed to excimer UV irradiation for 30 s to remove the residue at the bottom of the nanopores.

An electrolyte containing $Pt(NH_3)_2(NO_2)_2$ and 100 mmol L^{-1} of $CoSO_4$, $(NH_4)_2C_6H_6O_7$, and NH_2CH_2COOH was used. The concentration of $Pt(NH_3)_2(NO_2)_2$ was adjusted for each deposition condition to maintain the film composition (Co:Pt = 80:20). The bath temperature was 303 K, and the bath pH was adjusted to 5.2 by adding NaOH. Electrodeposition of CoPt was performed under a constant applied potential using a potentiostat (HZ-0.50, Hokuto Denko) with a three-electrode system consisting of Co wire as the counter electrode and a Ag/AgCl electrode as the reference electrode.

Magnetic characterization of the deposited films was carried out with polar magneto-optical Kerr effect equipment (BH-810CPC-WU, NEOARK). X-ray diffraction (XRD) patterns of the deposited films were collected using an X-ray diffractometer (Rint-TTR, Rigaku) using Cu-K α radiation (λ = 1.54184 Å). Morphological and structural characterizations of the electrodeposited CoPt nanodot arrays were performed using a high resolution scanning electron microscopy (HR-SEM, S5500, Hitachi High-Tech.) and transmission electron microscope (TEM, JEM-2010, JEOL) after removing the entire EB resist by exposure to excimer UV irradiation for 2.0 min and rinsing with ethanol and UPW.

Table 3.2.1 Operating conditions of electron beam lithography

Resist	ZEP520A-7 : ZEP-A = 1:2
Spin coat rate	5000 rpm, 60 s
Prebake	180 °C, 3 min
Thickness of resist	30 nm
Accelerating voltage	50 kV
Beam current	20, 100 pA
Dose value	3.0-10 fC / dot
Developer	IPA
Developing time	5 s
Developing temperature	5 °C
Rinse	UPW

3.2.2 Analysis of Distribution of CoPt Nuclei inside Nanopores

Nanopore patterned substrate was fabricated on (002) oriented Ru substrate with the conditions summarized in Table 3.2.1. In order to achieve uniform distribution of CoPt nuclei on the Ru substrate, Ru surface was planarized by chemical mechanical polishing (CMP). In the case of 60 nm-thick Ru substrate because the grain size of Ru is around 20 nm, grain boundaries are formed at the surface. Thus, in order to distinguish the nucleation of CoPt from the surface conditions, such as grain boundary, 1.5 μm-thick Ru was sputtered to increase the grain size so as to reduce grain boundaries on the surface. Table 3.2.2 shows the CMP conditions. CoPt was electrodeposited potentiostatically on nanopore patterned Ru substrate in the same electrolyte and electrochemical system as described in chapter 3.2.1. In order to eliminate the effect of concentration of metal ions, $Pt(NH_3)_2(NO_2)_2$ was set to 2.1 mmol L^{-1}. The CoPt nuclei deposited inside the nanopores were recorded using HR-SEM (S5500, Hitachi High-Tech.). The distribution of CoPt nuclei were quantitatively measured by analyzing the recorded SEM images using the computer software, ImageJ.

Table 3.2.2 CMP conditions

Abrasive	Glanzox 3900 : H_2O = 1 : 5
Drop volume of slurry	3 mL/min
Pressure	1810 Pa
Rotational rate of pat	80 rpm
Rotational rate of head	45 rpm
Planarlize time	10 min

3.3 Analysis and Control of the Initial Electrodeposition Stages of CoPt Nanodot Arrays

3.3.1 Characterization of Inidial Deposition Stages of CoPt

In order to analyze the initial deposition stages of CoPt inside the ultra-fine nanopores, the CoPt nucleation and growth processes were observed by SEM. The concentration of Pt electrolyte was set to 0.6 mM in all deposition conditions to eliminate the effect of electrolyte concentration on the initial deposition stages. Prior to CoPt electrodeposition, nanopore patterned substrates with 65, 50, 35, 25, 15, and 10 nm in diameter and 100 nm in pitch were fabricated by EBL. CoPt was then deposited on the nanopore patterned substrate with an applied potential of -0.9 V (vs. Ag/AgCl), which is the same condition as used in chapter 2. Figure 3.3.1 shows SEM images of deposited CoPt nuclei inside the nanopores with different diameters. The deposition duration was set to 3.0 s, which is appropriate for depositing CoPt as nuclei to obtain clear images by SEM. At this deposition stage, CoPt nucleated as fine grains of 2.0–3.0 nm in diameter and randomly distributed on the Ru surface at the bottom of the nanopores. It should be noted that CoPt nucleated from the outer side of the nanopore due to the current crowding effect at the edge of photoresist patterns [16, 17]. The current crowding occurs at the edge of the patterns because of the higher degree of mass flux and local current density due to the higher supply of metal ions from the three dimensional directions, thus current density is expected to be higher at the outer side compared to inner side [16, 17]. In larger nanopores, a distinct difference in the current density led to CoPt nucleation from the outer side of the nanopore. On the other hand, in the smaller nanopore with a 10 nm diameter, nucleation of CoPt is much less likely to be affected by the difference in current density. Although the number of nuclei decreased in the smaller nanopores multiple nucleation occurred even with the smallest nanopore of 10 nm [Fig.3.3.1 (a)].

Figure 3.3.2 shows SEM images of the growth ptocess of CoPt into 10 nm nanopore deposited at -0.9 V (vs. Ag/AgCl). The duration times were 2.0, 3.0, and 5.0 s. As several nuclei of 2.0–3.0 nm in size were distributed on the bottom surface at an early stage, they grew as a cluster with several grain boundaries. This random and multinucleation could result in a lack of uniformity in the coercivity of each CoPt dot.

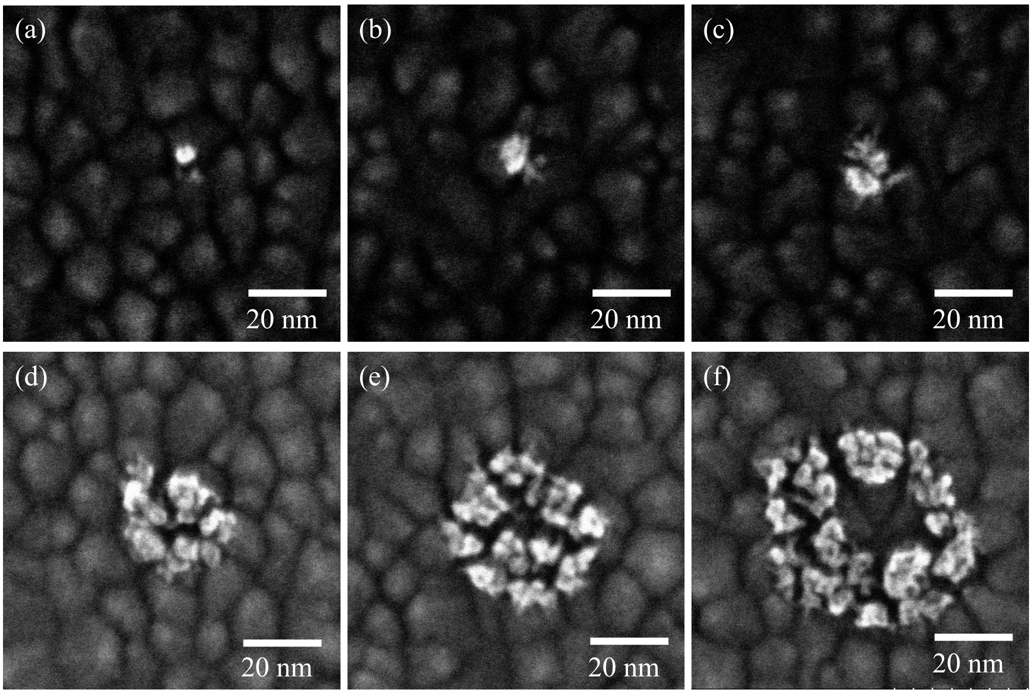

Fig. 3.3.1 SEM images of CoPt deposited with -0.9 V (vs. Ag/AgCl) for 3.0 s in nanopores with different diameters: (a) 10 nm, (b) 15 nm, (c) 25 nm, (d) 35 nm, (e) 50 nm, and (f) 65 nm.

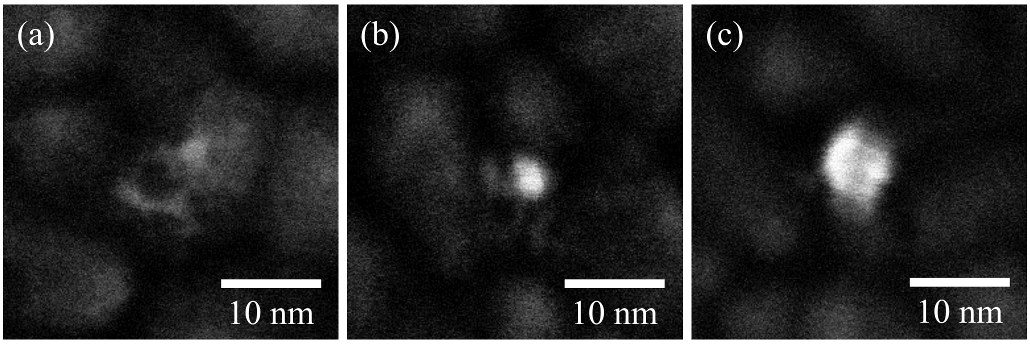

Fig. 3.3.2 SEM images of CoPt deposited with -0.9 V (vs. Ag/AgCl) for (a) 2.0 s, (b) 3.0 s, and (c) 5.0 s inside nanopore with 10 nm diameter

Moreover, the superparamagnetic properties of CoPt particles should be considered, as this is a critical issue for BPM with Tbit-level densities. For application in the recording layer of a hard disk drive, the energy barrier of magnetic materials is required to obey the following equation for permanent recording, where K_u is the magnetic anisotropy constant, V is the volume of the particles, k_B is Boltzmann constant, and T is temperature.

$$K_u V > 60 k_B T \tag{3.3.1}$$

In Eq. (3.3.1), the superparamagnetic limit occurs when the product of K_u and V is less than the right-hand side; thus, it is possible to determine the critical size D_p from the volume when K_uV equals $60k_BT$. If the CoPt nucleus is assumed to be a sphere, the critical particle diameter D_p is expressed by Eq. (3.3.2).

$$D_p = (60 \times 3/4\pi \times k_B T/K_u)^{1/3} \times 2 \tag{3.3.2}$$

The K_u value of hcp CoPt was 2.0×10^7 erg/cm^3 [18] and T was 298 K. According to Eq. 3.3.2, the critical size D_p was calculated as 6.2 nm. Based on this result, CoPt particles with a size of 2.0–3.0 nm are expected to be superparamagnetic. Therefore, to form CoPt nanodots consist of single grains, it is important to enhance the growth of CoPt by applying a less negative potential at which growth of the nucleus preferentially occurs to form larger size particles.

Hence, CoPt electrodeposition was carried out with less negative potential of -0.5 V, --0.6 V, -0.7 V (vs. Ag/AgCl), and difference in grain size with applied potential and deposition duration was compared with the results of -0.9 V (vs. Ag/AgCl). CoPt was deposited inside nanopores with 65 nm diameter with different applied potentials; corresponding SEM images are shown in Fig. 3.3.3. Figs. 3.3.3 (a, b), (c, d), (e, f), and (g, h) correspond to the images of CoPt nuclei deposited at -0.5 V, -0.6 V, -0.7 V, and -0.9 V (vs. Ag/AgCl) with different deposition durations. As seen in the images, current crowding effect was clearly observed in all deposition conditions owing to the wide diameter of the nanopore, CoPt preferentially nucleated from the edge of the nanopore as observed in Fig. 3.3.1. It can also be seen that the size of the nuclei increased and the number of nuclei decreased as the applied potential became less negative; for example, at the early deposition stage, the size of the nuclei was 4.0–5.0 nm at -0.5 V and -0.6 V (vs. Ag/AgCl) [Figs. 3.3.3 (a) and (c)], whereas fine nuclei of 2.0–3.0 nm were observed at -0.9 V (vs. Ag/AgCl) [Fig.3.3.3 (g)]. At the later deposition stage, the number of nuclei rarely differed from that at the early stage and the nuclei size increased in less negative potential; CoPt grew to a diameter of 8.0–10 nm, 5.0–7.0 nm, and 4.0–5.0 nm at -0.5 V, -0.6 V, and -0.7 V (vs. Ag/AgCl), respectively [Figs.3.3.3 (b), (d), and (f)], whereas dense cluster of fine nuclei of 2.0–3.0 nm were observed at -0.9 V (vs. Ag/AgCl) [Figs.3.3.3 (h)] owing to the continuous nucleation at the Ru surface or on the nucleated CoPt grains. These results observed at less negative potentials indicated that the growth of CoPt nuclei preferentially occurs over formation of a new nucleus, and thus a single nucleus should be grown in 10 nm nanopores using this potential range.

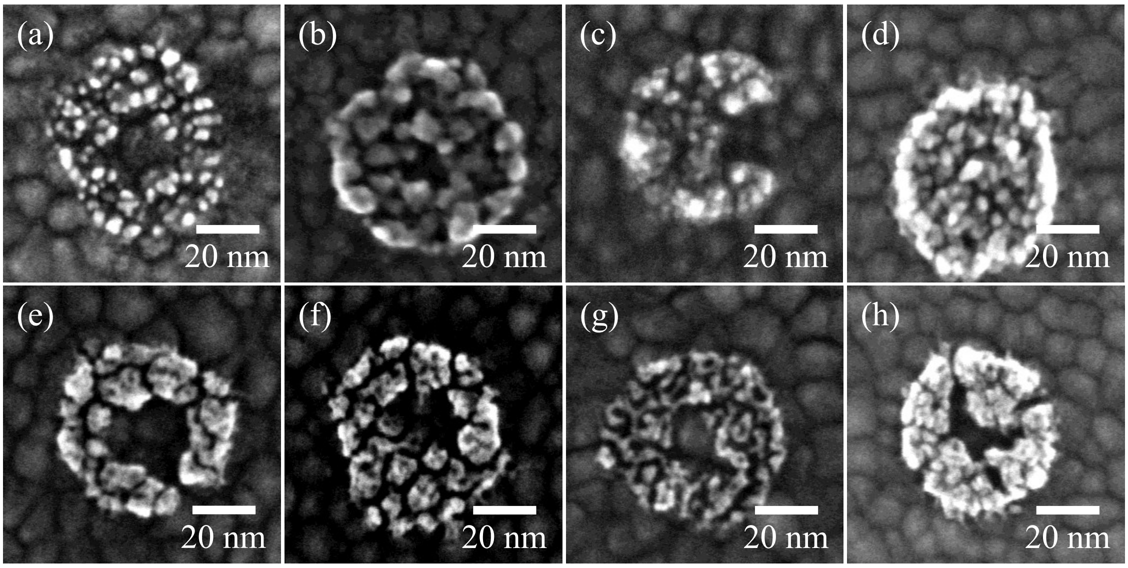

Fig. 3.3.3 SEM images of CoPt deposited inside nanopore with 65 nm diameter at - -0.5 V for (a) 60 min and (b) 960 min (16 h), at -0.6 V for (c) 30 min and (d) 60 min, at -0.7 V for (e) 250 s and (f) 290 s, and at -0.9 V for (g) 2.0 s and (h) 5.0 s.

Figure 3.3.4 shows the SEM images of CoPt deposited with different applied potentials inside 10 nm nanopores. At less negative potentials, deposition of a single nucleus was observed inside the nanopore that grew to a diameter of 10 nm, whereas the grain boundaries were observed for the CoPt nanodot deposited at -0.9 V (vs. Ag/AgCl). These results suggested the successful deposition of a single grains inside the nanopore that grow to form nanodot arrays with single crystal structure by adjusting the applied potential to control the number and size of

CoPt nuclei.

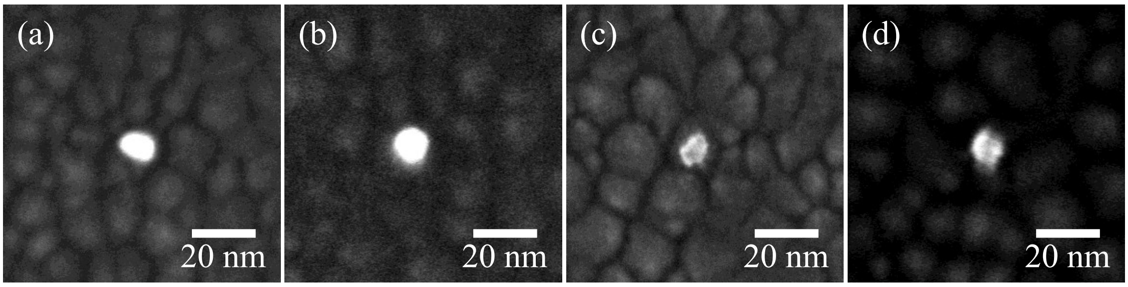

Fig. 3.3.4 SEM images of CoPt deposited at (a) - -0.5 V for 960 min (16 h), at (b) -0.6 V for 30 min, at (c) -0.7 V for 200 s, and at (d) -0.9 V for 5.0 s inside nanopore with 10 nm diameter.

3.3.2 Analysis of Distribution of CoPt Nuclei inside Nanopores

As described in chapter 3.3.1, single nucleus was successfully deposited inside the nanopore by applying less negative potential to suppress the nucleation density. The reason for the deposition of a single nucleus inside 10 nm nanopores is not only the difference of nucleation density but also the difference in the size of the nucleation exclusion zone with applied potential. When a nucleus is formed on the surface, a region with reduced supersaturation is created around the nucleus that inhibits further nucleation. Milchev et al. [19] and Scharifker et al. [20-21] reported that the nucleation and growth rates and spatial distribution of nuclei were affected by the inhibited region with reduced supersaturation. Thus it is significant to consider the size of the inhibited region to analyze the initial deposition stage, especially when the nucleation takes place inside the ultra-fine nanopore. In the case of the smaller nanopores, the bottom surface could be covered by the nucleation exclusion zone, thus single nucleus subsequently grow as a single crystal without formation of a new nucleus with less negative potentials. In order to confirm this hypothesis, the size of exclusion zone should be estimated, thus the distribution of CoPt nuclei with different applied potential was investigated by analyzing the nucleation density and nearest neighbor distance of nuclei.

Figure 3.3.5 shows SEM images of CoPt nuclei deposited at -0.7 and -0.9 V (vs. Ag/AgCl) inside nanopores with 20 nm in diameter and 50 nm in pitch. The duration times were set to 15 min and 3 s for -0.7 and -0.9 V (vs. Ag/AgCl), respectively, as an initial nucleation stage so that dispersed CoPt nuclei can be observed. Although, several cracks, which could be caused by the CMP process, smooth Ru surface with small amount of grain boundary was observed. Because the diameter of the nanopore is 20 nm, multiple-nucleation was observed in both potentials, and CoPt nucleated from the outer side of the nanopore due to the current crowding. By using the SEM images in Fig. 3.3.5, the image analysis was applied to measure the nucleation density inside the nanopores. The eight positions were randomly selected while avoiding the cracks on the Ru surface. The positions were numbered at the bottom of the nanopores in Figs. 3.3.5 (a) and (b), respectively. The measured number of nuclei and nucleation density, N_o, in each position are summarized in Tables 3.3.1 and 3.3.2. In the image analysis, the partilces with less than 2.0 nm^2 were excluded because the diameter of the nuclei is assumed to be 2.0 nm at the initial stages in Figs. 3.3.1-3.3.3. The area of the nanopores is assumed as circle with 20 nm in diameter. As seen in the tables, the nucleation density decreased at less negative potential in every selected positions as expected, which correponds to the results as observed in Figs. 3.3.3 and 3.3.4; the average nucleation density, N_0 was 0.018

nm^{-2} and 0.031 nm^{-2} for -0.7 V and -0.9 V (vs. Ag/AgCl), respectively.

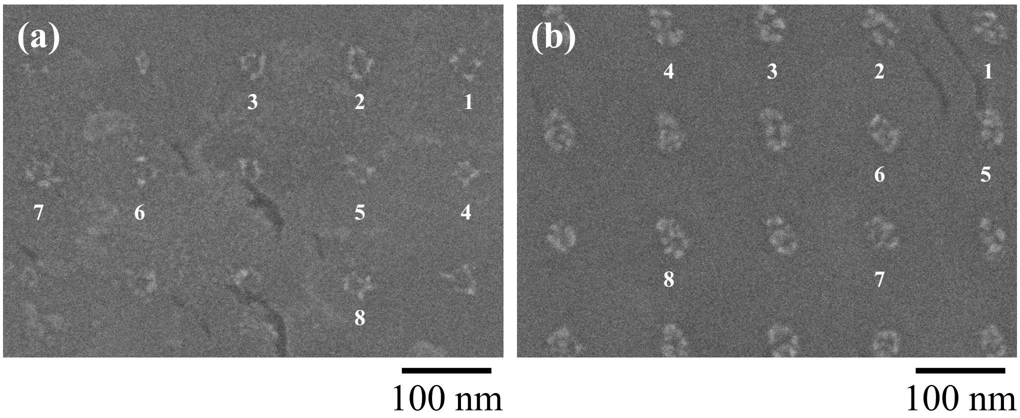

Fig. 3.3.5 SEM images of CoPt deposited at (a) -0.7 V and (b) -0.9 V (vs. Ag/AgCl) inside nanopores with 20 nm in diameter and 50 nm in pitch.

Table 3.3.1 Number of nuclei and nucleaetion density of CoPt deposited at -0.7 V

Position	Number of nuclei	N_o / nm^{-2}	Average N_o / nm^{-2}
1	4	0.013	0.018
2	5	0.016	
3	8	0.025	
4	6	0.019	
5	4	0.013	
6	4	0.013	
7	7	0.022	
8	6	0.019	

Table 3.3.2 Number of nuclei and nucleaetion density of CoPt deposited at -0.9 V

Position	Number of nuclei	N_o / nm^{-2}	Average N_o / nm^{-2}
1	9	0.029	0.031
2	8	0.025	
3	9	0.029	
4	11	0.035	
5	10	0.032	
6	10	0.032	
7	10	0.032	
8	12	0.038	

In order to further investigate the nuclei distribution, inter-nucleus distances in the SEM images were measured by image analysis. The probability distribution of measured distances between first r_1, second r_2, and third r_3 nearest neighbor nuclei were shown in Fig. 3.3.6 for -0.7 V and -0.9 V (vs. Ag/AgCl), respectively. In addition, neareset neighbor distances were also estimated based on the poisson probability distribution. The distance of jth-neighbors nucleus for the poassion probability distribution can be expressed by

$$dP(r_j) = \frac{2}{(j-1)!}(\pi N_0)^j r_j^{2j-1} \exp(-\pi r_j^2 N_0) dr_j \tag{3.3.3}$$

where N_0 is the nucleation density and r_j is the distance between the jth-neighbor nucleus. From the Eq. (3.3.3), the average distances between first r_1^*, second r_2^*, and third r_3^*nucleus are expressed as;

$$r_1^* = \frac{1}{2\sqrt{N_0}} \tag{3.3.4}$$

$$r_2^* = \frac{3}{4\sqrt{N_0}} \tag{3.3.5}$$

$$r_3^* = \frac{15}{16\sqrt{N_0}} \tag{3.3.6}$$

The nearest neighbor distanes were calculated by Eqs. (3.3.4-3.3.6) using experimentaly measured nucleation density, N_0, of 0.018 and 0.031 nm^{-2} as listed in Tables 3.3.1 and 3.3.2. The average of experimental nearest neighbor distance data and calculated data are summarized in Table 3.3.3.

From the histograms in Fig. 3.3.6 and Table 3.3.3, the measured first neighbor distance r^1 was larger than the value calculated from poisson probability distribution in both applied potentials. Because the exclusion zone corresponds to the hemispherical diffusion zone of metal ions, the radius of the zone, δ, grows along with deposition duration, t, as described as $\delta = (kDt)^{1/2}$, where k is a numerical constant, D is diffusion coefficient of metal ions. Thus, it can be said that the difference in the experimental and theoretical values is attributed to the growth of nucleation exclusion zone around each growing nucleus.

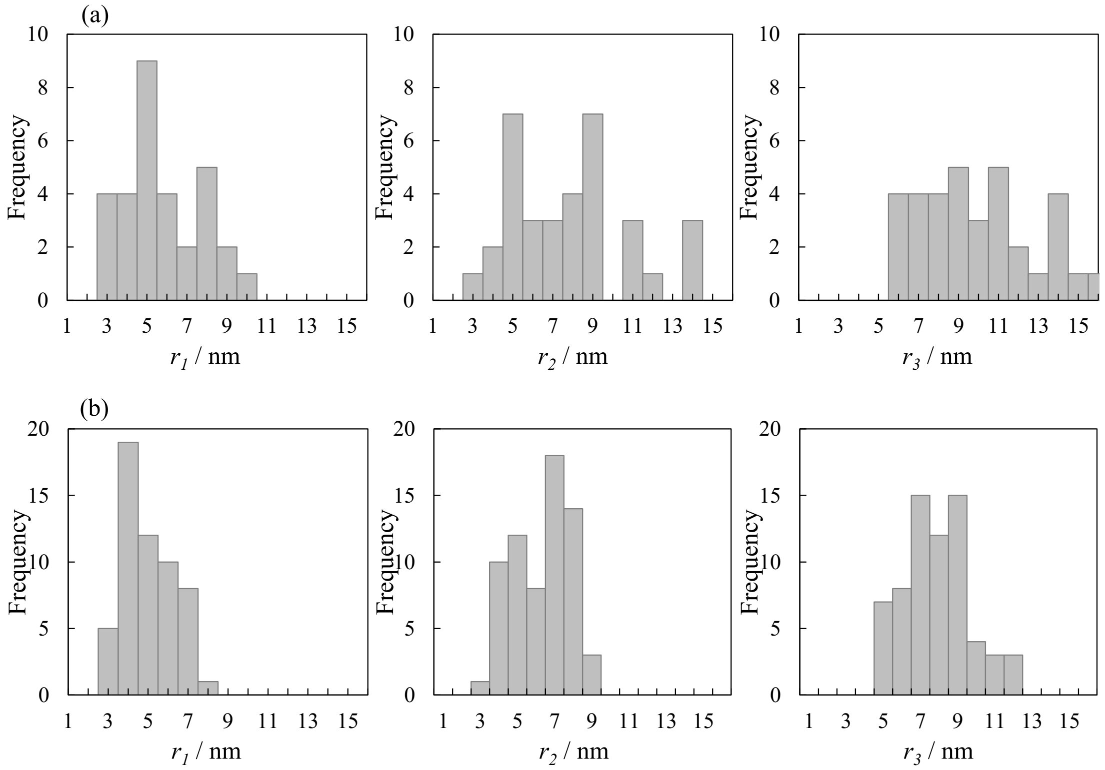

Fig. 3.3.6 Probability distribution of measured distances between first r_1, second r_2, and third r_3 nearest neighbor nuclei deposited at (a) -0.7 V and (b) -0.9 V (vs. Ag/AgCl).

Table 3.3.3 Experimental and analytical data of nearest neighbor distance

	Potential	Nearest neighbor distance / nm		
	/ V	first, r_1	second, r_2	third, r_3
Experimental	-0.7	5.3	7.3	9.3
data	-0.9	4.5	5.8	7.3
Analytical	-0.7	3.8	5.7	7.1
data	-0.9	2.8	4.2	5.3

In addition, nearest neighbor distance increased with -0.7 V (vs. Ag/AgCl) compared to -0.9 V (vs. Ag/AgCl). Chen et al. described the size dependence of exclusion zone on overpotential with theoretical model [22]. In this model, the distance from a growing nucleus, which nucleation rate decreases by the ratio of the nucleation rate at ρ to that on the surface without nucleus, J_{rel}, was described as Eq. (3.3.7).

$$\rho(t) = \frac{\left(\sqrt{A^2 + 8ABV_M t} - A\right)^3}{16Dc_\infty V_M C^3 t\left(1 - J_{rel}^{\frac{1}{1+n_k}}\right)}$$

$$A = c^* DFn$$

$$B = \frac{J_o^2}{Fn}\left[\exp\left(\frac{2anF\Delta E}{RT}\right) - \exp\left(\frac{(2a-1)nF\Delta E}{RT}\right)\right]$$

$$C = j_o \exp\left(\frac{anF\Delta E}{RT}\right) \tag{3.3.7}$$

Where c^* is a bulk concentration of metal ions, D is a diffusion coefficient of metal ions, F is the Faraday constant, n is a transferred electron number, J_o is an exchange currend density, a is a transfer coefficient (a=0.5), ΔE is an applied potential, R is the gas constant, T is a temperature, V_M is a molar volume, t is a deposition duration, n_k is a number of atoms for a stable nucleus, 30-40 atoms. Chen et al. considered the exclusion zone as an area where nucleation rate is reduced by one order of magnitude, thus, exclusion zone was estimated by calculating the distance, ρ, from a growing nucleus from Eq. (3.3.7) with J_{rel} of 0.1. From this equation, the distance ρ decreases with lower overpotential, which indicates that more negative potential results in the long radius of exclusion zone. However, as described in Table 3.3.3, the nearest neighbor distance decreased at more negative potential, which is contradictory to Eq. (3.3.7). The short distance of nearest neighbor of CoPt nuclei could be due to the multiple-nucleation inside the nanopores. In the theoretical model, a single nucleus was taken into account for the calculation of distance ρ, however, in the case of multiple-nucleation, CoPt simultaneously nucleated inside the nanopore before the growth of exclusion zone. Especially, in the case of high overpotential, such as -0.9 V (vs. Ag/AgCl) for the deposition of CoPt, high nucleation density leads to the short distance of nearest neighbor. On the other hand, in the case of lower overpotential of -0.7 V (vs. Ag/AgCl), the nucleation density is lower than that of -0.9 V (vs. Ag/AgCl), which led exclusion zone to grow inside the nanopores resulting in the longer nearest neighbor distance.

In addition, the nearest neighbor distance corresponds to radius of exclusion zone. Thus, in the case of -0.7 V (vs. Ag/AgCl), exclusion zone with radius of 5.3 nm grows around the nucleus and covers the Ru surface inside 10 nm nanopores to hinder the formation of a new nucleus, resulting in the formation of a single nucleus inside the nanopores. On the other hand, in the case of -0.9 V (vs. Ag/AgCl), the radius of exclusion zone is 4.5 nm, which results in the multiple-nucleation of CoPt inside the 10 nm nanopores.

Based on the detail analysis of distribution of CoPt nuckei inside the nanpores, it was indicated that the deposition of single nucleus inside 10 nm nanopores at less negative potential is attributed to the difference in nucleation density and size of the nucleation exclusion zone. In order to further discuss the difference in the exclusion zone with applied potential, relation between both the propagation rate of exclusion zone and nucleation rate of metal with applied potential should be analyzed in the next step.

3.4 Fbrication of CoPt Nanodot Arrays with Single Crystal Structure

Considering the growth conditions of CoPt deposited at less negative potentials (> -0.7 V) as observed in chapter 3.3.1 and 3.3.2, nanodot arrays should exhibit single crystal structure with high crystal orientation from Ru underlayer. Figure 3.3.7 shows cross-sectional TEM images of CoPt deposited with -0.9, -0.7, and -0.6 V (vs. Ag/AgCl) inside 10 nm nanopores. To confirm the above assumption, we observed the growth conditions of CoPt inside nanopores using TEM. In Figs. 3.3.7 (a) and (b), the thickness of the EB resist was reduced from 30 to 20 nm by the excimer-UV pretreatment, and mushroom-shaped nanodot arrays were observed owing to overfilling of CoPt. In this overfilled region, a polycrystalline structure with fine grain structure was confirmed, which may be due to hemispherical diffusion of metal ions to expand the CoPt nucleation site. Nevertheless, columnar structures of nanodot arrays without voids were observed inside the nanopore. Figures 3.3.7 (d), (f), and (h) show high magnification TEM images of the interface between CoPt and Ru, and the insets show the electron beam diffraction of each nanodot. In these images, lattice fringes in the direction perpendicular to the Ru interface were observed. Furthermore, the diffraction images showed rings and spots corresponding to hcp (002), indicating that CoPt grew along the Ru crystal orientation with high crystallinity in the initial deposition stage, which is expected to induce perpendicular magnetic anisotropy in the nanodot arrays. In addition, from the diffraction images, diffraction rings and diffraction spots that correspond to polycrystalline and single crystalline structures were observed for -0.9 V (vs. Ag/AgCl) and the less negative potentials of -0.7 V and -0.6 V (vs. Ag/AgCl), respectively, indicating different CoPt growth conditions for -0.9 V (vs. Ag/AgCl) and the less negative potentials. Figures 3.3.7 (g) and (h) show higher magnification TEM images of the upper part of the CoPt nanodot. In Fig. 3.3.7 (g), the CoPt lattice is randomly oriented, suggesting that multinucleation, including secondary nucleation, occurs to form grain boundaries at -0.9 V (vs. Ag/AgCl), which resulted in a nanodot with a polycrystalline structure. On the other hand, in Figs. 3.3.7 (f) and (h), clear stacking of hcp lattices without any grain boundaries was observed, even in the upper section of the nanodot. These results indicated that, with a less negative potential, a single nucleus of CoPt was formed inside the nanopore that subsequently grew from the interface of Ru in a perpendicular orientation to form a single crystalline structure.

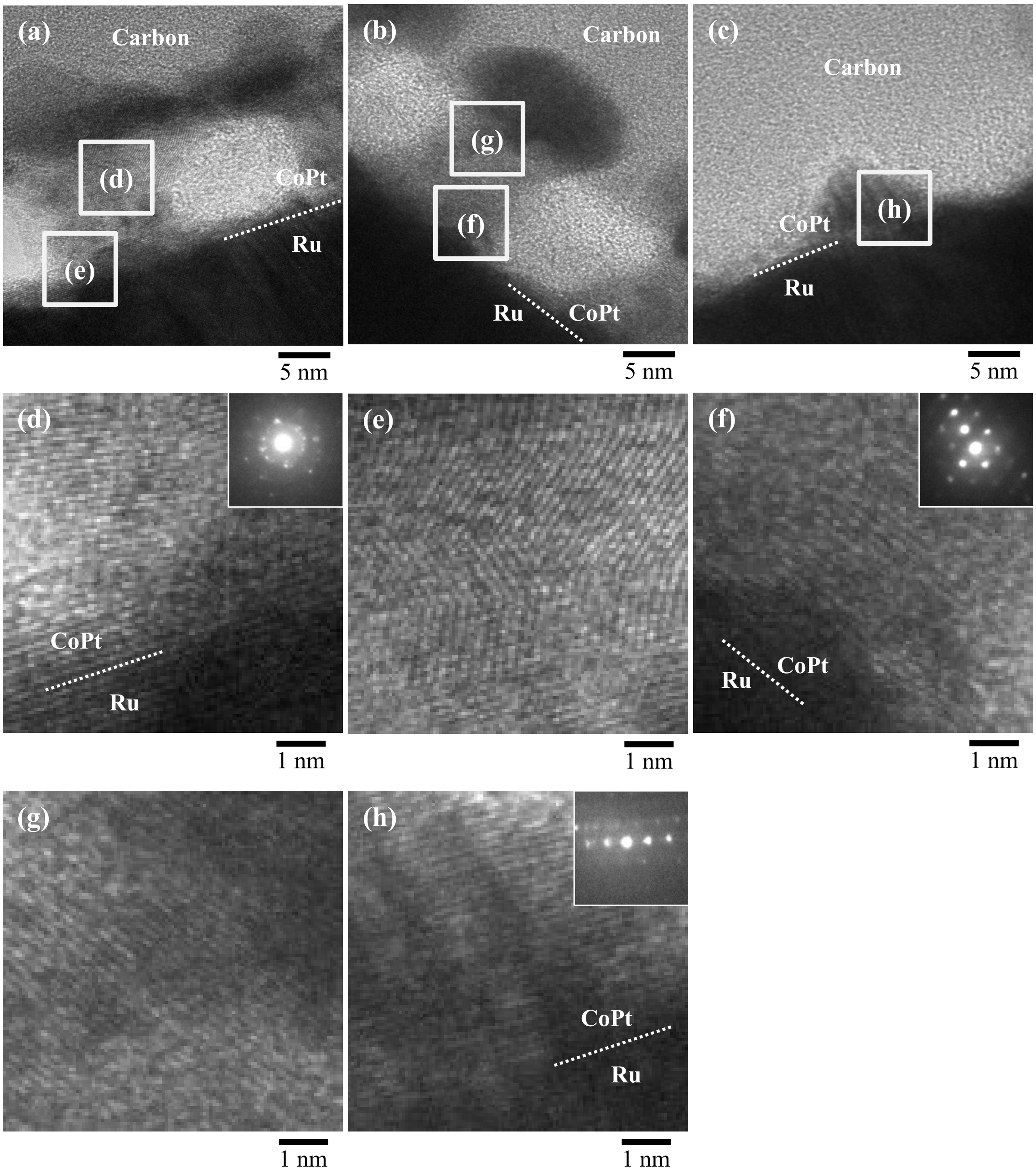

Fig. 3.3.7 Cross sectional TEM images of CoPt nanodot arrays with 10 nm diameter and 35 nm pitch deposited with (a) -0.9 V, (b) -0.7 V and (c) -0.6 V (vs. Ag/AgCl). High magnification images at (d, f, h) interface of CoPt and Ru substrate and (e, g) upper part of CoPt nanodot arrays. The insets show the electron beam diffraction of nanodot arrays deposited with each potential.

Because the magnetic anisotropy and magnetic domain structure are sensitive to slight changes in crystal structure, the coercivity of nanodot arrays should be strongly influenced by the applied potential, as a difference in crystal structure with potential was suggested in Fig. 3.3.7. To investigate the effect of the applied potential on the coercivity of CoPt, we analyzed the magnetic properties and crystal structure of CoPt continuous films. Because the deposition rate is extremely slow at -0.6 V (vs. Ag/AgCl), CoPt was deposited at -0.7 V and -0.9 V (vs. Ag/AgCl) to compare the difference in coercivity and crystal structure. The concentration of $Pt(NH_3)_2(NO_2)_2$ was optimized to 2.1 and 3.0 mmol L^{-1} for -0.7 and -0.9 V (vs. Ag/AgCl), respectively to set the alloy composition close to Co:Pt = 80:20; the composition of Pt is tend to increase at less negative potential, thus the concentration of Pt electrolyte was lowered at less negative potential.

Figure 3.3.8 shows the out-of-plane hysteresis loops of CoPt continuous films deposited with -0.7 and -0.9 V (vs. Ag/AgCl) with thicknesses of 16 and 17 nm, respectively; composition, coercivity, and squareness of the CoPt continuous films are summarized in Table 3.3.4. From the hysteresis loops, the coercivity of the CoPt continuous film deposited at -0.7 V (vs. Ag/AgCl) was higher than that of the film deposited at -0.9 V (vs. Ag/AgCl), even though this film had a larger deviation from the ideal composition of CoPt = 80:20; the composition of the films were CoPt = 70:30 and 79:21 with -0.7 and -0.9 V (vs. Ag/AgCl), respectively.

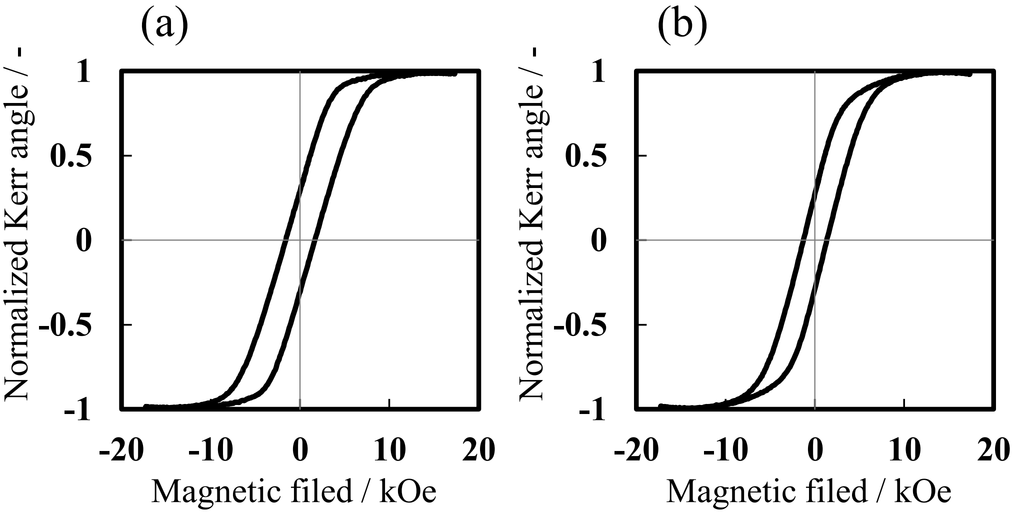

Fig. 3.3.8 Out-of-plane hysteresis loops of CoPt continuous films deposited at (a) -0.7 V and (b) -0.9 V (vs. Ag/AgCl).

Table 3.3.4 Measured coercivity and squareness of CoPt continuous films

Potential / V	Thickness / nm	Composition / at%	Coercivity / kOe	Squareness
-0.9	17	$Co_{79}Pt_{21}$	1.3	0.28
-0.7	16	$Co_{70}Pt_{30}$	1.7	0.30

To evaluate the change in coercivity with potential, crystal structure of the CoPt films was analyzed by XRD measurements; corresponding XRD patterns are shown in Fig. 3.3.9. The XRD patterns of the CoPt films showed peak around at 43° corresponding to hcp (002), indicating that CoPt grew in a perpendicular direction along with Ru (002) plane. In the case of -0.7 V (vs. Ag/AgCl), the hcp (002) peak appeared at around 42.7° to overlap the peak of Ru hcp (002), whereas peak was appeared at 43.5° for -0.9 V (vs. Ag/AgCl). The main reason for this shift is the change in the composition of the film. In substitutional solid solutions, it is known that the lattice constant changes with respect to the composition of the alloy in accordance with Vegard's law. Thus, when the composition of Pt, which has a larger atomic radius than Co, increases, the lattice spacing of CoPt increases, resulting in a lower 2θ value. In order to investigate the peak shift, the 2θ value for each composition was calculated according to Vegard's law. The lattice constant a is expressed by Eq. (3.3.7).

$$a = \frac{2r_{Co}x + 2r_{Pt}(100 - x)}{100} \tag{3.3.7}$$

where r_{Co} is the atomic radius of Co (125 pm), r_{Pt} is the atomic radius of Pt (139 pm), and x is the composition of Co (%). The relation between the lattice constant and lattice spacing is expressed by Eq. (3.3.8).

$$\frac{1}{d^2} = \frac{4}{3}\left(\frac{h^2 + hk + k^2}{a^2}\right) + \frac{l^2}{c^2} \tag{3.3.8}$$

In the case of hcp (002), the (h,k,l) value is (002), and thus the lattice spacing c is described as $c = 2d$. As the ratio of the lattice constants a and c for CoPt is known to be $c = 1.63a$. Based on these equations, the lattice spacing d was calculated, and 2θ was obtained from the Bragg equation [Eq. (3.3.9)], where n is an integer and λ is the wavelength of the incident wave (1.54178 Å for CuKα).

$$d = \frac{n\lambda}{2\sin\theta} \tag{3.3.9}$$

The 2θ values calculated from the composition of each film were 43.5° (CoPt = 79:21) for -0.9 V (vs. Ag/AgCl) and 43.0° (CoPt = 70:30) for -0.7 V (vs. Ag/AgCl). In the case of -0.9 V (vs. Ag/AgCl), the calculated angle was the same as that observed in the XRD pattern. On the other hand, in the case of -0.7 V (vs. Ag/AgCl), because the peak in the pattern is shifted to a lower angle than that calculated using Vegard's law, a further increase in the lattice spacing was suggested. This indicates that CoPt has grown along the Ru crystal orientation, which has slightly larger lattice spacing than CoPt, to broaden its lattice spacing. This epitaxial-like growth could enhance the perpendicular magnetic anisotropy and increase the coercivity of the film deposited with -0.7 V (vs. Ag/AgCl). In addition, the peak intensity was higher at -0.7 V compared to that of -0.9 V, indicating higher crystallinity of hcp (002) structure at less negative potential. This increase in crystallinity could be attributed to the homogenization of alloy composition from the initial deposition stage. Table 3.3.5 shows the alloy composition of CoPt continuous films with different thickness deposited at -0.6 V (vs. Ag/AgCl). In the case of -0.6 V (vs. Ag/AgCl), because the overpotential is significantly small it is difficult control the alloy composition, thus the composition deviated from the ideal alloy composition. However, the composition rarely changed along with the film thickness. Because the diffusion limited growth is mitigated at less negative potential due to the slow deposition rate, composition gradient with film thickness was reduced, which could form hcp structure from the initial deposition stage. This improvement in the crystallinity may correspond to the results observed under forced convection conditions in chapter 2.

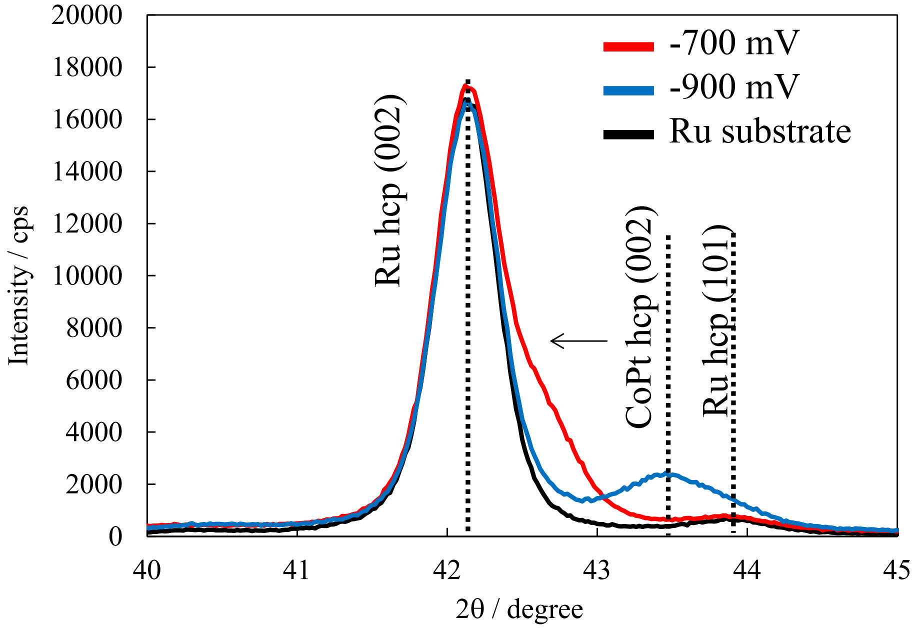

Fig. 3.3.9 XRD patterns of Ru substrate and CoPt continuous films deposited at -0.7 V and -0.9 V (vs. Ag/AgCl).

Table 3.3.5 Alloy composition of CoPt continuous films deposited at -0.6 V

Thickness / nm	Alloy composition	
	Co/ at%	Pt/ at%
2	68	32
3	63	37
12	69	31

By controlling the nucleation and growth behavior of CoPt, the attempt to fabricate single crystal CoPt nanodot arrays was successful. Based on the above results, nanodot arrays consist of single crystal should exhibit high coercivity due to the high crystallinity with high orientation in the perpendicular diection. In order to further investigate the difference of coerivity of CoPt nanodot arrays with crystal structure, nanodot arrays should be analyzed with polar magneto-optical μ-Kerr effect device.

Conclusion

In the present work, the initial electrodeposition stages of CoPt inside ultra-fine nanopores were analyzed to fabricate CoPt nanodot arrays with a single crystalline structure. At -0.9 V (vs. Ag/AgCl), the number of nuclei decreased in smaller nanopores, but multinucleation was observed, even in 10 nm nanopores. On the other hand, at less negative potentials (> -0.7 V), growth of the nucleus is preferential, and a single nucleus was formed inside the 10 nm nanopore that grew to form a columnar-structured grain with a size of 7.0–10 nm. It was suggested from the analysis of distribution of CoPt nuclei inside the nanopore that the growth of single nucleus was attributed to the difference of the nucleation density and the size of the nucleation exclusion zone; excusion zone was larger at less negative potential, which covered the surface of Ru inside the 10 nm nanpores to hinder a formation of a new nucleus. Cross-sectional TEM images confirmed that, at less negative potentials, CoPt grew as a single crystal with clear stacking of hcp lattices in the direction perpendicular to the interface of Ru. In addition, at less negative potentials, CoPt grew along the Ru crystal orientation during the initial deposition stage to increase the coercivity of the CoPt films.

Based on the detailed analyses of nucleation process inside the nanopore, precise control in the nucleation density and grain size of the CoPt was successfully demonstrated to form Tbit/in^2 nanodot arrays exhibiting single crystal feature, which is highly desirable for the BPM application. In addition, the quantitative analyses of nucleation exclusion zone of nucleus with single nano-meter should be beneficial for the fabrication of nanostructures by electrochemical process, since there has been few reports regarding the analysis of exclusion zone at nanoscale region.

References

[1] O. Hellwig, J. K. Bosworth, E. Dobisz, D. Kercher, T. Hauet, G. Zeltzer, J. D. Risner-Jamtgaard, D. Yaney, and R. Ruiz, *Appl. Phys. Lett.*, 96 (2010) 052511.

[2] Y. Kamata, A. Kikitsu, H. Hieda, M. Sakurai, K. Naito, J. Bai, and S. Ishio, *Jpn. J. Appl. Phys.*, 46 (2007) 999.

[3] B. R. Scharifker and G. Hills, *Electrochim. Acta*, 28 (1983) 879.

[4] B. R. Scharifker and J. Mostany, *J. Electroanal. Chem.*, 177 (1984) 13.

[5] W.S. Kruijt, M. Sluyters-Rehbach and J.H. Sluyters, *J. Electroanal. Chem.*, 371 (1994) 13.

[6] R.M. Penner, *J. Phys. Chem. B*, 106 (2002) 3339

[7] A. Radisic, P.M. Vereecken, J.B. Hannon, P.C. Searson, and F.M. Ross, *Nano Lett.*, 6 (2006) 238

[8] A. Radisic, F. M. Ross, and P. C. Searson, *J. Phys. Chem. B*, 110(2006) 7862.

[9] J. Ustarroz, X. Ke, A. Hubin, S. Bals, and H. Terryn, *J. Phys. Chem. C*, 116 (2012) 2322.

[10] J. V. Zoval, J. Lee, S. Gorer, and R. M. Penner, *J. Phys. Chem. B*, 102 (1998) 1166.

[11] J.M. Sieben, M.M.E. Duarte, and C.E. Mayer, *J. Solid State Electrochem.*, 14 (2010) 1555.

[12] I. Lee, K-Y. Chan, and D.L. Phillips, *Appl. Surf. Sci.*, 136 (1998) 321.

[13] P. Dixit and J. Miao, *J. Electrochem. Soci.*, 153 (2006) G522

[14] R. Beica, C. Sharbono, T. Ritzdorf, *Proc. 2008 Electronic Components and Technology Conference*, Orlando, FL, May. 2008, 577

[15] T-H. Tsai and J-H. Huang, *Microele. Eng.*, 88 (2011) 195.

[16] L. T. Romankiw, *Electrochim. Acta*, 12 (1997) 2985.

[17] Y. Tian, C. Liu, D. Hutt, and B. Stevens, *J. Electron. Mater.*, 43 (2014) 594

[18] D. Weller, A. Moser, L. Folks, M. E. Best, W. Lee, M. F. Toney, M. Schwickert, J. U. Thiele, and M. F. Doerner, *IEEE Trans. Magn.*, 36 (2000) 10.

[19] A. Milchev, W. S. Krujit, M. S-Rehbach, and J. H. Sluyters, *J. Electroanal. Chem.*, 350 (1993) 89.

[20] B. Scharifker and G. Hills, *Electrochim. Acta*, 7 (1983) 879.

[21] B. Scharifker and J. Mostany, *J. Electroanal. Chem.*, 177 (1984) 13.

[22] S. Chen and A. Kucernak, *J. Phys. Chem. B*, 197 (2003) 8392.

Chapter 4

Development of Electrodeposition Process for Fabrication of FePt Nanodot Arrays with Tbit/in^2 Areal Density

4.1 Introduction

The equiatomic FePt ordered alloy with $L1_0$ phase has been considered as one of the most promising candidates for the use in ultra-high density perpendicular magnetic recording media due to its high magnetocrystalline anisotropy, K_u, which enables to minimize the grain size down to around 2.0 nm for sufficient thermal stability [1-3]. Utilizing this feature, $L1_0$-FePt alloy have been extensively studied for data storage applications to achieve Tbit-level areal recording density, for example, energy-assisted magnetic recording [4] and bit-patterned media (BPM) [5, 6]. BPM enables to reduce the coupling of each magnetic grain and to increase the grain size by storing the data in physically separated arrays of ferromagnetic nanodots, thus high signal-to-noise ratio (SNR) and thermal stability can be achieved [7, 8].

In researches of electrodeposited FePt films, at the very negative potential required for Fe deposition, hydrogen gas evolution occurs, resulting in incorporation of hydroxides and oxides of Fe to increase oxygen composition of the film and, furthermore, Pt deposited under diffusion limited condition, leading to porous films with rough surface [9, 10]. These conditions were considered as critical issues to improve the coercivity of FePt films. G. Zangari et al. have developed a bath which overcomes these problems and they have succeeded to deposit FePt films with low oxygen content and smooth surface as well as with high coercivity of 13 kOe [11-13]. In this bath system, Pt complex was changed from Pt chlorides, as conventionally used, to amino-nitrite complex ($Pt(NH_3)_2(NO_2)_2$) to shift the onset of Pt reduction to more negative potential where co-deposition of Fe occurs, yielding a smooth surface and, furthermore, Fe is present as Fe(III)-citrate in the electrolyte, which is more stable than Fe(II)-citrate complex at alkaline pH to avoid precipitation of Fe as hydroxides or oxides, resulting in low oxygen content in deposited films.

As mentioned above, electrodeposition have been demonstrated as suitable process for fabricating films of high K_u materials, it is expected to apply in fabrication of nandot arrays by utilizing patterned nanopore substrate formed via lithography technique. Despite many studies on the electrodeposition of FePt have been reported, there is no report of fabrication of ultra-fine

FePt nanodot arrays by electrochemical methods for the application in BPM. Thus, in this study, in order to demonstrate the electrochemical fabrication process of Tbit-level nanodot arrays consisting of high K_u materials, FePt nanodot arrays were fabricated by combining lithography technique and electrodeposition. In addition fabrication process, such as deposition conditions of FePt with high coercivity and annealing process of nanodot arrays, were investigated in detail. Electrodeposition of FePt was carried out based on the bath system proposed by Zangari et al.

4.2 Experimental

4.2.1 Deposition Conditions of FePt Nanodot Arrays

FePt continuous films and nanodot arrays were electrodeposited from the electrolyte summarized in Table 4.2.1, which was based on the bath proposed by Zangari et al.. The bath temperature was 75 ^{o}C, and the pH was adjusted to 8 by diluted KOH. All electrochemical measurements were performed utilizing potentiostat (HZ-7000, Hokuto Denko); a Pt mesh and Ag/AgCl electrode were used as counter electrode and reference electrode, respectively. FePt alloy was deposited onto a 60 nm-thick Ru underlayer with 5 nm-thick Ti adhesion layer sputter deposited on n-Si (100) wafer. Post annealing to induce a phase transformation to the $L1_0$ ordered structure was performed utilizing a rapid thermal annealing device under forming gas (90 % Ar + 10 % H_2); samples were heated up to 500 or 650 ^{o}C with different holding times and ramp rates, and finally cooled down to room temperature. Details of the annealing conditions of FePt continuous films and nanodot arrays are listed in Table 4.2.2.

For the fabrication of FePt nanodot arrays, nanopore patterned substrate was formed onto Ru substrate with electron beam lithography (ELS-7500, ELIONIX) by the same fabrication process as described in chapter 2. Morphology of FePt nanodot arrays were observed by high-resolution scanning electron microscope (HR-SEM, S5500, Hitachi High-Tech.). Crystal structure of continuous films was analyzed by X-ray diffractometer (XRD, Rint-Ultima III, Rigaku); films with less than 100 nm thickness were analyzed with the grazing incidence angle of 0.4 ^{o}. Structural analysis of nanodot arrays was performed by transmitting electron microscope (TEM, JEM-2010, JEOL). Alloy composition of FePt continuous films and nandot arrays was determined by inductively-coupled plasma mass spectrometry (ICP-MS, 7700x, Agilent); 10 ppb of Rh was used as an internal standard. Magnetic properties of deposited continuous films were characterized by magneto-optical Kerr effect equipment (BH-810PC-WU, NEOARK). Prior to the characterization of the nanodot arrays all the resist was removed by exposing the samples with excimer UV irradiation for 2.0 min and rising with ethanol and UPW.

Table 4.2.1. Bath compositions and electrodeposition conditions of FePt

Chemicals	Concentration / mM
$(NH_4)_2C_6H_6O_7$	150
$Fe_2(SO_4)_3$	50
NH_2CH_2COOH	150
$NaNO_2$	100
$(NH_4)_2SO_4$	100
$Pt(NO_2)_2(NH_3)_2$	15
Bath temperature	75 °C
pH	8 (adjusted by KOH)
Reference electrode	Ag / AgCl
Counter electrode	Pt Mesh

Table 4.2.2. Annealing conditions

Atmosphere	$Ar+H_2$ 10 %
Annealing temperature	450-650 °C
Ramp rate	130-1950 °C/min
Holding time	0 min
Cooling	Water

Table 4.2.3 Operating conditions of electron beam lithography

Resist	ZEP520A-7 : ZEP-A = 1:2
Spin Coat	5000 rpm, 60 s
Prebake	180 °C, 3 min
Thickness of resist	30 nm
Accelerating voltage	50 kV
Beam current	20 pA
Dose value	10 fC / dot
Developer	IPA
Developing time	5 s
Developing temperature	5 °C
Rinse	UPW

4.3 Development of Fabrication Process of FePt Nanodot Arrays with Tbit/in^2 Areal Density

4.3.1 Deposition of L1$_0$-FePt Films with High Coercivity

To investigate the general characteristics of FePt electrodeposition, linear sweep voltammogram of FePt electrolyte was obtained at the scan rate of 50 mV s^{-1} (Fig. 4.3.1). The electrolyte showed a current onset at -0.2 V (vs. Ag/AgCl), and further voltammetric features were observed at -0.52 V and -0.85 V (vs. Ag/AgCl), which were corresponded to reduction of Pt and Fe. The current onset is attributed to the reduction of Fe(III) to Fe(II), followed by the onset of Fe reduction at -0.85 V (vs. Ag/AgCl). It should be noted that in the existence of Pt electrolyte, Zangari et al. [13] confirmed the codeposition of Fe at a potential 0.48 V more positive than the single Fe deposition due to the under potential codeposition of Fe by means of electrochemical quartz crystal microbalance. The significant increase in the current at more negative potential than -1.0 V was corresponded to hydrogen evolution reaction.

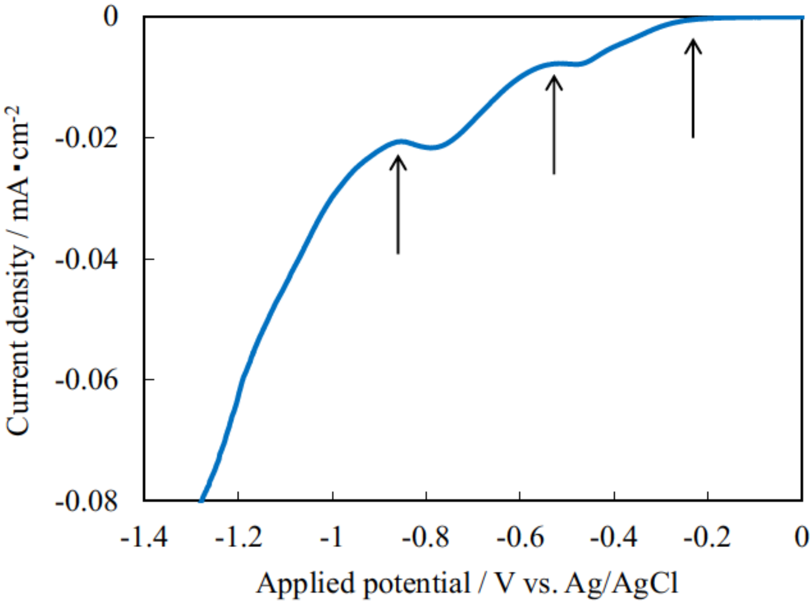

Fig. 4.3.1 Linear sweep voltammogram of FePt electrolyte. Scan rate was 50 mV s^{-1}.

Based on the electrochemical characteristics of FePt electrodeposition as described in Fig. 4.3.1, alloy composition of FePt films deposited on Ru substrate was optimized by adjusting the applied potential in order to deposit equiatomic FePt films, which is required to achieve $L1_0$ ordered structure. Figure 4.3.2 (a) shows the deviation of atomic fraction of Fe in 200 nm-thick alloy films with different applied potentials. As the potential increased in negative value, atomic fraction of Fe in the film increased, and near-equiatomic composition was obtained in the range of -1.0 V to -1.2 V (vs. Ag/AgCl). Figure 4.3.2 (b) shows the depth profile of alloy composition in 250 nm-thick FePt film deposited at -1.1 V (vs. Ag/AgCl). The deposited film showed a uniform composition ratio of Fe and Pt with thickness, and the oxygen content was less than 10 at%, indicating the low content of oxides or hydroxides of Fe formed by the hydrogen evolution reaction at this potential range.

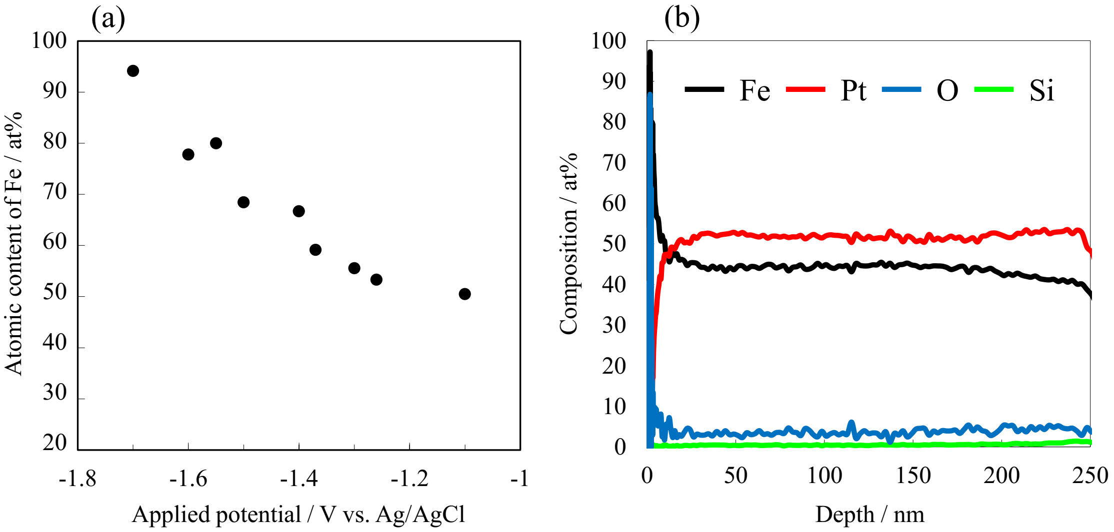

Fig. 4.3.2 Compositional analyses of deposited FePt continuous films. (a) Variation of atomic contents of Fe with different applied potentials. (b) Compositional depth profile of 250 nm thick FePt continuous films deposited at -1.1 V (vs. Ag/AgCl).

In order to investigate the phase transformation of FePt, 200 nm-thick continuous films deposited at -1.15 V were annealed for 60 min at 500 and 650 °C. XRD patterns of FePt continuous films are shown in Fig. 4.3.3. The sharp peak at 42.3 ° corresponds to hcp (002) of Ru underlayer. The as-deposited film showed a shoulder to Ru peak around 40.5 °, which corresponded to the peak of fcc disordered phase in (111) direction. Upon annealing, the (111) peak with higher intensity was clearly observed, and the peak shifted to higher 2θ value at 41.4 °. Due to the large lattice mismatch between FePt and Ru underlayer epitaxial-like growth of FePt is hardly occurs, resulting in the formation of the films with (111) preferred orientation. Although the (111) peak was observed, other characteristic peaks of $L1_0$ structure was not observed at 500 °C. On the other hand, peaks of (200), (110), and (001) of $L1_0$ ordered structure appeared at 650 °C, indicating the higher degree of phase transformation from fcc disordered structure to $L1_0$ ordered structure.

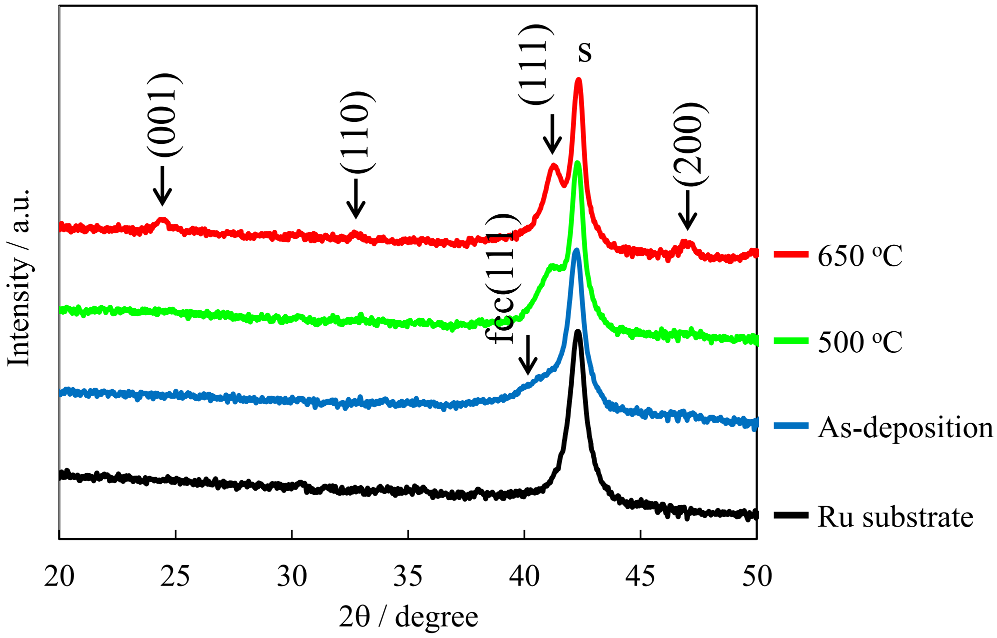

Fig. 4.3.3 XRD patterns of 200 nm-thick FePt continuous films deposited at -1.15 V (vs. Ag/AgCl). Thickness of the films was 200 nm.

To further investigate the phase transformation of $L1_0$ ordering, magnetic properties of the same samples as shown in Fig. 4.3.3 were measured by polar magneto-optical Kerr effect equipment; corresponding out-of-plane magnetic hysteresis loops are shown in Fig. 4.3.4 and measured coercivity and squareness were summarized in Table 4.3.1. The as-deposited films showed superparamagnetic feature due to the fcc structure of the deposited films. Upon annealing, significant magnetic hardening was observed; coercivity of 6.0 and 13.3 kOe and squareness of 0.65 and 0.93 were obtained for 500 °C and 650 °C, respectively. Higher values of coercivity and squareness at 650 °C are attributed to the higher degree of phase transformation to $L1_0$ structure as confirmed by XRD measurements in Fig. 4.3.3.

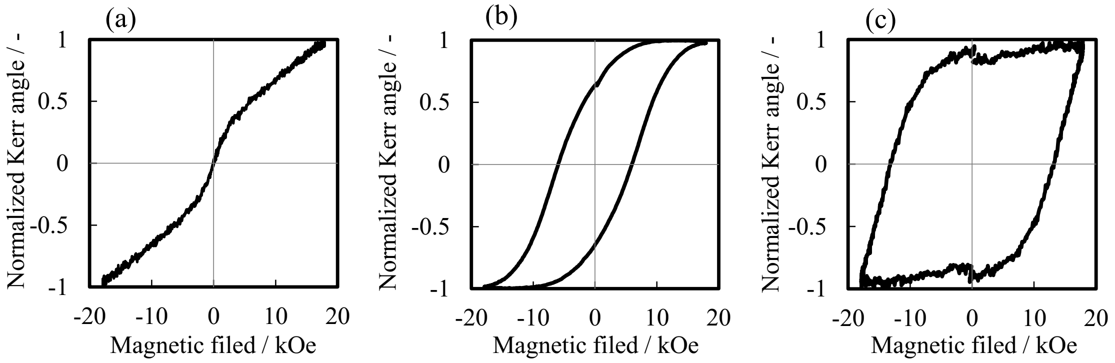

Fig. 4.3.4 Out-of-plane hysteresis loops of FePt continuous films (a) as-deposition, (b) annealed at 500 °C and (c) at 650 °C for 60 min. The thickness was 200 nm.

Table 4.3.1 Coercivity and squareness of 200 nm-thick FePt continuous films

Samples	Coercivity / kOe	Squareness
As-deposition	-	-
500 °C	6.0	0.65
650 °C	13.3	0.93

From the above characterizations of continuous films, phase transformation and magnetic hardening were successfully demonstrated. In BPM, magnetic layer with thickness less than 20 nm is required for the application, thus FePt continuous films with small thickness (< 40 nm) were deposited by reducing the deposition durations and were analyzed. Figure 4.3.5 shows the XRD patterns of annealed FePt continuous films with different thickness at 650 °C for 60 min. Because the peak intensity was insufficient to obtain by the out-of-plane method due to the small thickness, the films were measured with the grazing incidence angle of 0.4 °. The (111) peak of fcc disordered structure was observed in 30 nm-thick as-deposited film; upon annealing, phase transformation was confirmed from the appearance of the peaks corresponding to $L1_0$ ordered structure in both 10 nm and 30 nm-thick films. The hcp (002) of Ru substrate only appeared in 10 nm-thick FePt film owing to its small thickness. Fig.4.3.6 shows the out-of-plane hysteresis loops of FePt continuous films with different thickness after annealing at 650 °C for 60 min; measured coercivity and squarenss were summarized in table 4.3.2.

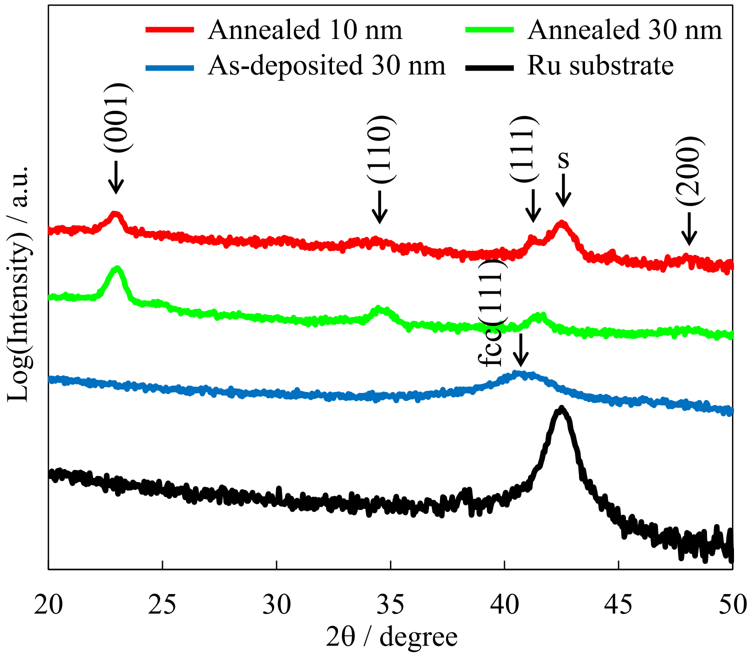

Fig. 4.3.5 XRD patterns of annealed FePt continuous films with different thickness. The grazing incidence angle was 0.4 º.

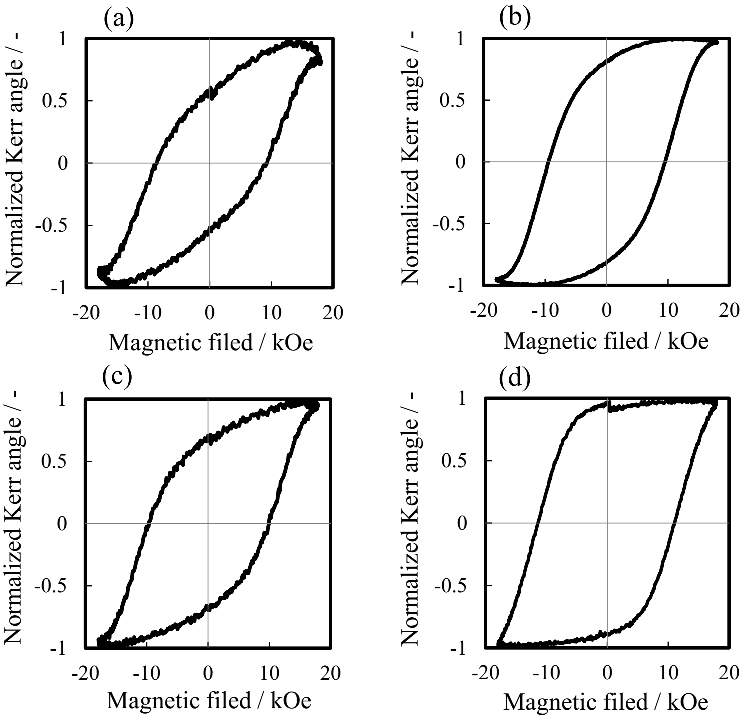

Fig. 4.3.6 Out-of-plane hysteresis loops of FePt continuous films with (a) 10 nm, (b) 20 nm, (c) 30 nm, and (d) 40 nm thickness after annealing at 650 ºC for 60 min.

Table 4.3.2 Coercivity and squareness of FePt continuous films with different thickness

Thickness / nm	Coercivity / kOe	Squareness
10	9.0	0.57
20	9.6	0.82
30	9.8	0.71
40	11.3	0.95

Magnetic hardening was clearly observed in each film due to the phase transformation of the films. The coercivity and squareness of the deposited films increased with increasing the thickness of the films, which is attributed to the increase in the magnetic domain size associating with the growth of the grain size of the film. The higher values of coercivity were obtained compared to that of the CoPt continuous films as confirmed in the chapter 2; 9.0 kOe was obtained even with the thickness of 10 nm. These features of crystal structures and magnetic properties of the continuous films should also be reflected in the nanodot arrays to exhibit high coercivity with $L1_0$ ordered structure.

4.3.2 Fabrication of $L1_0$-FePt Nanodot Arrays with Tbit/in^2 Areal Density

In order to apply FePt alloy for the fabrication of nanodot arrays with Tbit/in^2 recording density, FePt was deposited into the nanopore patterned substrate with 35 nm in pitch fabricated by electron beam lithography in the same bath summarized in table 4.2.1. The fabrication of FePt nanodot arrays was conducted in the same procedures as fabrication of CoPt nanodot arrays (see Fig.2.2.1). However, as shown in Fig. 4.3.7 (a), geometry of ordered nanodot arrays was degraded after electrodeposition. Although the exact reason for this degradation is not understood, one possibility is the high bath temperature for the FePt deposition. Because the glass transition temperature of the electron beam resist (ZEP520A-7) is 105 °C, the high bath temperature of 75 °C may deteriorate the nanopores to inhibit the nucleation of FePt inside the nanopores. Baumgartner et al. reported that the current efficiency decreases below 60 °C; considering this point, the bath temperature was lowered to 60 °C to mitigate the deterioration of nanopores. Figure 4.3.7 (b) shows the linear sweep voltammograms of FePt electrolyte with 75 °C and 60 °C; scan rate was 50 mV s^{-1}. At lower bath temperature, the current onset and the reduction of each metal shifted to 0.11 V more negative potential, which was in accordance with the Nernst equation. Although the shift in the reduction of each metal changes the alloy composition, near-equiatomic composition of FePt was obtained at 60 °C with -1.15 V (vs. Ag/AgCl).

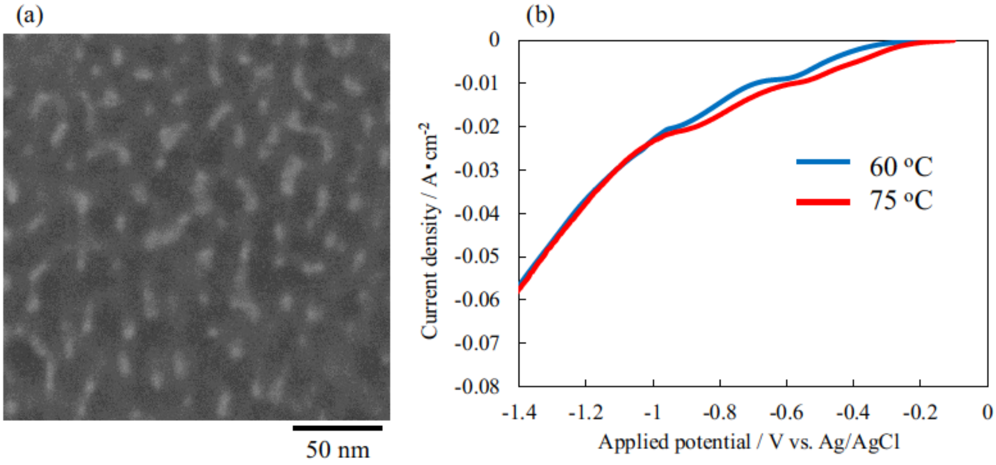

Fig. 4.3.7 (a) SEM images of FePt nanodot arrays deposited in bath temperature of 75 °C. (b) Linear sweep voltammograms of FePt electrolyte with 75 °C and 60 °C.

FePt was deposited with -1.15 V (vs. Ag/AgCl) for 15 s at 60 ^{o}C inside the nanopore patterned substrate with 35 nm in pitch and 15 nm in diameter to fabricate nanodot arrays; SEM image of nanodot arrays is shown in Fig. 4.3.8 (a). From the SEM image, the deposition of FePt was confirmed over the patterned area, however, FePt grew to form nanodots in non-uniform shapes consisting of several fine grains. This inhomogeneous growth of FePt could attribute to multiple nucleation along with the hydrogen evolution, which took place at the potential where Fe reduction occurs. As the growth of FePt proceeded, hydrogen evolution could also be enhanced due to the catalytic activity of the Pt on the surface to inhibit the nucleation of FePt, resulting in the non-uniform morphology in each nanodot. The inhomogeneous morphology of nanodots results in lack of uniformity in coercivity of each nanodot. In addition, nanodot arrays consisting of fine FePt grains could exhibit not only multiple magnetic domain structure but also superparamagnetic feature. Thus, in order to suppress the hydrogen evolution and to enhance the growth of FePt, FePt was deposited inside the nanopore with less negative potential of -1.0 V (vs. Ag/AgCl). Figures 4.3.8 (b) and (c) shows the SEM image of FePt nanodot arrays with 35 nm and 25 nm in pitch deposited with -1.0 V (vs. Ag/AgCl) at 60 ^{o}C for 20.5 s and 6.0 s, respectively. From the top images of nanodot arrays, FePt was uniformly nucleated inside the nanopore over the patterned area to form FePt nanodot arrays at less negative potentials; the inhomogeneous morphology was prevented by applying less negative potential to mitigate the hydrogen evolution and multiple nucleation. At higher recording density of 25 nm in pitch, corresponding to 1 Tbit/in^2, although some defects were observed due to the non-uniform patterning at this ultra-high density, fabrication of FePt nanodot arrays with Tbit/in^2 were successfully demonstrated.

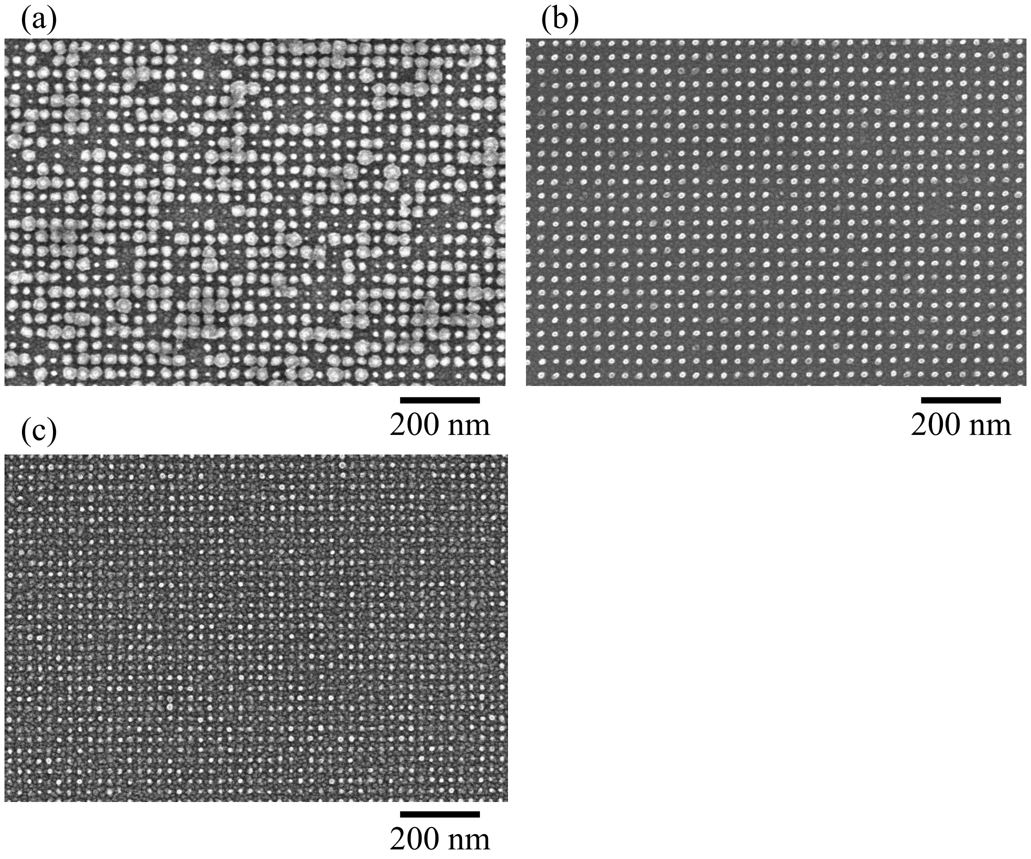

Fig. 4.3.8 SEM images of FePt nanodot arrays with 35 nm in pitch deposited with (a) -1.15 V for 15 s and with (b) -1.0 V for 20.5 s, and (c) nanodot arrays with 25 nm in pitch deposited with -1.0 V for 6.0 s.

Prior to the detailed analyses of FePt nanodot arrays, annealing conditions of ramp rate and holding time were optimized to fabricate uniform nanodot arrays with high areal recording density. Figure 4.3.9 shows SEM images of FePt nanodot arrays with 35 and 15 nm in pitch and diameter, respectively. Figures 4.3.9 (a) and (b) compares the top view of FePt nanodot arrays before and after annealing at 650 ^{o}C for 60 min with the ramp rate of 130 ^{o}C/min. In the as-deposited conditions, nanodot arrays were uniform over the patterned area [Fig. 4.3.9 (a)]; however, after annealing for 60 min at 650 ^{o}C major deterioration of nanodot arrays was observed [Fig. 4.3.9 (b)]. Because the longer holding time may accelerate the diffusion of Fe and Pt atoms on the surface and into Ru substrate and possibly the aggregation of nanodots, the nanodot array geometry suffered degradation after the annealing. In order to achieve uniform nanodot arrays, a reduction in the total time of the annealing process was attempted by increasing the ramp rate and reducing the holding time. Figures 4.3.9 (c) and (d) show SEM images of FePt nanodot arrays annealed at 650 °C for 0 min with 1300 °C/min and 1950 °C/min, respectively. As the ramp rate increased the deterioration of nanodot arrays was mitigated after annealing, and at 1950 °C/min uniformity of as-deposited nanodot arrays was successfully maintained after the annealing. Thus, in the present work, fabrication of FePt nanodot arrays was carried out by annealing at 650 °C for 0 min with 1950 °C /min.

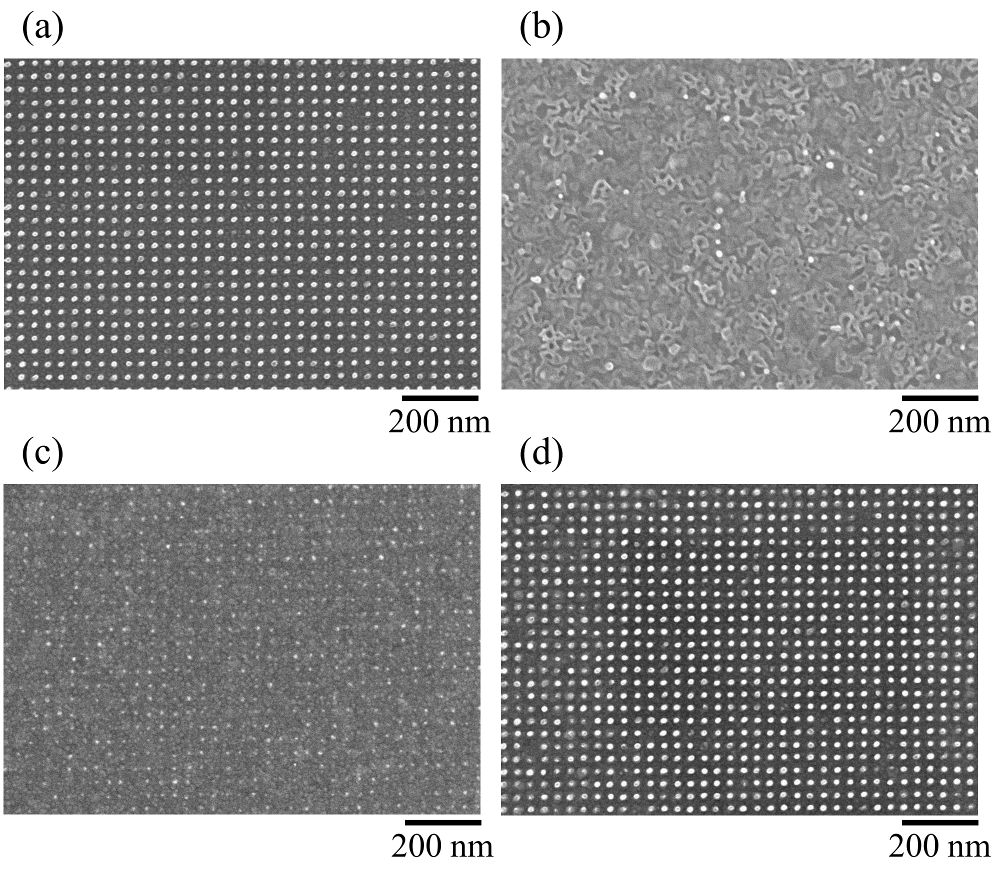

Fig. 4.3.9 SEM images of FePt nanodot arrays with 35 nm in pitch (a) as-deposited stage and annealed at 650 °C for (b) 60 min with 130 °C /min, (c) for 0 min with 1300 °C/min, and (d) for 0 min with 1950 °C/min.

In order to investigate the phase transformation of FePt nanodot arrays, lattice structure of nanodots with 35 nm in pitch were observed using TEM. Figure 4.3.10 shows the cross-sectional TEM images of the as-deposited FePt nanodot arrays deposited at -1.0 V (vs. Ag/AgCl) for 20.5 s. The insets show the selected area electron diffraction (SAED) patterns of nanodot. From the lower magnification TEM image [Fig. 4.3.10 (a)], uniform fabrication of nanodot arrays with a columnar shape without voids was confirmed. In addition, SAED patterns of as-deposited nanodots showed ring-like patterns, which indicates that the deposited nanodot arrays exhibit polycrystalline structure due to the multiple nucleation inside the nanopore under this deposition condition. Higher magnification image [Fig. 4.3.10 (b)] showed grain boundaries of FePt particles and random crystal orientations due to the multiple nucleation of FePt, resulting in the polycrystalline structure as observed in the SAED patterns.

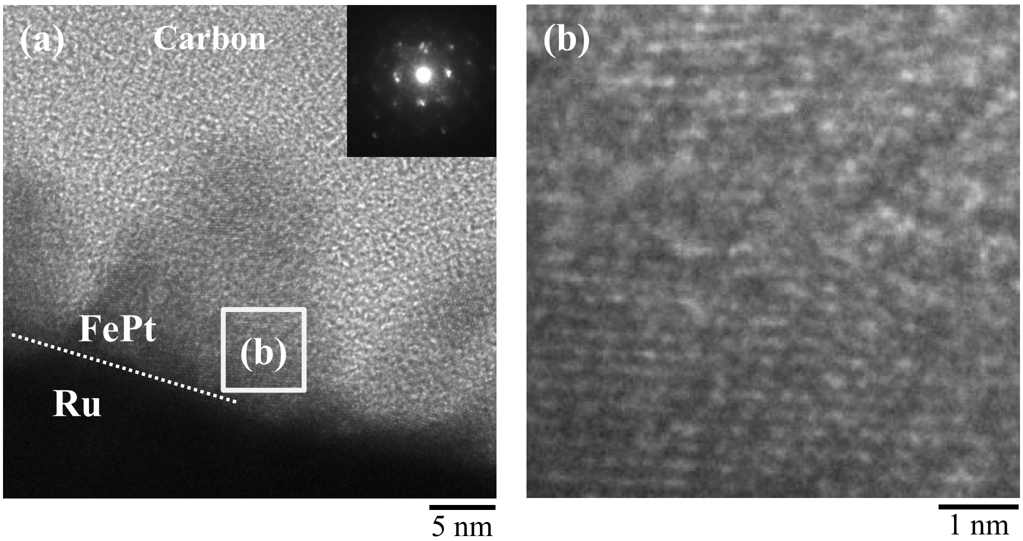

Fig. 4.3.10 Cross-sectional TEM images of FePt nanodot arrays deposited at -1.0 V for 20.5 s. (a) Low magnification and (b) high magnification image of nanodots. The inset shows the selected area electron diffraction (SAED) patterns of nanodots.

Figure 4.3.11 shows the cross-sectional TEM images of annealed FePt nanodot arrays at 650 ^{o}C for 0 min with ramp rate of 1950 ^{o}C/min. Lower magnification image confirmed that columnar shape was maintained after annealing. The slight difference in the shape of the nanodots compared to that of the as-deposited ones should be mainly attributed to the rearrangement of Fe and Pt atoms in the ordered structure, and the decrease in height of the nanodot could be due to the interdiffusion of Fe and Pt atoms into the Ru substrate. From the higher magnification TEM images of the nanodot, it was found that grain boundaries and random crystal orientation, which were observed in the as-deposited nanodot, vanished to form a clear stacking of crystal facets oriented in the perpendicular direction from the initial deposition stage. The SAED patterns of the nanodot showed diffraction spots and a small amount of diffraction rings in the patterns, indicating that the nanodot arrays were polycrystalline structure. In addition, the measured d-spacing was 0.231 nm, which was slightly larger than the d_{111} plane spacing of $L1_0$ ordered structure (0.219 nm). Although the morphology of nanodots was maintained after the annealing, it was suggested that the phase transformation from fcc disordered structure to L10 ordered structure was incomplete under this annealing conditions. Thus, in order to achieve fabrication of Tbit/in^2 nanodot arrays with $L1_0$ structure $L1_0$ ordering should be enhanced.

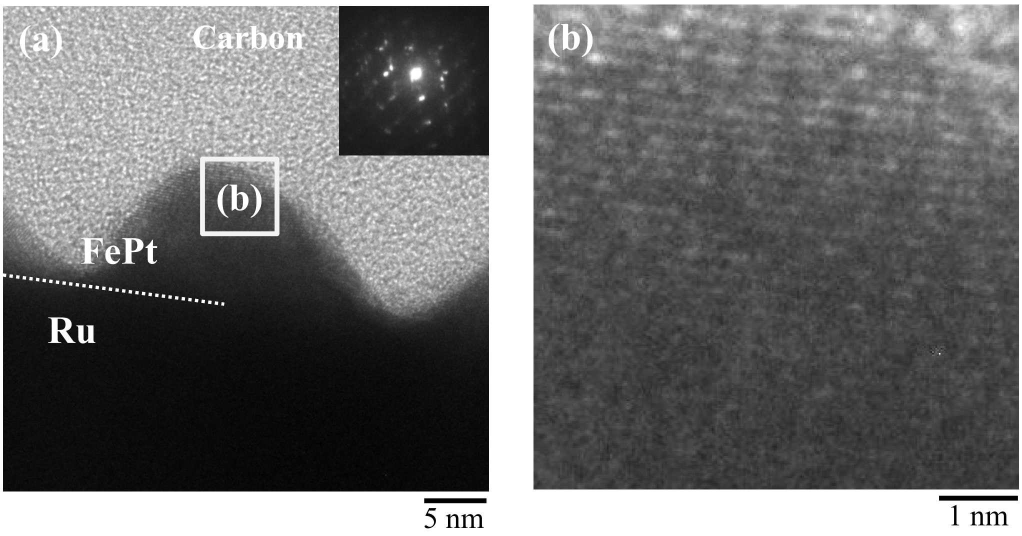

Fig. 4.3.11 Cross-sectional TEM images of annealed FePt nanodot arrays deposited at -1.0 V for 20.5 s. The nanodots were annealed at 650 ^{o}C for 0 min with ramp rate of 1950 ^{o}C/min. (a) Low and (b) high magnification image of nanodots. The inset shows the selected area electron diffraction (SAED) patterns of nanodots.

Conclusion

Feasibility of the electrodeposition process as a fabrication process of FePt nanodot arrays was evaluated. Electrodeposited FePt films showed higher coercivity of 9.0 and 13.3 kOe for 10 and 200 nm-thick films, respectively, which were two times higher than electrodeposited CoPt films. FePt deposition demonstrated fabrication of nanodot arrays with 25 nm in pitch, which corresponds to 1.0 Tbit/in^2 areal density, and the optimization of the annealing conditions, such as ramp rate and holding time, led to successful formation of FePt nanodot arrays after annealing at high temperature of 650 ^{o}C. By developing the deposition conditions to satisfy the requirement of the enhancement of $L1_0$-ordering of FePt, electrodeposition process should be a promising candidate for the fabrication of nanodot arrays consist of high K_u materials.

References

[1] D. Weller, A. Moser, L. Folks, M. E. Best, W. Lee, M. F. Toney, M. Schwickert, J. U. Thiele, and M. F. Doerner, *IEEE Trans. Magn.*, 36 (2000) 10.

[2] R. A. Ristau, K. Barmak, L. H. Lewis, K. R. Coffey, and J. K. Howard, *J. Appl. Phys.*, 86 (1999) 4527.

[3] D. Weller, O. Mosendz, G. Parker, S. Pisana, and T. S. Santos, *Phys. Status Solidi A*, 210 (2013) 1245.

[4] M.H. Kryder, E.C. Gage, T.W. McDaniel, W.A. Challener, R.E. Rottmayer, G. Ju, Y-T. Hsia, and F. Erden, *Proc. IEEE*, 96 (2008) 1810.

[5] Q. Dong, G. Li, C.-L. Ho, M. Faisal, C.-W. Leung, P. W.-T. Pong, K. Liu, B.-Z. Tang, I. Manners, and W.-Y. Wong, *Adv. Mater.*, 24 (2012) 1034.

[6] A. Kikitsu, T. Maeda, H. Hieda, R. Yamamoto, N. Kihara, and Y. Kamata, *IEEE Trans. Magn.*,49 (2013) 693.

[7] T. R. Albercht, H. Arora, V. A.-Vitikkate, J.-M. Beaujour, D. Bedau, D. Berman, A. L. Bogdanov, Y.-A. Chapuis, J. Cushen, E. E. Dobisz, G. Doerk, H. Gao, M. Grobis, B. Gurney, W. Hanson, O. Hellwig, T. Hirano, P.-O. Jubert, D. Kercher, J. Lille, Z. Liu, C. M. Mate, Y. Obukhov, K. C. Patel, K. Rubin, R. Ruiz, M. Schabes, L. Wan, D. Weller, T.-W. Wu, and E. Yang, *IEEE Trans. Magn.*, 51 (2015) 1.

[8] Y. Shiroishi, K. Fukud, I. Tagawa, H. Iwasaki, S. Takenoiri, H. Tanaka, H. Mutoh, and N. Yoshikawa, *IEEE Trans. Magn.*, 45 (2009) 3816.

[9] K. Leistner, E. Backen, B. Schupp, M. Weisheit, L. Schultz, H. Schlorb, and S. Fahler, *J. Appl. Phys.*, 95 (2004) 7267.

[10] J.J. Mallett, E.B. Svedberg, S. Sayan, A.J. Shapiro, L. Wielunski, T.E. Madey,W.F. Egelhoff, and T.P. Moffata, *Electrochem. Solid-State Lett.*, 7 (2004) C121.

[11] D. Liang, J. J. Mallett, and G. Zangari, *J. Electrochem. Soc.*, 158 (2011) D149.

[12] D. Liang, J. J. Mallett, and G. Zangari, *ACS Appl. Mater. Interfaces*, 2 (2010) 961.

[13] D. Liang, J. J. Mallett, and G. Zangari, *Electrochim. Acta*, 55 (2010) 8100.

Chapter 5

Fabrication of Multilayered FePt and FePtCu Nanodot Arrays towards $L1_0$ Ordering

5.1 Introduction

Several approaches have been proposed to accelerate the $L1_0$ ordering process of FePt in the physical deposition methods, for example, fabrication of multilayered Fe/Pt film [1-3] or addition of Cu as a third element to form ternary FePtCu alloy [4, 5]. Previous studies of fabrication of multilayered Fe/Pt films have shown that multilayered structure was effective in reducing the ordering temperature due to its rapid diffusion at the Fe/Pt interface to form $L1_0$ FePt phase directly [3]. On the other hand, Maeda et al. reported that the addition of Cu into FePt alloy increases the free energies between the disordered and ordered FePtCu ternary alloy compared to that of the FePt binary alloy, which increases the driving force of phase transformation at lower annealing temperature [4].

Fe/Pt multilayer films consisting of Fe- and Pt-rich layer were first studied to reduce the oxygen contents in the electrodeposited films. Leistner et al. reduced the oxygen content in the as-deposited films by depositing Fe/Pt multilayer by pulse electrodeposition [6]; bilayer thickness down to 40 nm thick with Fe/Pt ratio of 1.0 was reported. Post annealing of this films in hydrogen atmosphere at 600 °C and 400 °C led to the formation of the $L1_0$ FePt phase and films with coercivity of 10 kOe and 6.2 kOe were achieved, respectively. However, the total thickness of the film was more than 1.0 μm, which was too thick for the application in magnetic recording media; thickness of less than 20 nm is required in the magnetic recording media. Zangari et al. fabricated 25 nm-thick FePt films by coupling Fe-rich layers with Pt 25 at% to accelerate the ordering of FePt [7]. The coercivity of FePt/Fe-rich bilayers (FePt 15 nm/ Fe-rich 10 nm) after annealing at 550 °C showed 45 % higher coercivity of 6.0 kOe compared with a single layer of 15 nm equiatomic FePt; the increase in the coercivity was also observed in the trilayer and five-layer structures.

For the electrodeposition of FePtCu ternary alloy, Thongmee et al. deposited 2 at.% Cu doped FePt films with a thickness of 800 nm on the Cu underlayer. Upon annealing at 350 °C, $L1_0$ ordered FePt was formed and the annealed film showed coercivity of 12 kOe [8]. In this film, diffusion of doped Cu may form channels in FePt films, which act not only as a formation of columnar structures in FePt films but also as a channels to facilitate further Cu diffusion from the underlayer. The columnar shape of the film induces the perpendicular magnetic anisotropy and diffusion of Cu into the film enhances the mobility of Fe and Pt, resulting in the increase in coercivity with lower annealing temperature. Svedberg et al. also utilized (001) oriented Cu underlayer to accelerate the phase transformation of FePt with (001) orientation [9]. By annealing the FePt films deposited on the Cu (001) underlayer, recrystallization of FePt stars at the FePt/Cu interface due to the interdiffuion of Cu into FePt, thus keeping the initial crystal orientation of Cu (001) underlayer through the deposited films; the $L1_0$ ordering of 360 nm-thick film was achieved at 450 ^{o}C and further annealing at 650 ^{o}C high perpendicular coercivity, of up to 10 kOe, was obtained.

Despite many studies on physically prepared FePt multilayers or FePtCu ternary alloy in the BPM system, there is no report of electrodeposited FePt multilayer or FePtCu ternary alloy for the application in ultra-fine nanostructures, which are suitable for the BPM application. From the previous studies of electrodeposited multilayer structure or the ternary alloy structure demonstrated the facilitation of FePt to $L1_0$ structure. Therefore, in this chapter, $L1_0$-FePt nanodot arrays with Tbit-level recording density were fabricated by applying multilayer structure or Cu addition to accelerate the ordering process of FePt under lower annealing temperature or heating time requirements. The acceleration of ordering process in nanodot arrays with multilayer and Cu addition was investigated by detailed crystal structure characterization.

5.2 Experimental

5.2.1 Fabrication of FePt Multilayers

FePt continuous films and nanodot arrays were electrodeposited from an electrolyte summarized in Table 5.2.1, which is the same bath composition as described in chapter 4. Multilayer structure was consisted of Fe- and Pt-rich layer with various thickness, which were deposited by changing the applied potential and deposition duration for each layer. Potentiostat (HZ-7000, Hokuto Denko) was utilized for all the electrochemical measurements; a Pt mesh and Ag/AgCl electrode were used as counter electrode and reference electrode, respectively. FePt alloy was deposited onto a 60 nm-thick Ru underlayer with 5 nm-thick Ti adhesion layer sputter deposited on n-Si (100) wafer. Post annealing for the phase transformation to $L1_0$ ordered structure was performed utilizing rapid thermal annealing device under forming gas (90 % Ar + 10 % H_2); samples were heated up to 450 and 650 ^{o}C with different holding times and ramp rates, and cooled down to room temperature. The annealing conditions are summarized in table 5.2.2.

The nanopore patterned substrate was formed onto Ru substrate by utilizing electron beam lithography (ELS-7500, ELIONIX) in the same process as described in the previous chapters; conditions of the electron beam lithography is shown in table 5.2.3. Morphology of FePt nanodot arrays were observed by high-resolution scanning electron microscope (HR-SEM, S5500, Hitachi High-Tech.). Crystal structure of continuous films was analyzed by X-ray diffractometer (XRD, Rint-Ultima III, Rigaku) with grazing incidence angle of 0.4 ^{o}, and structural analysis of nanodot arrays was performed by transmission electron microscope (TEM, JEM-2010, JEOL). Alloy composition of FePt continuous films and nandot arrays was determined by inductively-coupled plasma mass spectrometry (ICP-MS, 7700x, Agilent); 10 ppb of Rh was used as an internal standard. Magnetic properties of deposited continuous films were characterized by magneto-optical Kerr effect equipment (BH-810PC-WU, NEOARK); the diameter of the laser spot area was 1.0 mm. Prior to the characterization of the nanodot arrays all the resist was removed by exposing the samples with excimer UV irradiation for 2.0 min and rising with ethanol and UPW.

Table 5.2.1 Bath compositions and electrodeposition conditions of FePt

Chemicals	Concentration / mM
$(NH_4)_2C_6H_6O_7$	150
$Fe_2(SO_4)_3$	50
NH_2CH_2COOH	150
$NaNO_2$	100
$(NH_4)_2SO_4$	100
$Pt(NO_2)_2(NH_3)_2$	15
Bath temperature	75 °C
pH	8 (adjusted by KOH)
Reference electrode	Ag / AgCl
Counter electrode	Pt mesh

Table 5.2.2 Annealing conditions

Atmosphere	$Ar+H_2$ 10 %
Annealing temperature	450, 650 °C
Ramp rate	130, 1950 °C/min
Holding time	0 min
Cooling	Water

Table 5.2.3 Operating conditions of electron beam lithography

Resist	ZEP520A-7 : ZEP-A = 1:2
Spin Coat	5000 rpm, 60 s
Prebake	180 °C, 3 min
Thickness of resist	30 nm
Accelerating voltage	50 kV
Beam current	20 pA
Dose value	10 fC / dot
Developer	IPA
Developing time	5 s
Developing temperature	5 °C
Rinse	UPW

5.2.2 *Electrodeposition of FePtCu Ternary Alloy*

For the electrodeposition of FePtCu ternary alloy, $CuSO_4$ was added as a precursor of Cu into the FePt electrolyte; the bath conditions are summarized in table 5.2.3. FePtCu was deposited onto (002) oriented 60 nm-thick Ru and 5 nm-thick Ti adhesion layer sputter deposited on the n-Si (100) substrate. All the electrochemical measurements were performed by using potentiostat (HZ-7000, Hokuto Denko). FePtCu nanodot arryas were fabricated in the same procedure as described in the previous chapters; the lithography conditions are summarized in table 5.2.3. For the phase transformation of the FePtCu rapid thermal annealing device was utilized; samples were heated under forming gas (90 % Ar + 10 % H_2) at 450 and 650 ^{o}C with the conditions summarized in table 5.2.2. Alloy compositions of each metal element in deposited continuous films were analyzed by energy dispersive X-ray spectroscopy. X-ray diffractometer (XRD, Rint-Ultima III, Rigaku) was used to investigate the crystal structure of deposited continuous films with grazing incidence angle of 0.4 º. The morphology of the deposited continuous films and nanodot arrays were observed by HR-SEM (S5500, Hitachi High-Tech.). The coercivity of the deposited continuous films was measured by polar magneto-optical Kerr effect equipment (BH-810PC-WU, NEOARK).

Table 5.2.4 Bath compositions and electrodeposition conditions of FePt

Chemicals	Concentration / mM
$(NH_4)_2C_6H_6O_7$	150
$Fe_2(SO_4)_3$	50
NH_2CH_2COOH	150
$NaNO_2$	100
$(NH_4)_2SO_4$	100
$Pt(NO_2)_2(NH_3)_2$	15
$CuSO_4$	0.020-5.0
Bath temperature	75 ^{o}C
pH	8 (adjusted by KOH)
Reference electrode	Ag / AgCl
Counter electrode	Pt mesh

5.3 $L1_0$ Ordering of FePt Nanodot Arrays with Multilayer Structure

5.3.1 Facilitation of $L1_0$ Ordering of FePt by Multilayer Strcuture

In order to fabricate FePt films with equiatomic or Fe- and Pt- rich composition, the composition of FePt films deposited on Ru substrate was optimized by adjusting the applied potential. At the applied potential of -1.0 V vs. Ag/AgCl, near-equiatomic FePt films were obtained; for the deposition of Fe-rich and Pt-rich layers instead -1.4 and -0.8 V vs. Ag/AgCl were selected, such that the Fe fraction in the films was 80 at.% and 20 at.%, respectively. The multilayer structure of twenty-, eight-, and four-layers, where the thickness of each layer was set to around 1.0, 2.5, and 5.0 nm, was deposited by changing the deposition duration: 120, 360, and 660 s for the Pt-rich layer and 0.50, 1.5, and 2.75 s for the Fe-rich layer, respectively. The number of layers was set by changing the number of potential cycles. In this chapter, the phase transformation and magnetic properties of 20 nm-thick blanket multilayer films is discussed in detail; subsequently, the fabrication of $L1_0$ nanodot arrays was attempted.

Table 5.3.1 shows the alloy composition of 20 nm-thick multilayer FePt films deposited with different number of Fe- and Pt-rich layers. All samples showed a composition near to equiatomic in each deposition condition suggesting the uniform formation of Fe-rich and Pt-rich layers at different thickness. At the composition ratio summarized in Table 5.3.1, phase transformation of FePt alloy from fcc disordered structure to $L1_0$ ordered structure is expected.

Table 5.3.1 The alloy compositions of FePt continuous films

Numbers of layers	Alloy composition	
	Fe / at%	Pt / at%
20	57	43
8	59	41
4	58	42
1	55	45

Figure 5.3.1 compares the XRD patterns of the as-deposited 20 nm-thick FePt films made up of multi-layers and a single layer. The as-deposited FePt films deposited with both pulse and constant potential showed a peak at 40-41 ° indicating that FePt grew in a fcc structure with a (111) orientation; peak appeared at slightly lower angle in multilayer films.

Because multilayer consists of both Fe- and Pt-rich layers, the multilayer films showed broad peak with lower intensity of (111) peak compared to that of single layer. The Pt- and Fe-rich layer should exhibit fcc structure and bcc structure, respectively; the individual peaks for the Fe-rich of bcc (110) and Pt-rich of fcc (111) at 44 and 40 ° were observed in the multilayer structures [6].

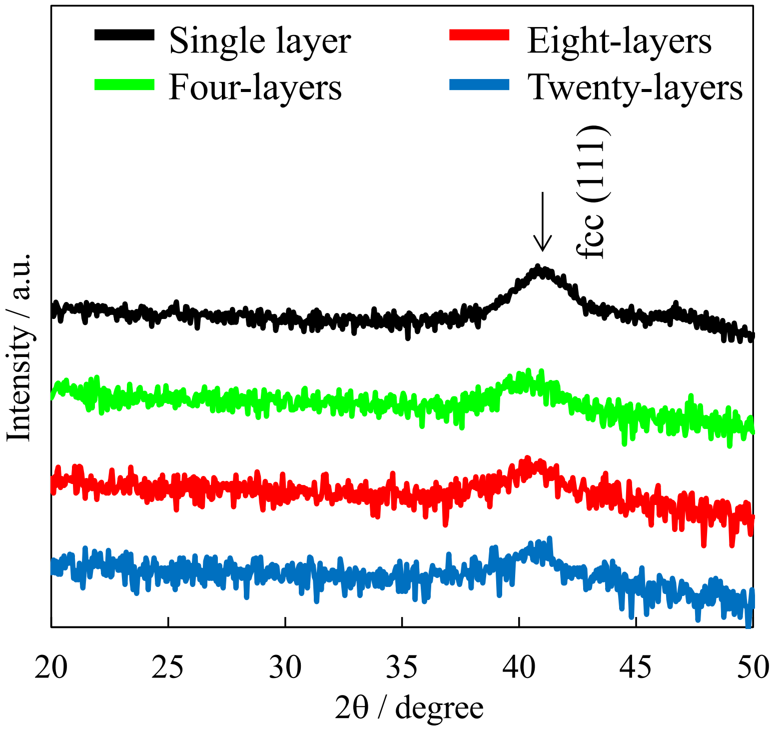

Fig. 5.3.1 XRD patterns of as-deposited 20 nm-thick FePt continuous films with single layer and multilayer structures.

To investigate the phase transformation of the deposited multilayer films and single layer of FePt film, which are the same samples described in Fig. 5.3.1, both sets were annealed at 450 °C for 60 min; corresponding XRD patterns are shown in Fig. 5.3.2. After the annealing process, all samples showed a sharp peak at 41.3° corresponding to the (111) reflection, which was shifted to a higher angle compared to the peak observed in the as-deposited films. In addition, additional peaks near 24° and 47°, which correspond to the (001) and (200) reflections of the $L1_0$ structure, were observed only in the multilayer with eight-layers, whereas other films did not show characteristic peaks of L10 structure, indicating that the phase transformation was incomplete for the single layer and other multilayer structures at the annealing temperature of 450 °C. With regard to the FePt films with twenty-layers, the thickness of each layer is 1.0 nm. Considering the short deposition duration at this condition, the Fe- and Pt-rich layers may be partially discontinuous and the separation of each layer was probably insufficient to form a uniform multilayer structure, which suggests that the interdiffusion of Fe and Pt atoms during the thermal annealing may not have been sufficient to facilitate the phase transformation. Considering the interdiffusion process, as the thickness of each layer increases Fe- and Pt- rich layer should be uniformly separated to facilitate formation of the $L1_0$ structure at the interface. However, $L1_0$ ordering was not observed in the case of FePt films with four-layers, which could be due to the larger diffusion length of Fe and Pt atoms because the thickness of each layer is assumed to be 5.0 nm.

Figure 5.3.3 displays the XRD patterns of FePt films with eight-layers and a single layer after annealing at 650 °C for 0 min. Under this annealing condition, temperature was cooled down as it reached to 650 °C, thus the holding time for the samples is considered as 0 min. Both films showed a sharp peak of (111) and peaks of (001) and (200) as observed in the patterns of other samples (Fig. 5.3.2), which suggests the phase transformation of the films.

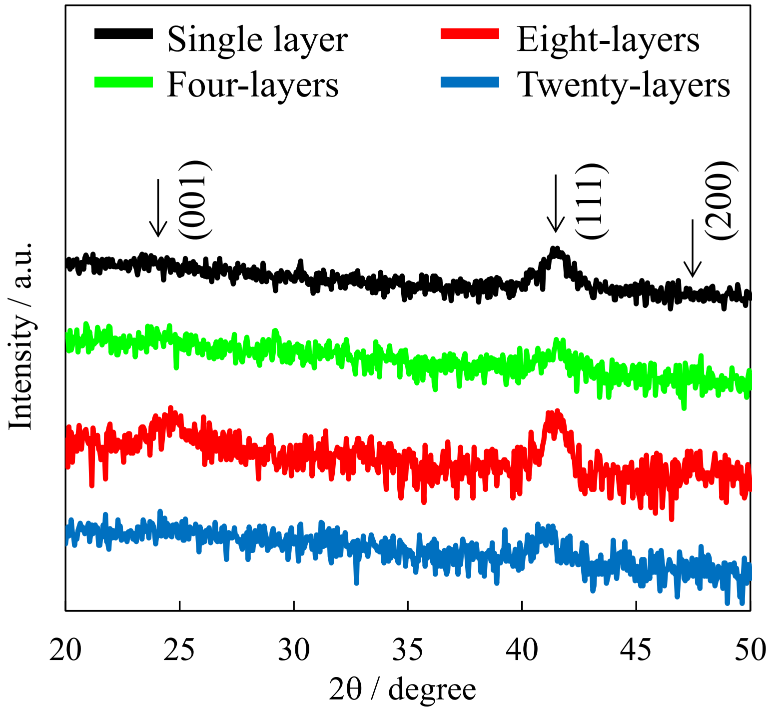

Fig. 5.3.2 XRD patterns of 20 nm-thick FePt continuous films with single layer and multilayer structure annealed at 450 ^{o}C for 60 min.

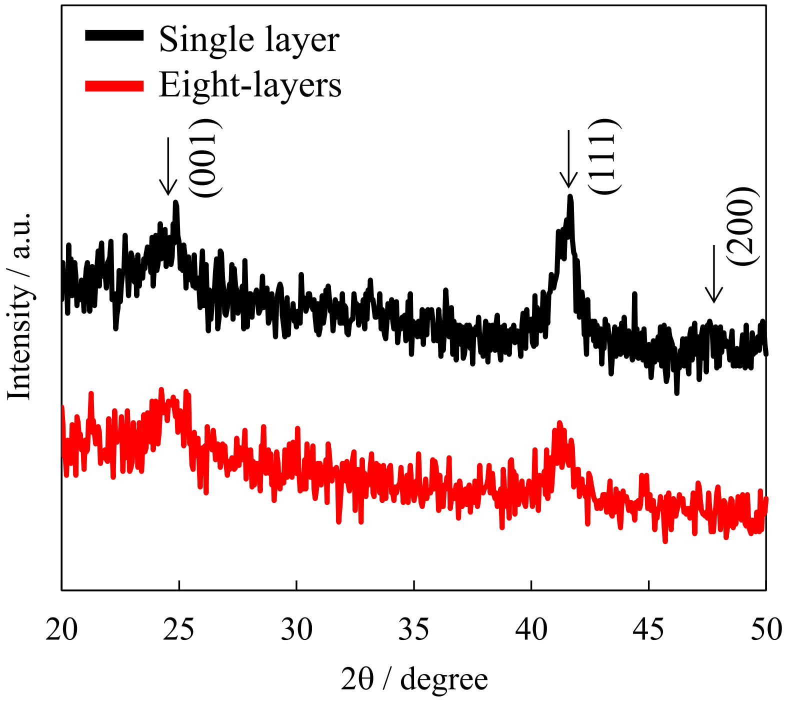

Fig. 5.3.4 XRD patterns of 20 nm-thick FePt continuous films with single layer and eight layer structure annealed at 650 ^{o}C for 0 min.

To further investigate the details of the phase transformation in these films, the ordering parameters, S, of the annealed films with single layer and wight-layers were calculated. S can be calculated from Eq. (5.3.1) by using the axial ratio of c and a axis of deposited films [4];

$$S^2 = \frac{1-(c/a)}{1-(c/a)_{S_f}} \tag{5.3.1}$$

where $(c/a)_{S_f}$ is the axial ratio for the fully ordered phase and (c/a) is the axial ratio of the annealed films. The values of a- and c- axis for the bulk $L1_0$ FePt are given by 3.852 and 3.713 Å [10], respectively, thus $(c/a)_{S_f}$ was estimated as 0.964. The axial ratios of the deposited films were determined by calculating the values of the a- and c- axis from the (200) and (001) XRD peaks, respectively. The lattice parameters and the ordering parameters of each film with different number of the layers are plotted in Fig. 5.3.4. Upon annealing at 450 °C, the eight-layer film showed ordering parameter of 0.82. In addition, at higher annealing temperature, eight-layer film showed decrease in c-lattice parameter compared to that of single layer, and the ordering parameters were enhanced up to 0.86 and 0.94 for the single and eight-layer films, respectively. These features observed in the diffraction patterns of the FePt multilayer films should reflect on the coercivity of FePt. To investigate this point, the coercivity of multilayer and single layer of FePt films was measured after the annealing.

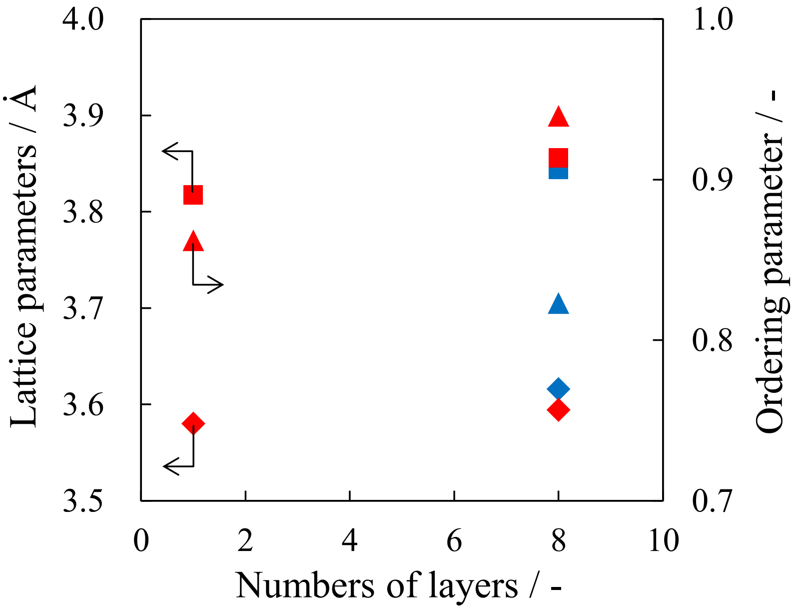

Fig. 5.3.4 The lattice parameters and the ordering parameters of 20 nm thick FePt continuous films with single layer and multilayer structures. The blue diamond, square, and triangle are c-, a-axis, and ordering parameters at 450 °C, and those in red color are at 650 °C.

Figures 5.3.5 (a) and (b) show the out-of-plane magnetic hysteresis loops for the same samples as shown in Figs. 5.3.2 and 5.3.3, which were measured by polar magneto-optical Kerr effect equipment. At 450 °C magnetic hardening was not observed for the single layer FePt film; this sample showed a perpendicular coercivity of 1.0 kOe and squareness of 0.11. On the other hand, although the coercivity and squareness increased slightly in the multilayer films with twenty- and four-layers, the FePt film with eight-layers showed significant magnetic hardening, leading to an increase in coercivity and squareness up to 6.6 kOe and 0.57, respectively. At 650 °C the magnetic hardening was clearly observed and the coercivity of single layer and eight-layers increased up to 4.8 and 7.5 kOe due to the higher degree of phase transformation to $L1_0$ structure. Higher coercivity can be obtained by increasing the holding time for 60 min at 650 °C, resulting in values such as 9.0 kOe and 12.3 kOe for a single layer and multilayer FePt films, respectively (data not shown). The measured coercivity and squareness are summarized in Fig. 5.3.6. These values are in good agreement with those of the ordering parameters as summarized in Fig. 5.3.4; in particular, the increase in coercivity and squareness of the eight-layers FePt film was attributed to the higher value of ordering parameter.

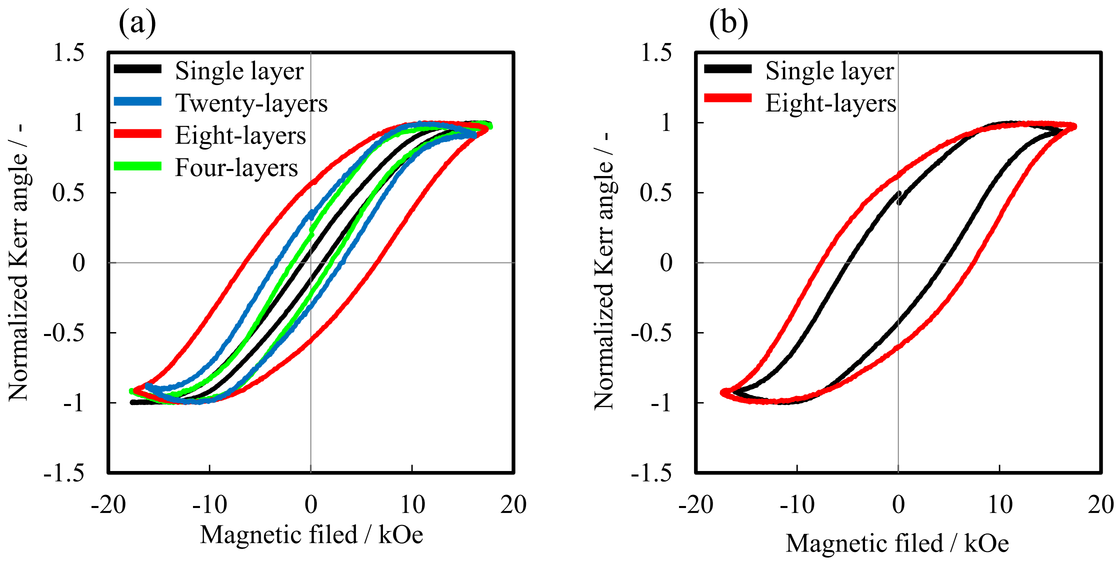

Fig. 5.3.5 Out-of-plane hysteresis loops of 20 nm-thick FePt continuous films with (a) single layer and multilayer structure annealed at 450 °C for 60 min and (b) single layer and eight-layer structure annealed at 650 °C for 0 min.

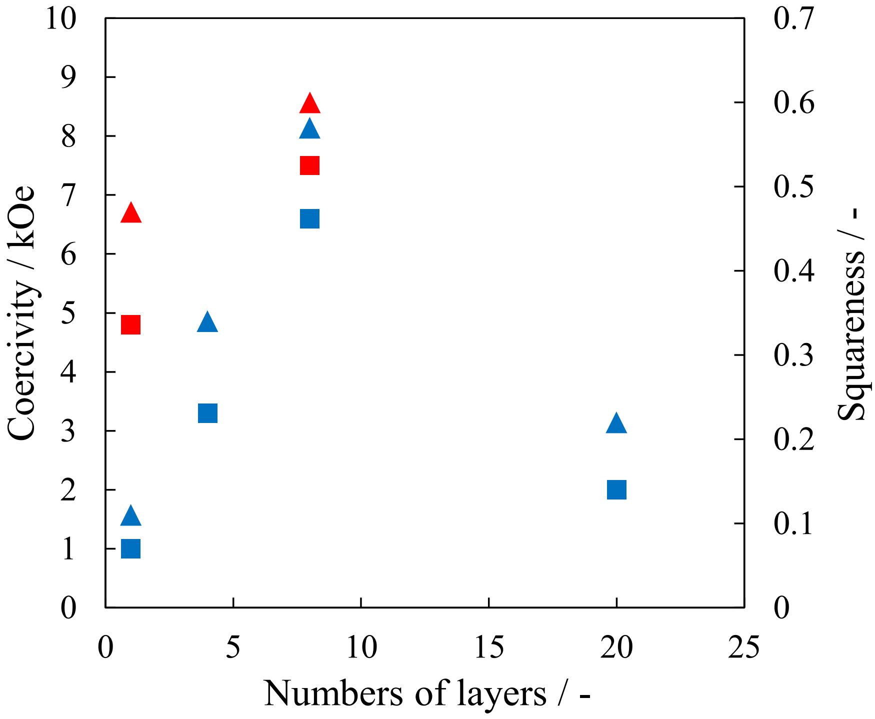

Fig. 5.3.6 The coercivity and squareness of 20 nm-thick FePt continuous films with single layer and multilayer structure. The blue square and triangle are coercivity and squareness at 450 °C, and those in red color are at 650 °C.

5.3.2 Fabrication of FePt Nanodot Arrays with Multilayer Structure

As described in chapter 4, annealing conditions of ramp rate and holding time significantly affect the nanodot arrays geometry; lower ramp rate and longer holding time accelerate the diffusion of Fe and Pt atoms on the surface and into the Ru underlayer, and the aggregation of nanodots. Therefore, nanodot arrays were annealed at 650 ^{o}C for 0 min with ramp rate of 1950 ^{o}C/min.

Figure 5.3.7 shows SEM images of eight-layer FePt nanodot arrays with 35 nm in pitch before and after annealing at 650 ^{o}C for 0 min with 1950 ^{o}C /min. Based on the characterization of the continuous films, the effects of multilayer structure should also be reflected in the formation of the FePt nanodot arrays. The eight-layer structure was chosen based on the strong improvement of magnetic properties and ordering behavior observed for continuous films. In the as-deposited state nanodot arrays with multilayer structure were uniformly fabricated over the patterned area, and although the diameter of the nanodot slightly decreased due to the diffusion of a small amount of Fe and Pt atoms into the Ru substrate caused by the thermal annealing, the nanodot geometry was uniformly maintained after the annealing process. From the analysis on the crystal structure of continuous films, significant enhancement of the phase transformation was confirmed with multilayer structure; thus, to investigate the difference in crystal structure of nanodot arrays obtained by single- and multi-layer deposits, the lattice structure of the FePt nanodot arrays with 35 nm in pitch were observed using TEM.

Figure 5.3.8 shows the cross-sectional TEM images of the as-deposited FePt nanodot arrays with eight-layer structure. The inset shows the selected area electron diffraction (SAED) patterns of nanodot. In the as-deposited condition, nanodot showed several grain boundaries with random crystal orientation; SAED patterns showed ring-like patterns indicating the polycrystalline structure of the nanodots due to the multiple-nucleation inside the nanopore as observed in the nanodot arrays with single layer structure in Fig. 4.3.10. In the eight-layer nanodot arrays a layered structure was expected from the cross-sectional image, however, it was hardly observed since the thickness of each layer is very thin and both layers should show the composition gradient at the initial deposition stage, which makes it difficult to observe the interfaces between each layer.

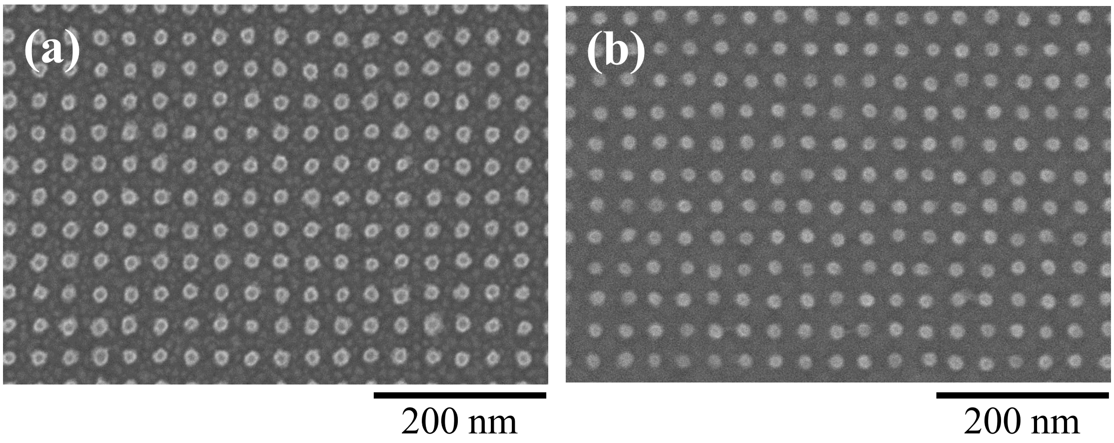

Fig. 5.3.7 SEM images of eight-layer FePt nanodot arrays with 35 nm in pitch (a) as-deposited stage and (b) annealed at 650 °C for 0 min with 1950 °C/min.

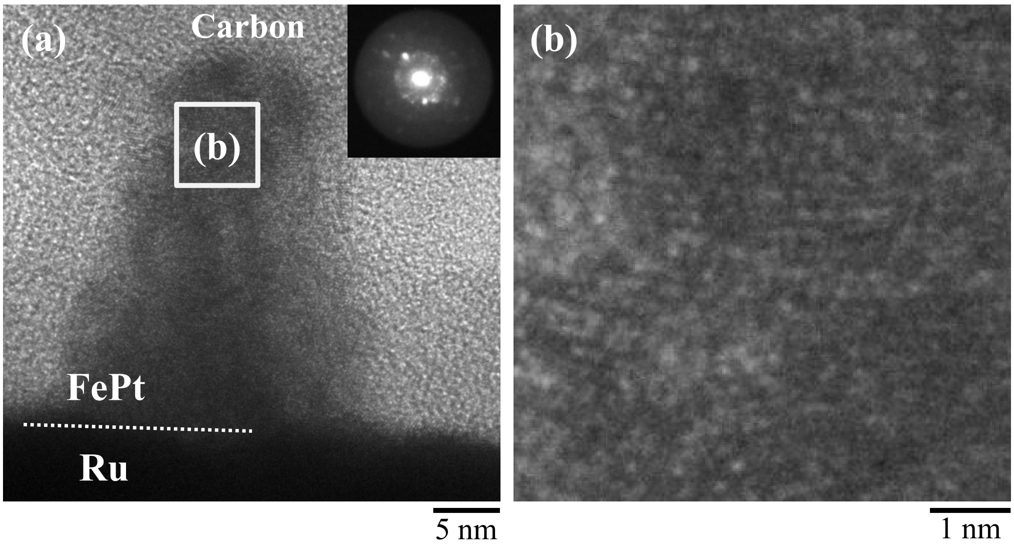

Fig. 5.3.8 Cross-sectional TEM images of as-deposited FePt nanodot arrays 35 nm in pitch consists of eight-layers structure. (a) Low and (b) high magnification. The insets show the SAED patternd of nanodot.

Figure 5.3.9 shows the cross-sectional TEM images of FePt nanodot arrays with the same geometry as shown in Fig. 5.3.8 after annealing at 650 °C for 0 min with 1950 °C /min. Lower magnification TEM images confirmed that geometry of nanodot arrays was maintained after the annealing process [Fig. 5.3.9 (a)]. The height of the nanodots was reduced after the annealing due to the diffusion of Fe and Pt atoms on the surface and inside the Ru underlayer, which was observed in the decrease in the diameter of nanodots in Fig. 5.3.7. Higher magnification image showed clear crystal fringes of lattice in the perpendicular direction from the interface of Ru to the upper part of the nanodots. The lattice spacing measured in the TEM image of multilayer nanodots was 0.220 nm, which agrees with the d_{111} plane spacing of the $L1_0$ FePt (0.219 nm) [24] indicating the phase transformation of nanodot arrays in the $L1_0$ ordered structure. In addition, the SAED patterns (insets) showed clear diffraction spots in the SAED patterns along the growth direction, without any diffraction rings, indicating that the crystallinity of $L1_0$ structure was improved with multilayer structure to have a single crystal nature. Furthermore, its crystal lattice is uniformly oriented in the perpendicular direction, which is necessary to induce the perpendicular magnetic anisotropy of the nanodot arrays. Since the nanodots exhibit a (111) crystal orientation along the growth direction, probably due to the lattice matching between FePt and Ru underlayer, they should exhibit both in-plane and perpendicular magnetization components. This is not ideal for maximizing remanence, therefore in order to control the crystal orientation along the (001) direction, a substrate with lattice matching to the FePt (100) plane, such as TiN [11], can be employed to induce perpendicular magnetic anisotropy.

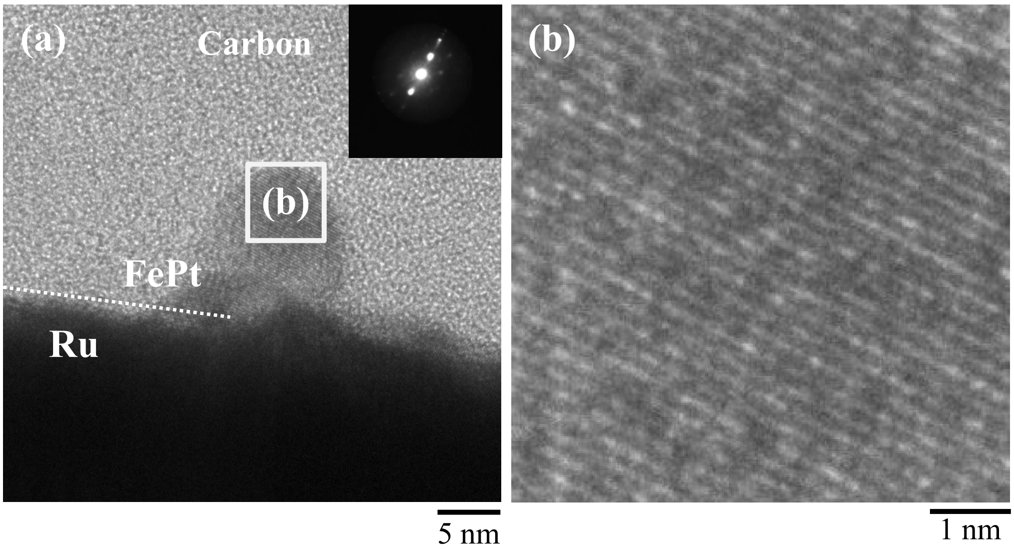

Fig. 5.3.9 Cross-sectional TEM images of annealed FePt nanodot arrays of eight-layer structure with 35 nm in pitch. The nanodots were annealed at 650 ^{o}C for 0 min with ramp rate of 1950 ^{o}C/min. (a) low and (b) high magnification images of nanodot; the inset shows the SAED patterns of nanodot.

Based on the above results, by controlling the crystal structure of FePt with the application of multilayer structure, we succeeded in controlling the phase transformation of FePt and in achieving the fabrication of ultra-fine FePt nanodot arrays with $L1_0$ ordered structure. Considering the improvement of the magnetic hardening in the continuous FePt films with multilayer structure, nanodot arrays with $L1_0$ structure are expected to exhibit higher coercivity, which will be analyzed in detail in future studies.

5.4 Addition of Cu into FePt Alloy towards Facilitation of $L1_0$ Ordering

Characteristics of FePtCu electrodeposition was investigated by linear sweep voltammetry at the scan rate of 20 mV s^{-1}. Fig. 5.4.1 shows the voltammograms of electrolytes containing Cu, FeCu, and FePtCu precursors; the concentration of Cu precursor was 5 mM in each electrolyte and the concentration of other metal precursors were listed in table 5.2.4. Onset of Cu reduction in the Cu electrolyte occurs at about -0.55 V (vs. Ag/AgCl), which corresponded well with the Cu reduction in glycine baths, indicating that the Cu precursor exists as glycine complex in this electrolyte [12]. Current onset at around -0.2 V (vs. Ag/AgCl) could be attributed to the proton reduction and hydrogen evolution reaction was clearly observed at more negative potential than -1.0 V (vs. Ag/AgCl). FeCu electrolyte showed increase in current density from -0.2 V (vs. Ag/AgCl) owing to the reduction of Fe(III) to Fe(II), followed by the reduction of Cu at -0.55 V (vs. Ag/AgCl) and reduction of Fe at around -0.85 V (vs. Ag/AgCl). In the FePtCu electrolyte, the reduction of Pt, which should be appeared at around -0.5 V (vs. Ag/AgCl), was hardly observed due to the overlap with the reduction of Cu. The reduction of Fe was observed at the same potential [-0.85 V (vs. Ag/AgCl)] with FeCu electrolyte; the onset of hydrogen evolution reaction shifted to more positive potential owing to the high catalytic activity of Pt.

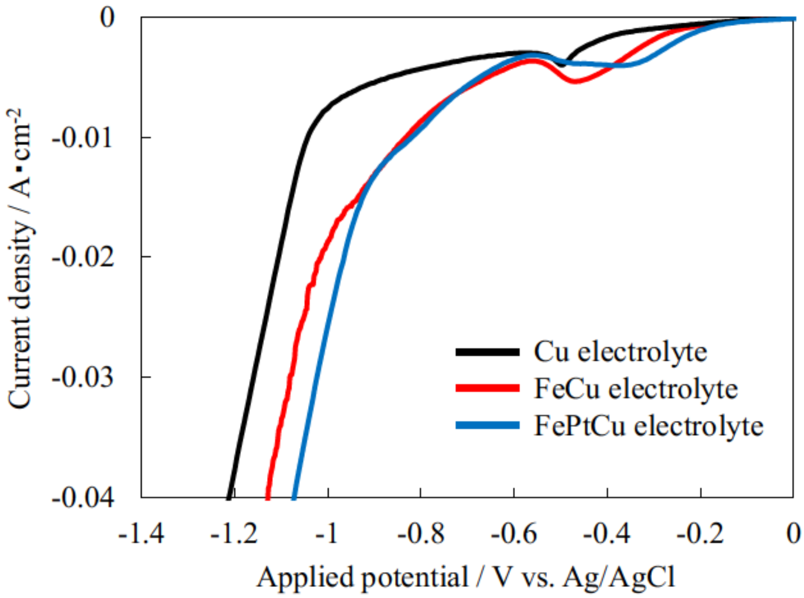

Fig. 5.4.1 Linear sweep voltammograms of electrolytes with different metal precursors. The concentrations of Cu, Fe, and Pt were 5.0 mM, 50 mM, and 15 mM, respectively.

In the previous studies, Cu additions up to ~25 at.% were considered effective in enhancement of phase transformation [4, 5]. Thus, based on the characteristics of FePtCu electrodeposition in Fig. 5.4.1, composition of 20 nm-thick FePtCu ternary alloy was optimized by adjusting the applied potential and concentration of $CuSO_4$. Because the reduction of Fe starts from -0.85 V (vs. Ag/AgCl) the applied potential was set as -1.0 V (vs. Ag/AgCl). The alloy composition pf the films deposited with various $CuSO_4$ concentrations were plotted in Fig. 5.4.2; the concentrations of $CuSO_4$ were 5.0, 0.50, 0.050, 0.040, 0.030, 0.025 mM, which were described as natural logarithm in Fig. 5.4.2. The atomic content of Cu increased with the increase in concentrations of $CuSO_4$ and films with 20~25 at.% Cu were obtained with the concentration from 0.025 to 0.05 mM. Because Pt is more noble metal than Fe, Pt preferentially deposited at this potential, resulting in the slight increase in Pt atomic content. At lower $CuSO_4$ concentrations (< 0.05 mM) the atomic contents of Fe and Pt rarely changed, thus composition was further optimized by adjusting applied potentials.

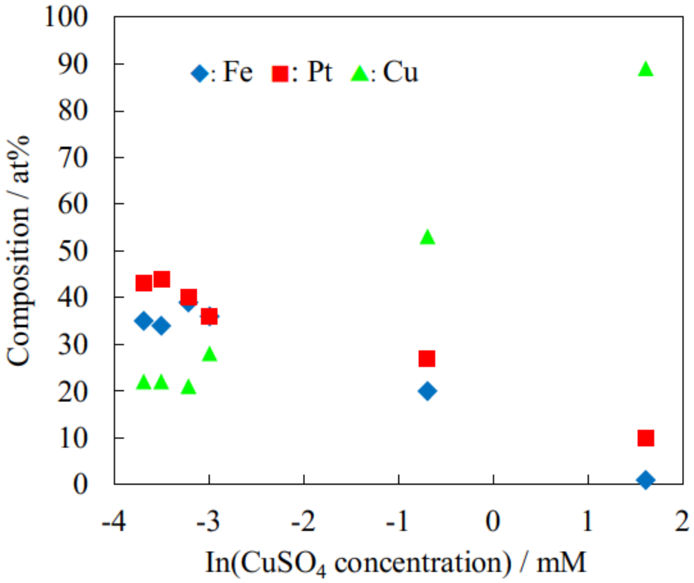

Fig. 5.4.2 Composition variation of 20 nm-thick FePtCu ternary alloy films with $CuSO_4$ concentration at applied potential of -1.0 V (vs. Ag/AgCl).

Figure 5.4.3 shows the alloy composition of 20 nm-thick FePtCu films deposited with -0.95, -1.0, -1.05 V (vs. Ag/AgCl) in different $CuSO_4$ concentrations. The composition of each metal showed a linear relation with applied potential that corresponded to the reduction potential of each metal; the noble metals of Pt and Cu increased and less noble metal, Fe, decreased with less negative potential. Table 5.4.1 summarizes the composition of FePtCu ternary films deposited with different applied potentials and $CuSO_4$ concentrations. Based on these compositional analyses, the composition of FePtCu was tuned with applied potential and $CuSO_4$ concentrations to facilitate the $L1_0$ ordering.

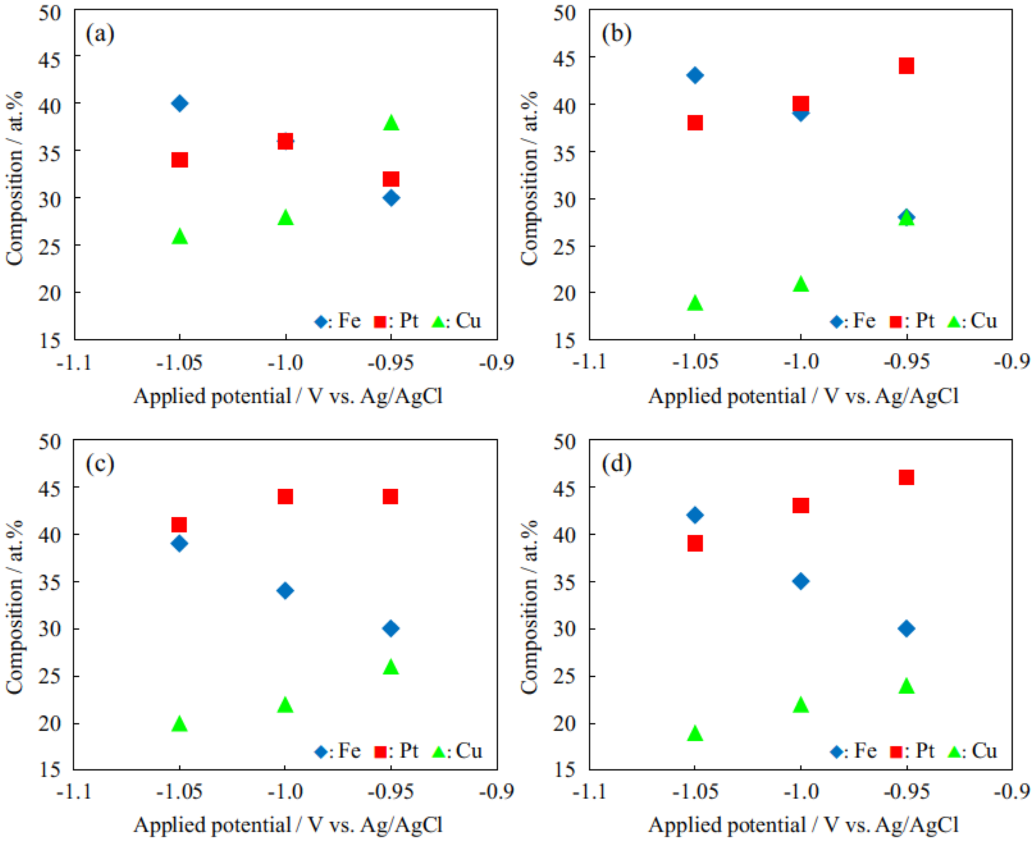

Fig. 5.4.3 Alloy composition of 20 nm-thick FePtCu continuous films deposited with $CuSO_4$ concentrations of (a) 0.050 mM, (b) 0.040 mM, (c) 0.030 mM, and (d) 0.025 mM at different applied potentials.

Table 5.4.1 The alloy composition of FePtCu continuous films

$CuSO_4$ / mM	Potential / V	Composition / at.% Fe	Pt	Cu
5.0	-1.0	1	10	89
0.50	-1.0	20	27	53
	-1.05	25	25	50
0.050	-0.95	30	32	38
	-1.0	36	36	28
	-1.05	40	34	26
0.040	-0.95	28	44	28
	-1.0	39	40	21
	-1.05	43	38	19
0.030	-0.95	30	44	26
	-1.0	34	44	22
	-1.05	39	41	20
0.025	-0.95	30	46	24
	-1.0	35	43	22
	-1.05	42	39	19

In order to investigate the phase transformation of electrodeposited FePtCu continuous films, crystal structure was analyzed after annealing at 450 ^{o}C for 60 min. Figure 5.4.4 shows the XRD patterns of 20 nm-thick FePtCu continuous films deposited with $CuSO_4$ concentrations of 0.50, 0.050, 0.040, 0.030, and 0.025 mM deposited with different applied potentials. With 0.50 mM [Fig. 5.4.4 (a)], deposited film showed peaks at 24.8 ^{o}, 43.0 ^{o}, and 44.0 ^{o}, which corresponded with the (001), (111), and (200) peaks. These measured peaks shifted more than 1.0 ^{o} compared to $L1_0$-ordered FePt; (001) and (111) shifted to higher angle, whereas (200) shifted to lower angle. The shifts in these peaks are attributed to the replacement of Fe with Cu atoms in the ordered structure, which shrinks and broadens in c- and a-axis lattice, respectively. Especially the high atomic content of Cu 50 at.% could lead to the large shift in these films compared to equiatomic FePt. With the concentration less than 0.050 mM, XRD patterns showed peaks of (001), (111), and (200) plane, and peak of (110) plane was also observed in several patterns. In these patterns, peak of elemental Cu was not observed and (001) peak and (200) shifted to higher and lower 2θ values, respectively, compared to the $L1_0$-ordered FePt, providing evidence that Cu was alloyed with FePt to form FePtCu ternary alloy. In addition, the peaks of (001) and (200) shifted to higher and lower 2θ values, respectively, with the increase in Cu composition of the films. In order to further investigate the degree of phase transformation of the deposited films, lattice parameters of c- and a-axis were calculated from the (001) and (200) peaks in Fig. 5.4.4 and the ratio of c- and a-axis was also calculated; the calculated lattice parameters and axial ratio were plotted versus $CuSO_4$ concentrations with different applied potentials in Fig. 5.4.5 and were summarized with alloy composition in table 5.4.2.

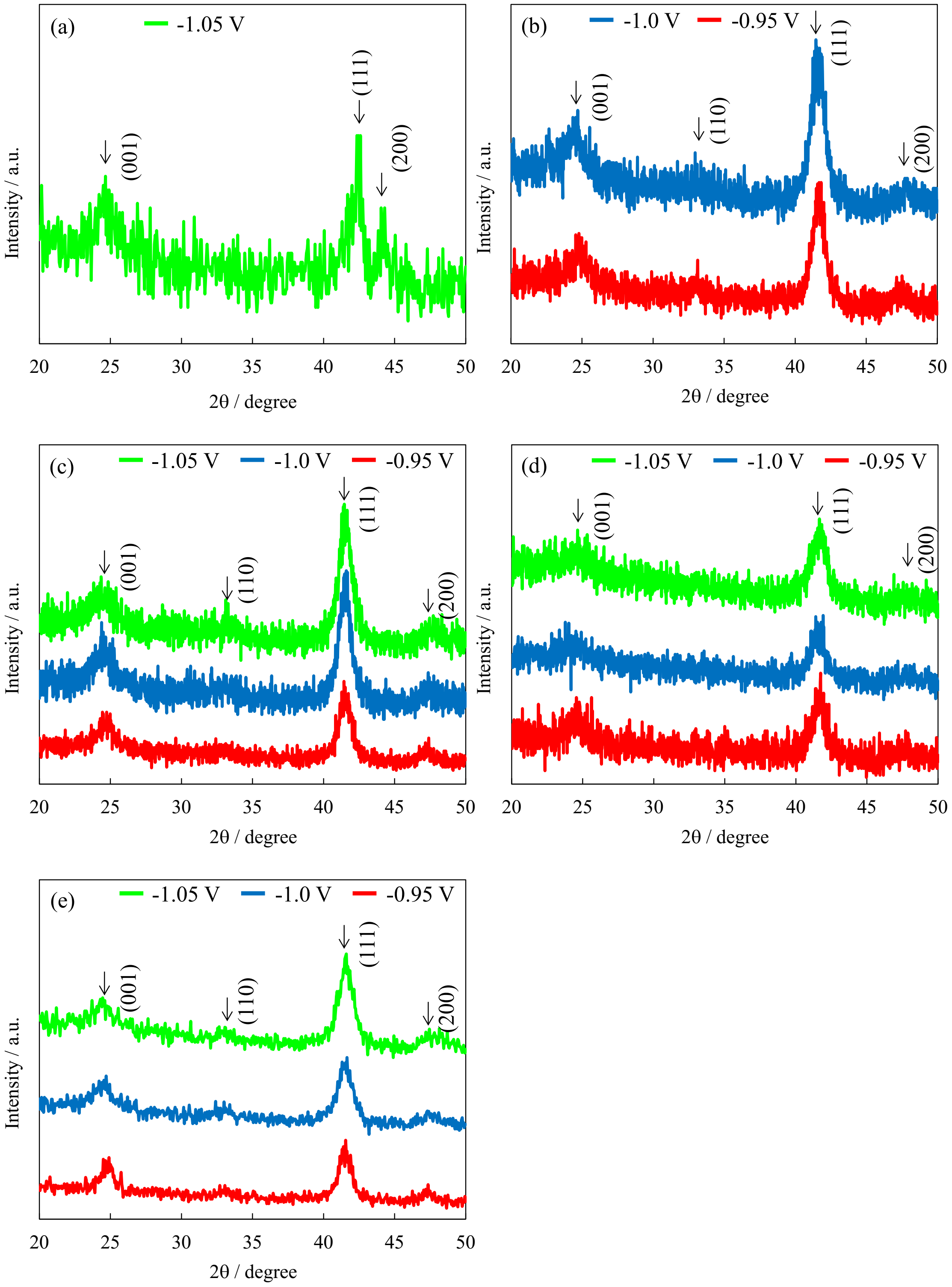

Fig. 5.4.4 XRD patterns of annealed FePtCu continuous films at 450 ^{o}C for 60 min. The films were deposited with (a) 0.50, (b) 0.050, (c) 0.040, (d) 0.030, and (e) 0.025 mM at different applied potentials.

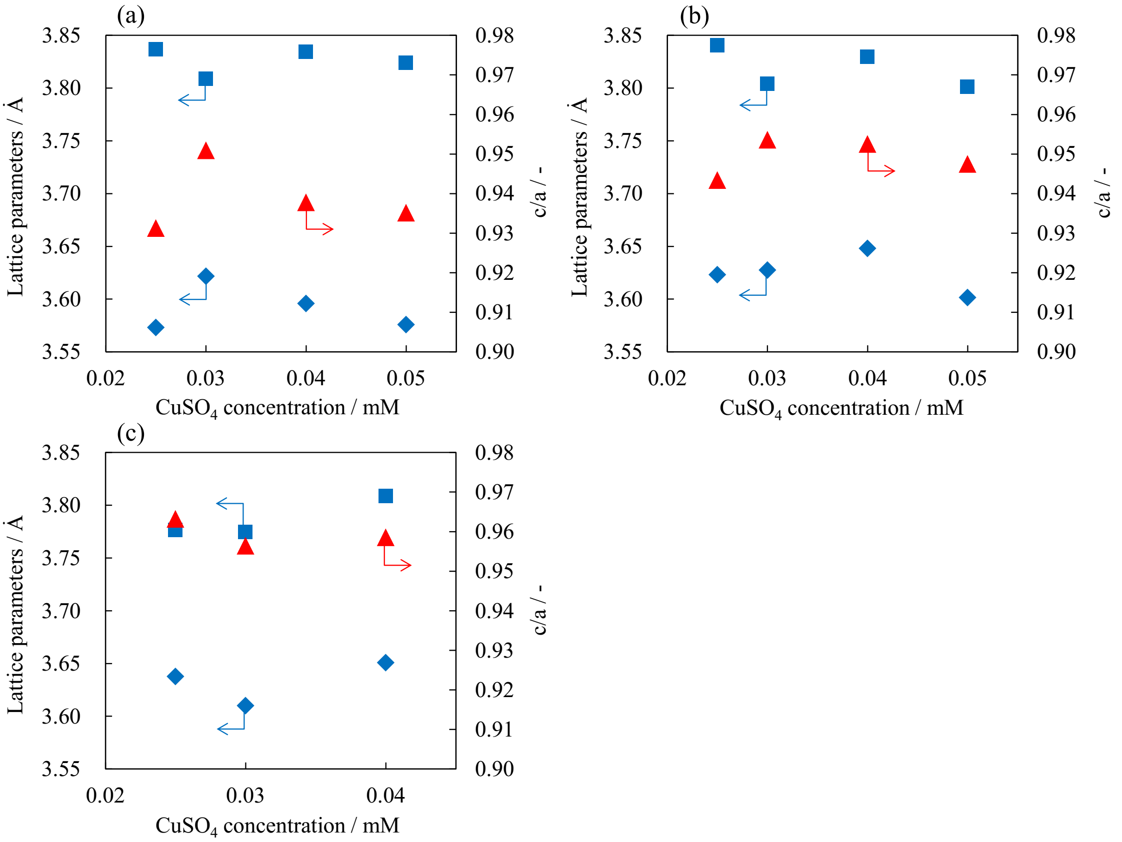

Fig. 5.4.5 Lattice parameters and axial ratio of FePtCu continuous films deposited at (a) -0.95, (b) -1.0, and (c) -1.05 V (vs. Ag/AgCl) with different CuSO$_4$ concentrations. The blue square, diamond, and red triangle corresponds to a-, c-lattice parameters and c/a axial ratio.

Table 5.4.2 The lattice parameters of FePtCu continuous films

Potential / V	CuSO$_4$ / mM	Composition / at.%			Lattice parameters		c/a
		Fe	Pt	Cu	a-axic	c-axis	
-0.95	0.050	30	32	38	3.824	3.576	0.935
	0.040	28	44	28	3.834	3.596	0.938
	0.030	30	44	26	3.809	3.622	0.951
	0.025	30	46	24	3.837	3.573	0.931
-1.0	0.050	36	36	28	3.801	3.602	0.947
	0.040	39	40	21	3.830	3.648	0.953
	0.030	34	44	22	3.804	3.628	0.954
	0.025	35	43	22	3.840	3.623	0.943
-1.05	0.50	25	25	50	4.086	3.609	0.883
	0.050	40	34	26	-	-	-
	0.040	43	38	19	3.809	3.651	0.959
	0.030	39	41	20	3.774	3.610	0.956
	0.025	42	39	19	3.777	3.638	0.963

Bulk $L1_0$ FePt value of the axial ratio is 0.964, estimated by the values of a- and c- axis of 3.852 and 3.713 Å [4], respectively. All the FePtCu films showed decrease in c-lattice parameter compared to FePt binary alloy, which suggested that the phase transformation of FePt was facilitated at lower annealing temperature of 450 °C by the addition of Cu. In addition, increasing in Cu composition led to the increase in a-lattice and decrease in c-lattice, resulting in the reduction in c/a axial ratio; lower c/a axial ratio was obtained at less negative potential compared to more negative potential owing to the high composition of Cu and Pt in the films. Figure 5.4.6 shows the FePtCu ternary phase diagram [13, 14]. From this phase diagram, because FePtCu films deposited at more negative potentials exhibited Cu composition close to 20 at.% single phase of $L1_0$-ordered structure was expected, whereas FePtCu films deposited at less negative potential could contain ordered fcc structure of both Cu- and Pt-rich phase due to its high composition of Cu and Pt.

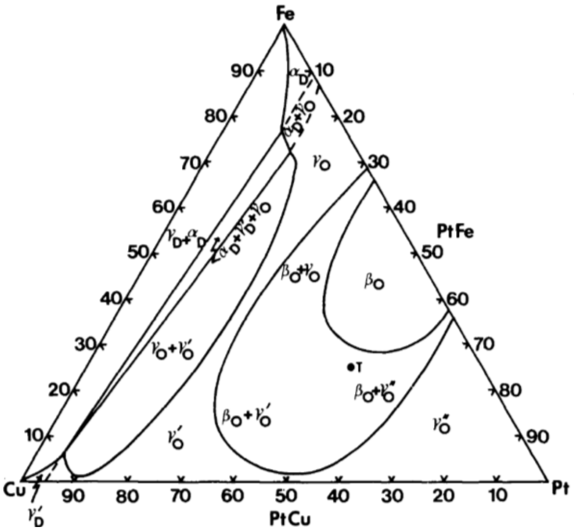

β_O: $L1_0$
γ_D: Disordered fcc (Fe-rich)
γ'_D: Disordered fcc (Cu-rich)
γ''_D: Disordered fcc (Pt-rich)
γ_O: Ordered fcc (Fe-rich)
γ'_O: Ordered fcc (Cu-rich)
γ''_O: Ordered fcc (Pt-rich)
α_D: Disordered fcc (Fe-rich)

Fig. 5.4.6 Phase diagram of FePtCu ternary alloy films [13]

In order to investigate the magnetic hardening of deposited FePtCu continuous films, coercivity was measured in each film by utilizing polar magneto-optical Kerr effect equipment. The coercivity of FePtCu deposited with different applied potentials was plotted versus $CuSO_4$ concentrations in Fig. 5.4.7 (a). As a result, an increase in coercitiy was confirmed with FePtCu ternary alloy films compared to the FePt binary films; at 450 °C, magnetic hardening was not observed for the binary alloy films, whereas FePtCu ternary alloy film showed significant magnetic hardening with the coercivity up to 6.0 kOe. The higher values of coercivity were obtained with FePtCu films deposited at less negative potentials even though these films deviate from the single phase of $L1_0$-ordered structure in the phase diagram (Fig. 5.4.6) due to its high atomic content of Cu. By contrast, although the FePtCu films deposited with negative potential are included in the composition range of single phase of $L1_0$-ordered structure, lower values of coercivity were obtained. One of the reasons for the reduction in coercivity with more negative potential is due to the higher values of c/a axial ratio. Figure 5.4.7 (b) shows the relation between coercivity and c/a axial ratio of FePtCu films deposited with different applied potentials; the measured values of coercivity were summarized in table 5.4.3 with composition and c/a axial ratio. As seen in Fig. 5.4.7 (b), the increase in perpendicular coercivity was consistent with the decreasing in the values of c/a axial ratio, indicating that FePtCu films deposited with less negative potential exhibit better perpendicular orientation even these films contain Cu-rich phase. Another reason for the lower values of coercivity at negative potentials could be due to the hydrogen evolution reaction during the electrodeposition of FePtCu. As seen in Fig. 5.4.1, a rapid current increase due to the hydrogen evolution reaction was observed below -1.0 V (vs. Ag/AgCl). This reaction can shift the local pH to higher value at the interface to cause the formation of Fe hydroxides or oxides, which incorporate as impurities in the deposited films. Thus, increase in the perpendicular coercivity with less negative potential was attributed to the reduction in the c/a axial ratio and reduced amount of hydrogen evolution reaction.

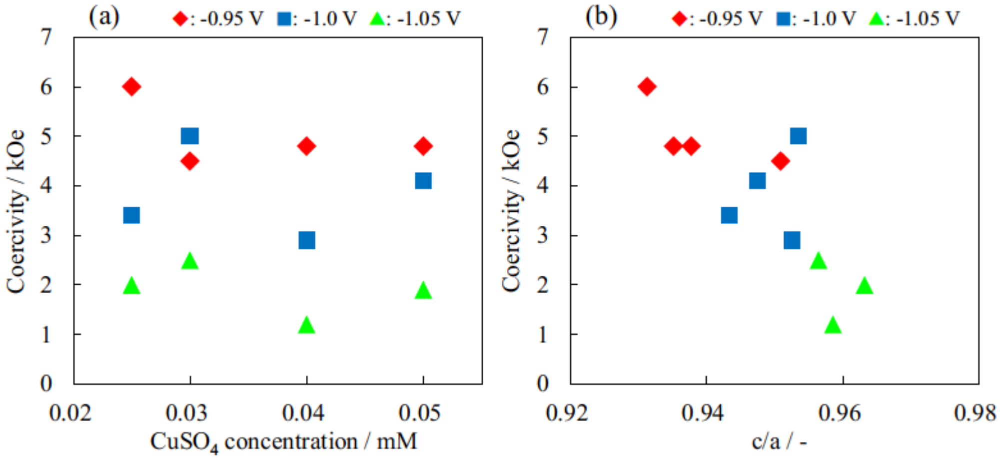

Fig. 5.4.7 Perpendicular coercivity of FePtCu films deposited with different applied potentials and $CuSO_4$ concentrations. The values of perpendicular coercivity were plotted versus (a) $CuSO_4$ concentrations and (b) c/a axial ratio.

Table 5.4.3 The perpendicular coercivity of FePtCu continuous films

Potential / V	$CuSO_4$ / mM	Composition / at.% Fe	Pt	Cu	c/a	Coercivity / kOe
-0.95	0.050	30	32	38	0.935	4.8
	0.040	28	44	28	0.938	4.8
	0.030	30	44	26	0.951	4.5
	0.025	30	46	24	0.931	6.0
-1.0	0.050	36	36	28	0.947	4.1
	0.040	39	40	21	0.953	2.9
	0.030	34	44	22	0.954	5.0
	0.025	35	43	22	0.943	3.4
-1.05	0.50	25	25	50	0.883	3.7
	0.050	40	34	26	-	1.9
	0.040	43	38	19	0.959	1.2
	0.030	39	41	20	0.956	2.5
	0.025	42	39	19	0.963	2.0

In order to fabricate Tbit/in^2 nanodot arrays with $L1_0$ structure, FePtCu ternary alloy was employed in fabrication of nanodot arrays. FePtCu nanodot arrays were fabricated with $CuSO_4$ concentration of 0.025 mM at -0.95 V (vs. Ag/AgCl) for 24 s, which was based on the strong improvement of magnetic properties and ordering behavior observed for continuous films. Figure 5.4.8 shows SEM images of as-deposited FePtCu nanodot arrays with 35 nm in pitch and 20 nm in diameter. From the top images, FePtCu was uniformly nucleated inside the nanopore over the patterned area to form FePtCu nanodot arrays.

Figure 5.4.9 and 5.4.10 shows cross sentional TEM images of FePtCu nanodot arrays with 35 nm in pitch before and after annealing at 650 ^{o}C for 0 min with 1950 oC/min. As-deposited nanodot arrays showed similar characteristic of crystal structure as observed in Fig. 5.3.9 with multilayer structure. The SAED pattern showed diffraction ring, which corresponds to polycrystalline structure. After the annealing, nanodot showed clear stacking of crystal facets orienting in a perpendicular direction without grain boundaries. The SAED pattern showed clear diffraction spots indicating that nanodot arrays recrystallize from polycrystalline structure to single crystal structure. In addition, measured lattice distance was 0.210 nm, which is slightly shorter than that of (111) plane of ordered binary alloy (0.219 nm). The reduction of the lattice distance indicated the substitution of Cu atom for Fe atom sites in the $L1_0$ structure to shrink the lattice structure in the c-axis direction as confirmed with the FePtCu continuous films, which suggests the formation of FePtCu nanodot arrays with single crystal of $L1_0$ structure.

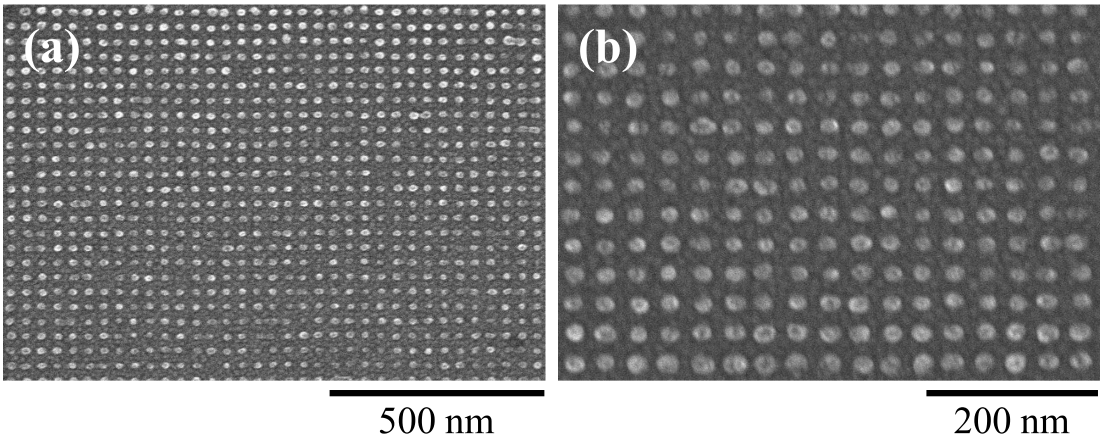

Fig. 5.4.8 (a) Low and (b) high magnification SEM images of FePtCu nanodot arrays deposited at -0.95 V (vs. Ag/AgCl) for 24 s with $CuSO_4$ concentrations of 0.025 mM.

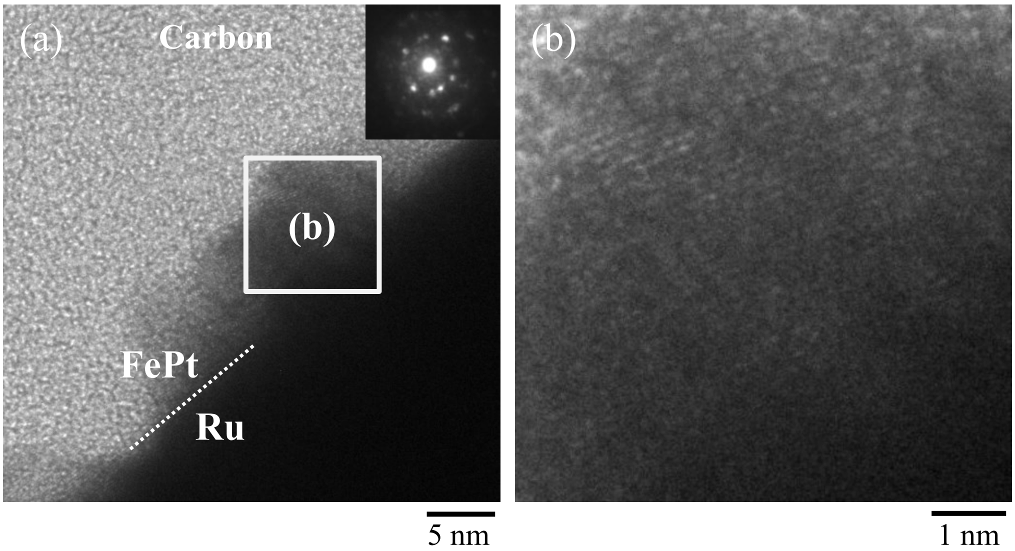

Fig. 5.4.9 Cross-sectional TEM images of as-deposited FePtCu nanodot arrays with 35 nm in pitch. (a) Low and (b) high magnification image. The insets show the SAED patternd of nanodot.

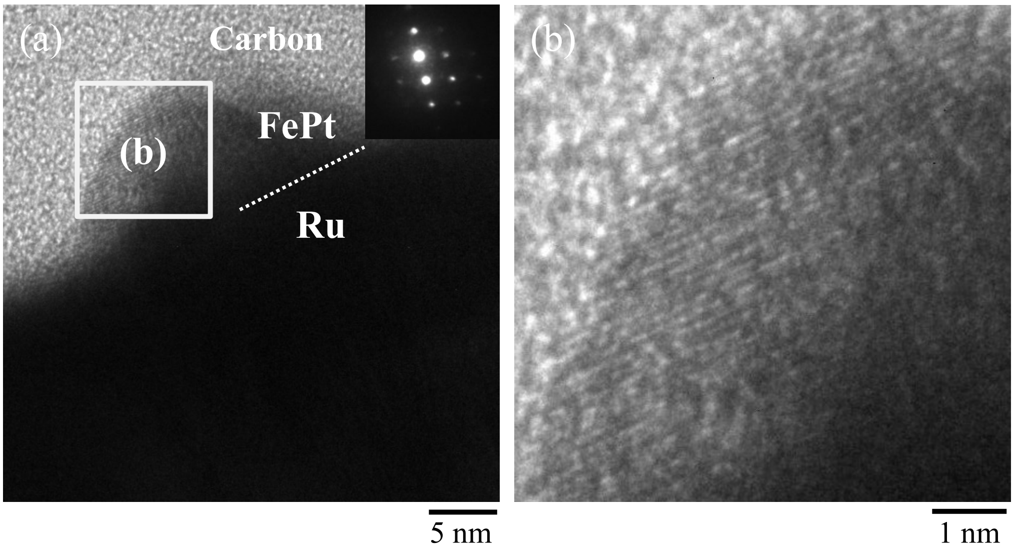

Fig. 5.4.10 Corss-sectional TEM images of annealed FePtCu nanodot arrays with 35 nm in pitch. The nanodots were annealed at 650 °C for 0 min with ramp rate of 1950 °C/min. (a) Low and (b) high magnification image. The insets show the SAED patternd of nanodot.

Based on the characterization of the continuous films and nanodot arrays, the facilitation of $L1_0$ ordering was successfully demonstrated by the fabrication of FePtCu ternary alloy. The annealed nanodot arrays showed single crystal characteristics of $L1_0$ structure with shrunken lattice structure in c-axis direction due to the alloying of Cu with FePt, which should exhibit high and uniform coercivity required for the BPM application.

Conclusion

20 nm-thick FePt multilayers consisting of Fe- and Pt-rich layer with various layer thickness were fabricated in order to achieve precise fabrication of FePt nanodot arrays with high deposition uniformity and high coercivity. It was found that the phase transformation was facilitated in the multilayer structures after annealing due to the reduction in the diffusion length of Fe and Pt atoms. The eight-layer FePt film showed a significant increase in coercivity up to 6.6 and 7.5 kOe at 450 and 650 ^{o}C, whereas single layer FePt film showed 1.0 and 4.8 kOe, respectively, suggesting that the enhancement of phase transformation did induce significant magnetic hardening with multilayer structures. In addition, the eight-layer FePt nanodot arrays showed a single crystal of $L1_0$ structure having stacking of $L1_0$ (111) lattice in a perpendicular direction from the Ru interface after annealing at 650 ^{o}C.

FePtCu ternary alloy films (20 nm thick) were fabricated by adjusting concentration of $CuSO_4$ and applied potential. Upon annealing at 450 ^{o}C, FePtCu films showed peaks of $L1_0$ order structure without elemental Cu peaks, providing evidence that the Cu was alloyed with FePt. The magnetic hardening was observed with FePtCu ternary alloy films to increase its coercivity up to 6.0 kOe. The coercivity values increased with FePtCu films deposited with less negative potentials even though these films have not only $L1_0$ phase but also Cu-rich phase. It was suggested that the increase in coercivity was attributed to the decrease in c/a axial ratio in the films deposited with less negative potential due to the higher amount of Cu content in the films, resulting in the enhancement of $L1_0$-ordering to shrink the lattice structure in c-axis direction. In addition, fabrication of FePtCu nanodot arrays with single crystal of $L1_0$ structure was successfully demonstrated due to the facilitation of $L1_0$ ordering by addition of Cu.

The collective results have successfully demonstrated enhancement of $L1_0$-ordering of FePt under lower annealing temperature or heating time requirements. Especially, electrochemical fabrication of ultra-fine FePt nanodot arrays with single crystal characteristic of $L1_0$ structure by applying multilayer structures or addition of Cu to facilitate the phase transformation was successfully demonstrated.

References

[1] Y. Endo, N. Kikuchi, O. Kitakami, and Y. Shimada, *J. Appl. Phys.*, 89 (2001) 7065.

[2] C. P. Luo , D. J. Sellmye, *IEEE Trans. Magn.*, 31 (1995) 2764.

[3] Y. Endo, K. Oikawa, T. Miyazaki, O. Kitakami, and Y. Shimada, *J. Appl. Phys.*, 94 (2003) 7222.

[4] C. L. Platt, K. W. Wierman, E. B. Svedberg, R. van de Veerdonk, J. K. Howard, A. G. Roy, and D. E. Laughlin, *J. Appl. Phys.*, 92 (2002) 6104.

[5] T. Maeda, T. Kai, A. Kikitsu, T. Nagase, and J. Akiyama, *Appl. Phys. Lett.*, 80 (2002) 2147.

[6] K. Leistner, S. Fahler, H. Schlorb, and L. Schultz, *Electrochem. Commun.*, 8 (2006) 916.

[7] D. Liang and G. Zangari, *Electrochim. Acta*, 56 (2011) 10567.

[8] S. Thongmee, B.H. Liu, J. Ding, and J.B. Yi, *Thin Solid Films*, 518 (2010) 7053.

[9] E.B. Svenberg, J.J. Mallet, S. Sayan, A.J. Shapio, W.F. Egelhoff, and T. Moffat, *Appl. Phys. Lett.*, 85 (2004) 1353.

[10] JCPDS-International Centre of Diffraction Data (2016).

[11] G. R. Trichy, J. Narayan, and H. Zhou, *Appl. Phys. Lett.*, 89 (2006) 132502-1.

[12] T.G. de Lima, B.C.C.A. Rocha, A.V.C. Braga, D.C.B. do Lago, A.S. Luna, and L.F. Senna, *Surf. Coat.*, 276 (2015) 606.

[13] M. Shahmiri, S. Muphy, and D.J. Vaughan, *Mineral. Mag.*, 49 (1985) 547.

[14] D.C. Berry and K. Barmak, *J. Appl. Phys.*, 102 (2007) 024

Chapter 6

General Conclusion

The fabrication of ferromagnetic nanodot arrays with high areal density and high coercivity is of extreme importance for the application in bit patterned media (BPM). The objective of this study is to propose electrochemical fabrication process of ultra-fine ferromagnetic nanodot arrays with high crystallinity and high crystal orientation, which is the origin of high coercivity, for the BPM application.

In order to achieve this objective, growth behavior of nanodot arrays was investigated in detail based on the analyses of crystal growth and initial nucleation processes of ferromagnetic materials. As ferromagnetic materials, hcp-CoPt and $L1_0$-FePt were studied as promising candidates for BPM application owing to their high perpendicular magnetic anisotropy. Because annealing process is not required for the fabrication of hcp-CoPt, its growth behavior inside the nanopores was focused to be analyzed as a fundamental study. On the other hand, annealing process is necessary to fabricate FePt with $L1_0$-ordered structure, whose crystal structure strongly affects the coercivity, thus effect of annealing process on the crystal structure of FePt was analyzed. In addition, acceleration of $L1_0$ ordering was investigated to achieve fabrication of FePt nanodot arrays with Tbit/in^2 areal density.

In this chapter, the collective results of this study are summarized, and the possibility of electrochemical fabrication process for the BPM application is discussed.

From the discussion in chapter 2, the fabrication of nanopore patterned substrate with Tbit/in^2 density and fabrication of CoPt nanodot arrays with high crystal orientation are proposed as follows.

In order to fabricate nanopore patterned substrate with Tbit/in^2 areal density, electron beam lithography (EBL) was utilized and its fabrication conditions, such as prebake temperature and dose values, were optimized. By increasing the prebake temperature, photosensitivity was improved to form uniform nanopore patterned substrate with above 35 nm in pitch with positive-type resist (ZEP520A-7). Further uniformity in nanopore patterned substrate was achieved with the utilization of negative-type resist (TEBN-1), which has higher resolution, by optimizing the dose values, and fabrication of nanopore patterned substrate with 15 nm diameter and 25 nm pitch, corresponding to 2.0 Tbit/in^2 was successfully demonstrated.

To achieve high coercivity of the nanodot arrays, crystal structure was controlled by controlling the diffusion state of metal ions from the initial deposition stages. Electrolyte agitation mitigated the diffusion limited growth of CoPt to homogenize the alloy composition from the initial deposition stage, whereas large composition gradient with growing thickness was observed without agitation. This uniform composition of CoPt resulted in increase in crystallinity of hcp structure in (002) direction, which led to increase in the coercivity of CoPt continuous films. By utilizing the above mentioned nanopore patterned substrate, fabrication of CoPt nanodot arrays with 25 nm in pitch, corresponding to 1.0 Tbit/in^2 was successfully fabricated under electrolyte condition. Furthermore, CoPt nanodot arrays with 35 nm in pitch showed clear stacking of hcp (002) lattice in perpendicular direction, which induces high perpendicular magnetic anisotropy to increase coercivity and squareness from 2.0 kOe and 0.64 to 4.0 kOe and 0.87 by applying electrolyte agitation.

From the discussion in chapter 3, fabrication of CoPt nanodot arrays consist of single grains (single crystal structure) was demonstrated based on the detail analyses of nucleation and growth process of CoPt inside the nanopores as follows.

Single grain structure/single crystal structure is highly desirable for the BPM application owing to its high coercivity and high crystallinity. To achieve deposition of CoPt single grains inside nanopore patterned substrate, nucleation and growth behavior of CoPt was focused to be analyzed. It was found that at negative potential of --0.9 V (vs. Ag/AgCl), which was used conditions in chapter 2, CoPt nucleated as 2.0-3.0 nm grains at the initial stage, they grew as a cluster with several grain boundaries in side nanopore with 10 nm diameter. To realize deposition of single grains, CoPt was deposited with less negative potential [> -0.7 V (vs. Ag/AgCl)] to induce growth of nucleus to form larger size grain. As a result, deposition of single nucleus with 5.0 nm was successfully demonstrated with less negative potentials. The detail analysis of the distribution of CoPt nuclei demonsteated the existence of nucleation exclusion zone, which suggested that the exlusion zone may conver the Ru surface inside 10 nm nanopore to inhibit the formation of new neculeus, resulting in the formation of a single nucleus. From the detail characterization of lattice structure of nanodot arrays, it was found that at less negative potential, a single nucleus of CoPt was formed inside the nanopore that subsequently grew from the interface of Ru underlayer in perpendicular direction to form a single crystal structure.

From the discussion in chapter 4, fabrication process of FePt nanodot arrays with Tbit/in^2 areal density was developed by optimizing the deposition conditions of FePt and post annealing process as follows.

In order to further achieve high coercivity of Tbit/in^2 nanodot arrays, fabrication process of $L1_0$-FePt nanodot arrays were proposed as a promising candidate for BPM application. The composition of FePt was optimized to deposit equiatomic FePt, which is required for the phase transformation to $L1_0$-ordered structure. The equiatomic FePt continuous film showed $L1_0$-ordering upon annealing at 650 °C for 60 min, which induced magnetic hardening of the films to increase its coercivity up to 9.0 kOe with 10 nm-thick film (the maximum value 13.3 kOe was obtained for 200 nm-thick film), which is two times higher than the value of CoPt. By utilizing the nanopore patterned substrate as described in chapter 2, fabrication of FePt nanodot arrays with 1.0 Tbit/in^2 areal density (25 nm pitch) was successfully demonstrated. However, when the same annealing condition as continuous films was applied to the fabrication of nanodot arrays, major deterioration of nanodot arrays was observed due to the diffusion of Fe and Pt atoms or the aggregation of nanodots. In order to achieve uniform nanodot arrays, higher ramp rate and lower holding time were applied. The fabrication of FePt nanodot arrays with 35 nm in pitch was successfully demonstrated upon annealing at 650 °C with ramp rate of 1950 °C/min and holding time of 0 min. However, it was suggested that the enhancement of phase transformation was required due to the insufficient $L1_0$-ordering of nanodot arrays.

From the discussion in chapter 5, enhancement of $L1_0$-ordering of FePt nanodot arrays was proposed by the application of multilayer Fe/Pt structure and by the addition of Cu into FePt alloy.

Based on the results of chapter 4, Fe/Pt multilayer structure and FePtCu ternary alloy were fabricated to promote the phase transformation of FePt. Fe/Pt multilayer structure consists of Fe- and Pt-rich layers, which were deposited by changing the applied potential and deposition duration for each layer. Effects of thickness of each layer on the $L1_0$-ordering and magnetic properties of 20 nm-thick Fe/Pt multilayer films were studied. The Fe/Pt films consist of thicker (5.0 nm) and thinner (1.0 nm) layer decreased the ordering parameters, which led to decrease in coercivity of the films. The thicker layer could result in a larger diffusion length of Fe and Pt atoms, whereas thin layer could be partially discontinuous and the separation of each layer was nonuniform, resulting in the insufficient interdiffusion of Fe and Pt during the annealing process in both multilayer structures. On the other hand, Fe/Pt films with layer thickness of 2.5 nm showed ordering parameter of 0.82 after annealing at 450 °C, which was further enhanced to 0.94 after annealing at 650 °C. The coercivity of this film after annealing at 450 and 650 °C was 6.6 and 7.5 kOe, whereas single layer FePt film showed 1.0 and 4.8 kOe, respectively, suggesting that the phase transformation and magnetic hardening was strongly facilitated in the multilayer structures. By applying multilayer structure in nanodot arrays, phase transformation of nanodot arrays was successfully achieved to form FePt nanodots single crystals with the $L1_0$

structure having uniform lattice fringes on the $L1_0$ (111) plane in the perpendicular direction from the Ru substrate.

FePtCu ternary alloy films were deposited by adding $CuSO_4$ into the FePt electrolyte and their alloy composition was optimized by changing the concentration of $CuSO_4$ and applied potential. Upon annealing at 450 ^oC, Cu was alloyed with FePt to form FePtCu ternary alloy with L10 structure, and magnetic hardening with the coercivity up to 6.0 kOe was successfully demonstrated with ternary alloy, whereas binary alloy did not show magnetic hardening. The higher values of coercivity were obtained with FePtCu films deposited with -0.95 V (vs. Ag/AgCl) compared to films deposited with -1.05 V (vs. Ag/AgCl) even though these films have Cu-rich phase. Less negative potential was effective to decrease the c/a lattice ratio due to its higher amount of Cu composition, which enhances the $L1_0$-ordering by shrinking the lattice in c-axis. Also, hydrogen evolution reaction is mitigated at less negative potential to prevent the formation of Fe hydroxide or oxide, which could incorporate as impurities in the deposited films. In addition, fabrication of FePtCu nanodot arrays with 35 nm in pitch was also successfully demonstrated.

In this thesis, the objective to fabricate Tbit/in^2 nanodot arrays with high crystallinity to induce high coercivity was successfully demonstrated in both CoPt and FePt systems by controlling the crystal structure from the initial deposition stages based on the detailed analyses of crystal structure and nucleation process of nanodots. Especially, the objective to achieve fabrication of nanodot arrays consisting of single grains, which is highly desirable for the application in BPM, was successful. To the best of my knowledge, this is the first work that demonstrates the electrochemical fabrication of nanodot arrays with Tbit/in^2 areal density that exhibit relatively high coercivity (>4.0 kOe). The collective results suggested the feasibility of electrochemical fabrication process as a promising candidate for the application in BPM. Moreover, since little is known concerning the electrochemical growth behavior inside the nanostructure, results obtained from the analyses of initial deposition stages inside the nanopore could be applicable for the electrochemical fabrication of micro/nano-structures.

List of Achievements

1 Original Publication

“Structural Control of Ultra-Fine CoPt Nanodot Arrays via Electrodeposition Process”
S. Wodarz, T. Hasegawa, S. Ishio, T. Homma
Journal of Magnetism and Magnetic Materials, in press

“Analysis and Control of the Initial Electrodeposition Stages of Co-Pt Nanodot Arrays”
S. Wodarz, J. Abe, T. Homma
Electrochimica Acta, 197, 330-335 (2016)

“Characterization of Electrodeposited Co-Pt Nanodot Array at Initial Deposition Stage”
S. Wodarz, T. Otani, H. Hagiwara, T. Homma
Electrochemical Society Transaction, 64, 99-105 (2015)

“Fabrication of FePt and CoPt Magnetic Nanodot Arrays by Electrodeposition Process”
T. Homma, S. Wodarz, D. Nishiie, T. Otani, S. Ge, G. Zangari
Electrochemical Society Transaction, 64, 1-9 (2015)

“Raman and DFT Study of the Reaction of Hydrazine and Hypophosphite on a Cu Surface in the Electroless Deposition Process”
B. Jiang, S. Wodarz, M. Kunimoto, M. Yanagisawa, T. Homma
Electrochemistry, 81, 674-677 (2013)

2 Technical Reports

“The Study on Electrodeposited FePt Nanodot Array with Multilayer Structure for Low $L1_0$-ordering Temperature”
M. Saito, S. Wodarz, S. Hashimoto, G. Zangari, T. Homma
IEEE technical report, 116, 1-5 (2016)

“Fabrication of FePt Nanodot Arrays with High Coercivity by Pulse Electrodeposition”
D. Nishiie, S. Wodarz, C. T. Hsieh, M. Saito, J. Abe, G. Zangari, T. Homma
IEEE technical report, 115, 25-29 (2016)

“Fabrication of ultra-high density nanodot arrays with high coercivity based on analysis of initial deposition process”
H. Hagiwara, S. Wodarz, T. Otani, D. Nishiie, G. Zangari, T. Homma
IEEE technical report, 114, 7-10 (2014)

“Characterization and analysis of deposition behavior of ultra-high density ferromagnetic nanodot arrays fabricated by electrochemical processes”
S. Wodarz, Y. Maniwa, H. Hagiwara, T. Homma
IEEE technical report, 113, 7-10 (2013)

“Characterization and analysis of deposition process of ultra-high density magnetic nanodot arrays fabricated by electrochemical processes”
S. Wodarz, Y. Maniwa, H. Hagiwara, T. Homma
IEEE technical report, 113, 13-17 (2013)

3 Review Articles

“Fabrication of Nanodots via Electrodeposition Process”
S. Wodarz, T. Homma
Electrochemistry, 83, 1012-1015 (2016)

4 Oral Presentations

“Structural Control of Electrodeposited $L1_0$-FePt Nanodot Arrays towards Reduction of Ordering Temperature”
S. Wodarz, S. Hashimoto, M. Saito, G. Zangari, T. Homma
PRiME 2016 (2016), invited

“The Study on Electrodeposited FePt Nanodot Array with Multilayer Structure for Low $L1_0$-ordering Temperature”
M. Saito, S. Hashimoto, S. Wodarz, G. Zangari, T. Homma
IEICE-MR (2016)

“Fine Structural Control towards High Coercivity of Electrodeposited CoPt Nanodot Arrays”
S. Wodarz, J. Abe, T. Homma
83rd Meeting of the Electrochemical Society of Japan (2016)

“Analysis of Initial Deposition Stages of Electrodeposited CoPt Nanodot Arrays towards Fine Structural Control”
J. Abe, S. Wodarz, T. Homma
133th Meeting of the Surface Finishing Society of Japan (2016)

“Study on the Low $L1_0$ Ordering Temperature of FePt Nanodot Arrays with High Coercivity via Pulse Electrodeposition”
S. Hashimoto, S. Wodarz, D. Nishiie, M. Saito, G. Zangari, T. Homma
133th Meeting of the Surface Finishing Society of Japan (2016)

“Analysis of Initial Deposition Stage of Co-Pt Nanodot Arrays”
S. Wodarz, T. Homma
DGIST-WASEDA Workshop on Electrochemistry (2015)

“The Study on Fabrication Process of Ultra-High Density FePt Nanodot Array via Electrodeposition”
M. Saito, D. Nishiie, S. Wodarz, G. Zangari, T. Homma
Fall Meeting of the Electrochemical Society of Japan (2015)

“Fabrication of FePt Nanodot Arrays with High Coercivity by Pulse Electrodeposition”
D. Nishiie, S. Wodarz, C. T. Hsieh, M. Saito, J. Abe, G. Zangari, T. Homma
IEICE-MR (2015)

“Growth Control of Electrodeposited Co-Pt Nanodot Arrays”
S. Wodarz, J. Abe, T. Homma
13th International Fischer Symposium (2015)

“Analysis of the Initial Stage of Co-Pt Electrodeposition Process at Nanopatterned Substrate”
S. Wodarz, T. Otani, H. Hagiwara, T. Homma
10th International Symposium on Electrochemical Micro & Nanosystem Technology (2014)
“Characterization of Electrodeposited Co-Pt Nano-Dot Array at Initial Deposition Stage”
S. Wodarz, T. Otani, H. Hagiwara, T. Homma
226th Meeting of the Electrochemical Society (2014)

“Fabrication of FePt and CoPt Magnetic Nanodot Arrays by Electrodeposition Process”
T. Homma, S. Wodarz, D. Nishiie, T. Otani, S. Ge, G. Zangari
226th Meeting of the Electrochemical Society (2014)

“Fabrication of ultra-high density nanodot arrays with high coercivity based on analysis of initial deposition process”
H. Hagiwara, S. Wodarz, T. Otani, D. Nishiie, G. Zangari, T. Homma
IEICE-MR (2014)

“Fabrication of electrodeposited CoPt nanodot array via initial deposition control and analysis of magnetic property”
T. Otani, S. Wodarz, T. Homma
81th Meeting of the Electrochemical Society of Japan (2014)

“Characterization and analysis of deposition behavior of ultra-high density ferromagnetic nanodot arrays fabricated by electrochemical processes”
S. Wodarz, Y. Maniwa, H. Hagiwara, T. Homma
IEICE-MR (2013)

"Electrochemical Fabrication of Magnetic Nanostructures - analysis, control, and design of deposition processes-"
T. Homma, S. Wodarz, B. Jiang, M. Kunimoto, M. Yanagisawa
224th Meeting of the Electrochemical Society (2013)

"Characterization and analysis of deposition process of ultra-high density magnetic nanodot arrays fabricated by electrochemical processes"
S. Wodarz, Y. Maniwa, H. Hagiwara, T. Homma
IEICE-MR (2013)

"Analysis of initial electrodeposition process of CoPt into nanopatterns"
S. Wodarz, H. Hagiwara, A. Takami, T. Homma
80th Meeting of the Electrochemical Society of Japan (2013)

"Fabrication of CoPt nanodot array with high coercivity by controlling plating bath composition"
H. Hagiwara, S. Wodarz, A. Takami, T. Homma
80th Meeting of the Electrochemical Society of Japan (2013)

"Fabrication and characterization of ultra-high density magnetic nanodot arrays fabricated electrochemical processes"
A. Takami, Y. Maniwa, S. Wodarz, H. Hagiwara, T. Homma
IEICE-MR (2012)

"Surface Enhanced Raman Scattering Analysis of Electroless Deposition with Two Reducing Agents"
S. Wodarz, N. Shimano, A. Otomo, M. Kunimoto, M. Yanagisawa, T. Homma
79th Meeting of the Electrochemical Society of Japan (2012)

Acknowledgements

Firstly, I want to express my appreciation to my thesis advisor Professor Dr. Takayuki Homma. He has been supportive since I joined the laboratory as an undergraduate. He has taught me not only the scientific knowledge but also the attitude with joy and enthusiasm for the research. I would like to appreciate his thoughtful guidance and warm encouragement for several years helping me to grow as a researcher. I would also like to express my appreciation to Professor Dr. Kazuyuki Kuroda, Professor Dr. Yoshiyuki Sugahara, and Professor Dr. Toshiyuki Momma for their ideas, helpful suggestions, and encouragement.

I would like to thank to Professor Dr. Yasuhiro Fukunaka, Professor Dr. Masahiro Yanagisawa, and Dr. Mikiko Saito. Their insightful suggestions helped me to get new ideas for my thesis research.

The detail discussion of magnetic properties of CoPt nanodot arrays in this thesis would not have been possible without the polar magneto-optical Kerr effect measurement from the group of Professor Dr. Takashi Hasegawa and Professor Dr. Shunji Ishio at Akita University. I wish to my sincere appreciation to their collaboration and helpful suggestions on my research.

In the work of fabrication of FePt nanodot arrays, I would like to appreciate the group of Professor Dr. Giovanni Zangari at the University of Virginia for their significant contributions. The collaboration work with Professor Dr. Giovanni Zangari at Waseda University in 2011 has helped me developing the research of FePt nanodot arrays fabrication. I would like to appreciate his warm encouragement and insightful comments on my research through the years.

I would like to thank my collaborators and colleagues for making my time in the laboratory enjoyable. I am grateful to work with my senior and junior collaborators; Mr. Naofumi Shimano, Mr. Yohei Konishi, Mr. Atsushi Takami, Mr. Yuta Maniwa, Mr. Hiroki Hagiwara, Mr. Junya Abe, Mr. Manabu Saito, Mr. Shogo Hashimoto, Mr. Tatsuki Tokuda, and Miss. Mana Kanbe. I would like to appreciate their contribution of time and enthusiasm on the

research. I also thank to my senior and junior colleagues in doctoral course; Dr. Masahiro Kunimoto, Dr. Nobufumi Matsuo, Mr. Yasuhiro Tsuyuki, and Mr. Tomohiro Otani. Their joy and enthusiasm on research inspired me during the tough times in the doctoral course. I would like to thank them for helpful discussions and for the fun we had through the years.

Lastly, I would like to express my gratitude to my parents and to my sister for always believing in me and supporting me. Your love and joy have encouraged me thus far.

February, 2017
Siggi Wodarz